



저작자표시-비영리-변경금지 2.0 대한민국

이용자는 아래의 조건을 따르는 경우에 한하여 자유롭게

- 이 저작물을 복제, 배포, 전송, 전시, 공연 및 방송할 수 있습니다.

다음과 같은 조건을 따라야 합니다:



저작자표시. 귀하는 원저작자를 표시하여야 합니다.



비영리. 귀하는 이 저작물을 영리 목적으로 이용할 수 없습니다.



변경금지. 귀하는 이 저작물을 개작, 변형 또는 가공할 수 없습니다.

- 귀하는, 이 저작물의 재이용이나 배포의 경우, 이 저작물에 적용된 이용허락조건을 명확하게 나타내어야 합니다.
- 저작권자로부터 별도의 허가를 받으면 이러한 조건들은 적용되지 않습니다.

저작권법에 따른 이용자의 권리는 위의 내용에 의하여 영향을 받지 않습니다.

이것은 [이용허락규약\(Legal Code\)](#)을 이해하기 쉽게 요약한 것입니다.

[Disclaimer](#)

공학박사학위논문

A coarse-grained approach  
on the particle simulation of  
capillary suspensions

모세관 현탁액의 입자 시뮬레이션을 위한  
근사적 접근법

2022 년 8 월

서울대학교 대학원  
화학생물공학부  
최진환

A coarse-grained approach  
on the particle simulation of  
capillary suspensions

모세관 현탁액의 입자 시뮬레이션을 위한  
근사적 접근법

지도교수 안 경 현

이 논문을 공학박사 학위논문으로 제출함

2022 년 8 월

서울대학교 대학원

화학생물공학부

최 진 환

최진환의 공학박사 학위논문을 인준함

2022 년 8 월

위 원 장	_____	남 재 욱	(인)
부위원장	_____	안 경 현	(인)
위 원	_____	김 소 연	(인)
위 원	_____	박 준 동	(인)
위 원	_____	이 성 재	(인)

# Abstract

Jin Hwan Choi

School of Chemical and Biological Engineering

The Graduate School

Seoul National University

A capillary suspension is a ternary system consisting of one solid and two immiscible liquids. As a small amount of one of the fluids, also known as the secondary fluid, is present in between the particles to form a sample-spanning network, the suspension experiences dramatic changes in the rheological properties. Previously, the simulation studies of the capillary suspension were limited to small scaled analyses of the local cluster and morphology. In this paper, a particle simulation on the capillary suspension is proposed by introducing the coarse-grained interaction between fluid droplets and solid particles and investigate the structure and rheological properties of the capillary suspension during flow. Due to the difficulties associated with solving the actual free surface including multiple partial differential equations and an excessive amount of computing resources, coarse-graining is inevitable to investigate the structural and rheo-

logical properties of the capillary suspension through a particle simulation. The shape of the free surface between two fluid phases is simplified and assumed as a sphere, which can be partially superposed on the solid surface, while the volume occupied by the fluid droplet is preserved. The capillary force exerted by the secondary fluid droplets connecting the particles is described by considering the surface energy difference when the distance between the particle and the secondary fluid droplet changes. The secondary fluid droplet, upon contact with a particle, goes through a radius change to preserve its volume that is superposed by the particle volume, and vice versa. The surface area change causes the surface energy difference, and the inter-particle force is described to minimize the surface energy. By using the method, the formation of the capillary suspension is simulated under various conditions to achieve a sample-spanning network. The characteristic variables that determine the strength and morphology of the capillary suspension are particle volume fraction( $\phi_p$ ), secondary fluid volume fraction( $\phi_f$ ), the three-phase contact angle( $\theta$ ), and the size of the secondary fluid droplets( $\kappa$ ). The effect of the characteristic variables on the formation and structure of the capillary suspension is investigated using various tools including cluster size analysis, bond number analysis, and rheological properties. In addition, various modes of mixing protocol were compared. After the optimal values for the characteristic variables to describe the capillary suspension the best are determined, the structure and flow properties of the capillary suspension are investigated at the size ratio of 0.4, the three-phase contact angle of 92 degrees, and particle and secondary fluid concentration of 25 vol% and 2 vol%, respectively. To measure the rheological properties accurately, the number of the particles was fixed at 10,000 and the number of the secondary fluid droplets vary according to the secondary fluid volume fraction and the size ratio. The low shear rate viscosity was analyzed with varying the secondary fluid volume

fraction and showed that the viscosity dependency on the secondary fluid volume fraction is similar to what was measured in the experiment. Through the rate sweep analysis, the capillary suspension is found to exhibit a strong shear thinning behavior and a sudden slope change of the shear stress at low shear rate regime due to the local freezing. Under low dimensionless shear rates less than 0.5, the simulated flow properties show a sign of local freezing, and the viscosity and stress measured in bulk do not reflect the local freezing due to the Lees-Edwards boundary condition. Therefore, the local properties of the frozen zone are isolated from the bulk properties and further investigated. The local properties are measured by dividing the simulation window into pieces in the y-direction and measuring the particle velocity and stress at each segment. The local stress increases linearly with the local strain in the frozen zone, exhibiting an elastic behavior. This indicates that the material preserves its structure over the imposed strain, and the difference between imposed and apparent strain is interpreted as the effect of yield stress. At different shear rates, the local properties of the frozen zones are measured and compared to find out the stress at which the elastic behavior vanishes. Finally, the yield stress is calculated as 5.7 in dimensionless form, similar to that reported in previous studies. Under an oscillatory flow, an amplitude sweep test was performed and the results demonstrated a strain thickening at 0.1 strain. The amplitude sweep data were analyzed with Sequence of Physical Process. This study attempted to describe the capillary suspension through a simulation by suggesting a methodology involving a coarse-grained approach and successfully reproduced some key characteristics of the capillary suspension.

**Keywords:** Capillary suspension, Particle simulation, Yield stress, Local freezing

**Student Number:** 2015-30219

# Contents

<b>Abstract</b>	<b>i</b>
<b>1 Introduction</b>	<b>1</b>
1.1 Capillary suspension . . . . .	2
1.2 Solving the free interface . . . . .	9
1.3 Yield stress . . . . .	12
1.4 Oscillatory shear . . . . .	14
1.5 Thesis outline . . . . .	16
<b>2 Methodology</b>	<b>17</b>
2.1 Capillary interaction . . . . .	19
2.2 Droplet friction on the particle surface . . . . .	29
2.3 Core-repulsion and hydrodynamic friction . . . . .	31
2.4 Evolution of particle and droplet positions under shear flow . . . . .	34
2.5 Simulation condition and analysis method . . . . .	36
2.6 Experimental . . . . .	43
<b>3 Results</b>	<b>46</b>
3.1 Effect of characteristic variables . . . . .	46

3.1.1	Effect of $\theta_c$ . . . . .	47
3.1.2	Effect of $\kappa$ and $\phi_f$ . . . . .	51
3.1.3	Effect of $\phi_p$ . . . . .	59
3.1.4	Effect of polydispersity in $\kappa$ . . . . .	62
3.2	Structure evaluation . . . . .	67
3.2.1	Effect of mixing protocol . . . . .	67
3.2.2	Sample-spanning network . . . . .	71
3.3	Flow properties of model capillary suspension . . . . .	74
3.3.1	Flow curve . . . . .	74
3.3.2	Yielding . . . . .	76
3.3.3	Oscillatory shear flow behavior . . . . .	85
<b>4</b>	<b>Conculsion</b> . . . . .	<b>91</b>
4.1	Concluding remarks . . . . .	91
4.2	Conclusion . . . . .	96
<b>A</b>	<b>Formulation</b> . . . . .	<b>102</b>
	<b>초록</b> . . . . .	<b>109</b>

# List of Figures

1.1	A schematic demonstrating different types of ternary systems containing one solid and two immiscible fluids. At very low or very high concentrations of wetting fluid, two different categories of capillary suspension are formed, a pendular state or a capillary state. At intermediate concentrations of wetting fluid, agglomerates, bijel, or Pickering emulsion is formed. . . . .	3
1.2	A rate sweep graph of experimentally measured viscosity of varying secondary fluid volume fractions. Black, red, pink, brown, green, and purple indicate secondary fluid volume fractions of 0, 0.25, 1, 1.5, 1.75, and 2 vol %, respectively. The system is prepared with spherical PMMA particles with 20 $\mu\text{m}$ diameter, glycerol as primary fluid, and paraffin oil as secondary fluid. The system is known to have approximately 90 degrees of three-phase contact angle. . . . .	6

2.1	A schematic of (a)before and (b)after the contact when describing the coarse-grained potential. Grey( $I$ ) and blue( $j$ ) indicate the particle and the droplet, respectively. $a$ , $a_f$ , $V_{ov}$ , $r$ , $x$ represent the particle radius, the droplet radius, the volume of the droplet overlapped by the particle, the distance between the centers of the particle and the droplet, and the distance between the particle center and the cross-section where the particle and the droplet cross. The area of the droplet (blue) is maintained to remain constant. . . . .	20
2.2	At the contact angle, $\theta_c = 90$ , the total surface area change with respect to the center-to-center distance is plotted for the cases where the droplet to particle size ratio is (a)1 and (b)0.4. Blue(1L1S), red(1L2S), and green(1L3S) circles represent the droplet interacting with 1, 2, and 3 particles, respectively. $r/a$ is the dimensionless distance, where $r$ is the distance between the centers of droplet and particle, and $a$ is the radius of the particle. . . . .	26
2.3	The depth-cut snapshots of the particles and droplets during the initial mixing with shear rate of $10^1$ at strains of (a) 0, (b) 0.5, (c) 1, and (d) 10. The number of particles used is 10,000 with $\phi_p = 0.25$ , $\phi_f = 0.02$ , and $\theta = 92$ . The grey spheres indicate the monodisperse droplets with $\kappa = 0.4$ . The particles are colored according to the number of particles and droplets in the cluster, and the maximum number of the cluster is 22,501, which is the sum of particles (10,000) and droplets(12,501). . . . .	38

2.4	A 2D confocal microscopic image of capillary suspension with the secondary fluid marked with a fluorescent dye. The particles appear as the black circles with red outline, and the secondary fluids appear as the red circles. The system is composed of PMMA particles with 20 $\mu\text{m}$ diameter, glycerol as primary fluid, and paraffin oil as secondary fluid, and the three-phase contact angle is approximately 90 degrees. . . . .	45
3.1	The error( $\varepsilon_\theta$ ) between the intended contact angle( $\theta_c$ ) and the observed contact angle is plotted as a function of the intended contact angle. Three size ratios were used: 0.01(green square), 0.1(red triangle), 1(blue inverted triangle). When the $\theta_c$ is larger than 90 degrees, the error is almost zero for all the size ratios. . . . .	48
3.2	(a)A demonstration of how the observed contact angle deviates from the intended contact angle. (b)A demonstration of what happens when the contact angle goes below 90 degrees and still have low $\varepsilon_\theta$ . Red spheres are the particles and the grey spheres are the droplets. The red dotted outline indicates the peripheral of the droplet screened by the droplet. The black solid lines indicate the measurement of the observed contact angle. . . . .	50
3.3	(a)Maximum cluster size change according to $\kappa$ , and (b)the particle distribution on the droplet when $\phi_p=25$ vol%, $\phi_f=2$ vol%. . . . .	52
3.4	The depth-cut snapshots for different $\kappa$ values. Red and blue spheres indicate the particles that are in and out of the cluster, respectively, and the grey spheres indicate the droplets. . . . .	55

3.5	(a)The viscosity change according to $S = 1 - \phi_f$ and (b)the droplet distribution on the particle in the range of $\phi_f=0.25 - 2$ . The red circles in (a) indicate experimental results measured with a capillary suspension that is made of 20 $\mu\text{m}$ PMMA, glycerol as primary fluid, and paraffin oil as secondary fluid at $\phi_p=25$ vol%. The normalization of viscosity was based on the viscosity at $S=0.980$ . . . . .	56
3.6	The reduced viscosity versus kappa at a fixed $\phi_f$ of 2 vol %. Red squares indicate the simulation values with varying values of kappa and the blue solid line indicates the value attained from the experiment. . . . .	58
3.7	(a)the reduced cluster size, which is cluster size divided by the total number of particles and droplets present in the system. (b)the number of droplets on particle and (c)the number of particles on droplet for different solid volume fractions of 0.1, 0.15, 0.2, and 0.25, each represented by symbols of blue circle, red square, green triangle, and brown upside-down triangles, respectively. . . . .	60
3.8	The stress versus shear rate curve of the system with $\phi_p=25$ vol%, $\phi_f=2$ vol%, and $\kappa=0.4$ . Red squares and blue diamonds represent the systems with and without the polydisperse droplets, and the solid lines represent error bars. . . . .	63
3.9	The low shear viscosity versus secondary fluid volume fraction plot of the system with $\phi_p=25$ vol%, $\phi_f=2$ vol%, and $\kappa=0.4$ . Red squares and blue diamonds represent the systems with and without the polydisperse droplets, respectively. . . . .	66

3.10	The residual stress after resting for different mixing protocols. Shear only, hybrid, and random only in x-axis indicates shear only mixing, random motion and shear hybrid mixing, and random motion only mixing, respectively. . . . .	68
3.11	The depth-cut snapshots for different mixing protocols. Red and blue spheres indicate the particles that are in and out of the cluster, respectively, and the grey spheres indicate the droplets. (a)hybrid and (b)random motion only mixing protocols are depicted. $\phi_p=25$ vol%, $\phi_f=2$ vol%, and $\kappa=0.4$ . . . . .	70
3.12	(a)The original particle cluster (b)the particle cluster that has been extended to x, y, and z direction to check for the sample-spanning network across the periodic boundary. Red and blue spheres indicate the particles that are in a cluster and out of the cluster, respectively. Grey spheres indicate the droplets. . . . .	73
3.13	A graph of (a)viscosity( $\eta = \tau_{xy}/\dot{\gamma}$ ) and maximum cluster size, and (b)stress versus shear rate. The blue diamond and the red square in (a) indicate the viscosity and the maximum cluster size, respectively. The dotted red line in (b) indicates the projected value of the yield stress, which will be discussed later. $\phi_p=25$ vol%, $\phi_f=2$ vol%, $\kappa=0.4$ , $\theta_c=92$ . . . . .	75

3.14	The graph that shows the particle average velocity at each bin when the y domain is divided into 100 bins. The shear rates for (a) and (b) are 0.1 and 5.6, respectively. The graphs are the snapshots at strain 10. The dotted black line, blue diamond, and grey arrow indicate the imposed velocity, the particle velocity, and the imposed shear direction, respectively. On the background overlay image, red and blue spheres indicate the particles that are in the cluster and the particles that are not in the cluster, respectively. . . . .	77
3.15	(a)The local strain versus imposed strain below 1% local strain, and (b)the local stress versus local strain when the shear rate is 0.1. . . . .	80
3.16	(a)The local strain versus imposed strain and (b)the local stress versus local strain when the shear rate is 5.6. . . . .	81
3.17	The stress versus the strain at different shear rates. Black, blue, and red indicate the shear rates of 0.1, 0.18, and 0.32, respectively, and these shear rates belong to the freezing condition. Green indicates the shear rate of 5.6 where the freezing is not observed. . . . .	84
3.18	The oscillatory shear amplitude sweep graph at frequency of 10. Filled symbols indicate G' and empty symbols indicate G". Red circles indicate the random motion only mixing protocol and blue squares indicate the hybrid mixing protocol. $\phi_p=25$ vol%, $\phi_f=2$ vol%, $\kappa=0.4$ , $\theta_c=92$ . . . . .	86

3.19	The oscillatory shear frequency sweep graph at a strain of 0.01. Filled symbols indicate $G'$ and empty symbols indicate $G''$ . Red circles indicate the random motion only mixing protocol and blue squares indicate the hybrid mixing protocol. $\phi_p=25$ vol%, $\phi_f=2$ vol%, $\kappa=0.4$ , $\theta_c=92$ . . . . .	88
3.20	The Cole-Cole plot at different amplitudes of 0.025, 0.05, 0.1, 0.25, 0.5, 1, 2.5, 5, 10. . . . .	90
A.1	A demonstration of the variables used in the formulation process. Grey spheres are the particles and blue spheres are the droplets. $a$ , $R$ , $d$ , $x$ represent the particle radius, the droplet radius, the distance between the centers of the particle and the droplet, and the distance between the particle center and the cross-section where the particle and the droplet cross. . . . .	103

# Chapter 1

## Introduction

Suspensions are the materials of importance used in various industries including, not limited to, printing, coating, and battery slurry, for example. Depending on its usage, a suspension is processed in different ways and its rheological properties are of most importance. They are determined by the interactions between the components of the material, which result from the interaction between the particles, the interaction caused by additives, or the friction with the solvent. However, the usage of the additives needs to be done with care due to the side effects that may result from the additives themselves. Controlling the rheological properties is one thing, but controlling the final product at the end of the processing is another, and using additives just to control the rheological properties regardless of the final composition may result in an unwanted final product.

## 1.1 Capillary suspension

Recently, a capillary suspension, which dramatically increases the rheological properties by adding a trivial amount of immiscible secondary fluid to a suspension, was proposed[1] and many applications are explored. The capillary suspension refers to a ternary system composed of particles and two kinds of fluids that are immiscible. When one fluid is present in a small amount, the fluid droplets are present in between the particles to form a sample-spanning network. The fluid that is present in bulk is referred to as the primary fluid and the fluid that is added in a small amount is referred to as the secondary fluid. Upon mixing, the secondary fluid is located in between the particles, forming a capillary bond that exerts a capillary force between the particles. The capillary force in the capillary suspension is known to exert nearly 100 times larger force than the Van der Waals force.[1] Thus, the capillary suspension, compared to the binary suspensions prior to adding a secondary fluid, exhibits rheological properties, such as yield stress or viscosity, that are several orders higher than those of the binary suspensions.

The capillary suspension can be classified into two categories depending on which fluid, between primary and secondary fluids, preferentially wets the particle. If the secondary fluid preferentially wets the particle (contact angle  $\theta_c < 90$ ), the capillary suspension is in a pendular state, and if the primary fluid preferentially wets the particle (contact angle  $\theta_c > 90$ ), the capillary suspension is in a capillary state. The schematic illustrated in Fig. 1.1 demonstrates how the two different states of the capillary suspension are composed. The capillary suspensions, both pendular and capillary states, are formed at low volume fractions of the secondary fluid. When the secondary fluid volume fraction increases, the suspension goes through a transition to either agglomer-

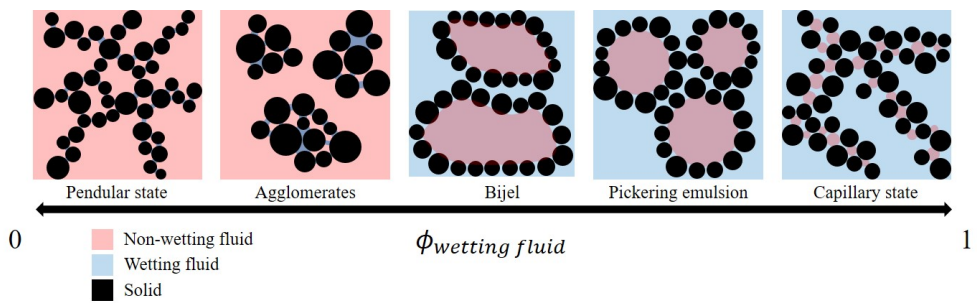


Figure 1.1 A schematic demonstrating different types of ternary systems containing one solid and two immiscible fluids. At very low or very high concentrations of wetting fluid, two different categories of capillary suspension are formed, a pendular state or a capillary state. At intermediate concentrations of wetting fluid, agglomerates, bijel, or Pickering emulsion is formed.

ates ( $\theta_c < 90$ ) or Pickering emulsion ( $\theta_c > 90$ ), eventually reaching Bijel when the two fluids have comparable volume fractions to each other.

The pendular state and the capillary state capillary suspensions have the same origin of the inter-particle force, the capillary force, but the microstructures are slightly different. In the pendular state, the secondary fluid forms capillary bridges in between the particles while in the capillary state, the particles are pinned into the secondary fluid droplets, mimicking the state of particles covering up the surface of the secondary fluid droplets. Both states of the capillary suspensions exhibit similar characteristics, though the concept of capillary state is relatively new and investigated less than the other. The amount of the secondary fluid and its wettability on the particle determines various types of the ternary system, such as Pickering emulsion, bijel, or capillary suspension.[2, 3] Capillary suspension forms only when the secondary fluid is present at a small amount, typically less than 5 vol %.

Using the capillary suspension, the rheological properties can be changed dramatically with as little as 10 vol% of solid content. Under a flow, the capillary network collapses and the suspension exhibits a strong shear thinning. In Fig. 1.2, the formation of capillary suspension is demonstrated. When the secondary fluid volume fraction is 0, the suspension behaves nearly as a Newtonian fluid. After adding a trivial amount of the secondary fluid, the viscosity at the low shear rate region dramatically changes, exhibiting yield stress and a strong shear thinning. As it can be seen from this demonstration, the strength of the capillary suspension is that one can achieve the desired rheological properties of the binary suspension by adding a small amount of the secondary fluid depending on the need. Also, by adjusting the amount of the secondary fluid used or the type of the secondary fluid, the rheological properties of the capillary suspension can be easily tuned. This is a great advantage due to the current

rising need for environmentally sustainable materials. In most of the materials used in the industries, there are many different additives involved in the recipe to achieve the desired rheological properties, and those additives are often considered non-friendly to the environment. By utilizing the capillary suspension, the desired rheological properties can be achieved while using environmentally friendly materials, such as oils and water. Also, because the secondary fluid that is used to tune the rheological property can be dried out at the end, the final composition of the product is barely influenced.

Several researches take advantage of such strength in various areas. For example, using the effect of the secondary fluid on the rheological properties, a study was conducted on tuning the rheological properties of the suspensions.[4] The effects of different mixing protocols on the structural and rheological properties of the capillary suspension were investigated as well.[5] Also, the yield stress increment due to the capillary network was utilized in designing the battery slurry to achieve a better edge shape. [6, 7, 8, 9] Capillary suspension was utilized in other industries as well including silver paste[10, 11] and 3D printing.[12, 13, 14] In the food industry, a small amount of water added to the chocolate was found to induce a shape resistance to heat while maintaining a low fat level[15, 16] and the capillary suspension was utilized in agri-food residues to open up possibilities for foods and ingredients uses.[17] Also, the pore size distribution control via the capillary network was studied to produce porous ceramics, [18, 19, 20] and porous glasses.[21, 22] The smart capillary suspension[23, 24, 25] that utilizes the selective presence of the secondary fluid in between the particles to deliver or locate the desired materials near the particles was introduced as well. The drying defect on the capillary suspension was also investigated and the drying defects, such as crack, were found to be mitigated upon utilizing capillary suspensions as well. [26, 27, 28] The concept of

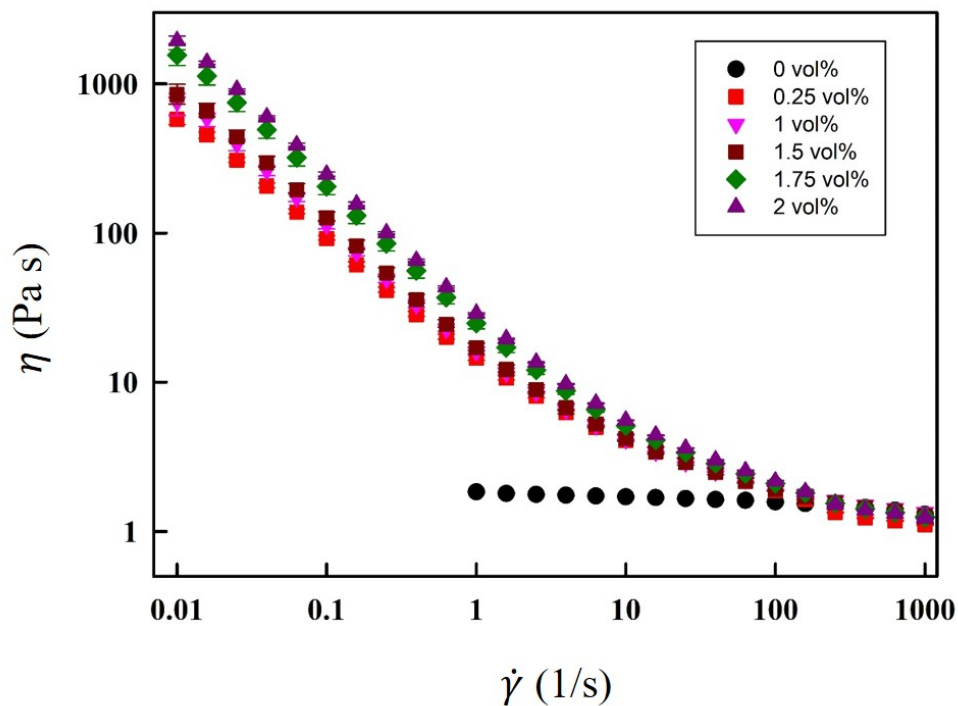


Figure 1.2 A rate sweep graph of experimentally measured viscosity of varying secondary fluid volume fractions. Black, red, pink, brown, green, and purple indicate secondary fluid volume fractions of 0, 0.25, 1, 1.5, 1.75, and 2 vol %, respectively. The system is prepared with spherical PMMA particles with 20  $\mu\text{m}$  diameter, glycerol as primary fluid, and paraffin oil as secondary fluid. The system is known to have approximately 90 degrees of three-phase contact angle.

ternary systems similar to the capillary suspension was also adopted in various polymer blend systems. [29, 30, 31, 32, 33, 34, 35]

While the aforementioned studies utilized the concept of capillary suspension for various applications, other studies explored the characteristics of capillary suspension. Some of the studies explored various morphological states of capillary suspensions with varying compositions using microscopy, and investigated yielding behavior under shear and oscillatory flows[36] and studied the relationship between different morphological characteristics to the yield stress.[37] A few other studies investigated the multi-tier yielding behavior of the capillary suspensions occurring under the oscillatory shear flows. [38, 39] Another investigated how the restructuring and the aging of the capillary network affect the rheological properties of the capillary suspension. [40] Additionally, several researches studied structural characteristics of the capillary suspension using microscopy and reproducing three-dimensional structures. [41, 42, 43] In limited settings, simulation studies were carried out to investigate the energies of different particle configurations formed by the particle and the secondary fluid droplets[44, 45] and the local interactions based on a small number of particles and fluids. [46] Some studies investigated the oscillatory shear flows in the medium amplitude oscillatory shear (MAOS) region and found that the capillary suspensions exhibit noninteger power law scaling. [47, 48] In another study, it was suggested that the capillary network can be formed via surface wetting of the secondary fluid on the particles. [49] However, the researches on the formation of the capillary suspension and the real-time tracing of the components of the capillary suspension (the particle and the secondary fluid droplet) under a flow have not been conducted yet.

In this study, we are proposing a simulation methodology that can track the particle and the secondary fluid droplet of the capillary suspension. The

methodology, in the long-term, aims to help investigate structural characteristics under flows and relate the structural characteristics to rheological properties to achieve a better understanding of the capillary suspension.

In the capillary suspension simulation, the most challenging and important aspect is that the free surface of the secondary fluid can be altered by the inter-particle interaction and the flow. When a number of secondary fluid droplets is present, it requires an excessive amount of simulation resources to numerically calculate all of the changes in free surfaces, and it is practically hardly achievable. In previous studies regarding a simulation of the capillary suspension, the analysis was limited to local interactions using a small amount of particles and fluids, and the flow properties or the rheological properties of the entire suspension were yet to be investigated. Such limitation is originated from the intense simulation cost related to calculating the free surface of the capillary suspension in detail, and an example will be given in the following section.

## 1.2 Solving the free interface

The description of the free surface formed in a ternary system has been investigated by many studies. [50, 51, 52] To demonstrate the difficulties involved in fully solving the free surface of the secondary fluid, the following exercise was conducted. When two immiscible fluids are at rest near the solid boundary, the pressure difference through the interface is determined by the interfacial tension and the curvature of the interface, which can be written as follows,

$$p_1 - p_2 = \Gamma \nabla \cdot \mathbf{n} \quad (1.1)$$

, where  $p_1$  and  $p_2$  are the pressure of each fluid,  $\Gamma$  is the interfacial tension, and  $\mathbf{n}$  denotes the unit normal vector of the interface of which direction is heading the fluid 2. ( $\nabla \cdot \mathbf{n}$  corresponds to the curvature) To calculate the shape of the interface, several restrictions should be applied to eqn. 1.1. For example, the contact angle between 3 phases (2 liquid and 1 solid) must be fixed, which is defined by the famous Young's equation. Another restriction can be possibly given by multiple sources, such as the gauge pressure condition ( $p_1 = p_2$ ) at the flat surface, or the volumetric conservation of one fluid phase. Though the interfacial shape can be determined by the governing equation and the restriction, the calculation of the acting forces on the interface is totally independent, as eqn. 1.1 only contains the information of static pressure distribution without the consideration of the most stable configuration of the solid boundary (or particle positions). In the determination process of the forces, the surface-excess energy of given interfacial shape should be expressed as a function of the boundary configuration.

In the case of the capillary suspension, the secondary fluid droplet forms the interface between two solid particles, and it acts as the interaction force between two particles. The determination of the interfacial shape and the cal-

culation of the forces between particles require complicated procedures which are given as follows. In this procedure, one may parameterize the shape of the interface with one or two degrees of freedom, and calculate the curvature in terms of the parameter(s) on the right-hand side of eqn. 1.1. As the gravitational effect can be neglected, the pressure difference at the left-hand side of eqn. 1.1 remains constant throughout the interface. However, the value of the constant should be determined by additional restriction, which comes from the aforementioned volumetric condition, which implies that the total volume of the droplet should be preserved independent of the interfacial shape. By solving eqn. 1.1 with the given parameter(s) under the volumetric restriction and the contact angle boundary condition the interfacial profile can be determined. However, the solution of the interaction force between the solid particle via the fluid droplet is still unknown.

As mentioned, to relate the interfacial profile and the interaction force, the total energy should be defined in terms of the distance between the particles. The total (excess) energy,  $E$  is given as follow,

$$E = (\Gamma_{S1} - \Gamma_{S2})A_{S2} + A_{12}\Gamma_{12} \quad (1.2)$$

, where  $\Gamma_{S1}$ ,  $\Gamma_{S2}$ , and  $\Gamma_{12}$  are the interfacial tension of solid-medium, solid-droplet, and medium-droplet respectively, while  $A_{ij}$  are the area of the corresponding interfaces. Once each area under the given interparticle distance is calculated by solving eqn. 1.1, the interparticle force, the derivative of the energy, can be represented by the distance, which is the so-called capillary force. However, the mathematical expression of the energy in terms of the distance is not analytic, so the real-time calculation of the particle dynamics of the capillary suspension is computationally tedious work.

In this study, the amount of calculation needed for tracking the free surface

of the secondary fluid was decreased dramatically by reducing the variables to describe the complex free surface to one variable, the contact angle  $\theta_c$ . In other words, by minimizing the calculation required to compute the changes in the free surface with the assumption that the secondary fluid maintains a spherical shape, we could use a sufficient amount of particles to calculate the rheological properties while maintaining a reasonable amount of calculation resources. In the process of this coarse-graining, we described the capillary interaction as the force that is derived from the surface energy due to the surface tension, which is a key factor of the capillary force. In chapter 2, a detailed explanation will be given to describe what assumptions were made to coarse-grain the complex capillary interaction, and what simulation methods were utilized to describe the behavior of the suspension under the flow. In chapter 3, focused analysis will be given on the structure and the flow behavior of the capillary suspension, especially on the structure freezing or yielding that occurs in the low shear rate condition. Through this study, a new simulation methodology to interpret the capillary interaction is suggested, and its performance and outcome will be explored.

### 1.3 Yield stress

One of the key characteristics of the capillary suspension is the presence of a yield stress. The yield stress is known to be found commonly in gel systems under both shear and oscillatory flows.[53, 54, 55, 56] The yielding behavior occurs when the microstructure formed by particle and additive interactions is strong enough to resist the outer forces that may otherwise cause the microstructure to collapse. The yield stress is defined as the stress at which the microstructure does yield to the flow, and it indicates the value of stress that a system or a microstructure can endure before yielding to the outer forces and collapsing. In experiments, the most common method is to observe the shear stress with respect to the shear rates and see if the shear stress does not increase with increasing shear rates at a low shear rate region. The plateau of the stress under increasing shear rate indicates the presence of yielding behavior in this case.

In a simple simulation system such as Brownian Dynamics simulation without hydrodynamic interactions or additional treatment of surface bond, however, the direct observation of the rigid particle or colloidal structure resisting the given shear flow has yet been observed, and the study of yielding behavior has been done on other aspects, such as in a start-up of shear flow.[57] In this study, the yield stress will be defined as the stress at which the system stops demonstrating its elastic behavior. In order to point out where that happens, the local strain and local stress were measured to observe the yielding behavior.

Note that the definition of the yield stress is an ongoing controversy. Some define the yield stress as the low shear rate plateau appearing in the flow curve while others define the yield stress as the overshoot maximum in the time sweep curve or the stress at which the particle structure begins to collapse in the time

sweep curve before the overshoot. It is unclear how the different definitions can relate to each other, and whether the yield stress can be given as a constant value is of another controversy. In this study, apart from the previous definitions, the yield stress is defined through the analysis on the local stress and strain, and the value of the stress at which the yielding behavior occurs is inferred from the local analysis and referred to as the yield stress.

## 1.4 Oscillatory shear

Oscillatory shear flows are commonly used to understand the microstructures of the suspensions. Upon applying a sinusoidal shear flow to a fluid, the measured stress also oscillates accordingly and oscillatory shear tests are performed to analyze how the material responds to the given oscillation.

$$\gamma(t) = \gamma_0 \sin(\omega t) \quad (1.3)$$

When an oscillatory shear is applied as above, where  $\gamma(t)$ ,  $\gamma_0$ , and  $\omega$  are the strain as a function of time, the maximum strain amplitude, and the frequency, respectively, the responding stress can be expressed as follows:

$$\sigma(t) = \sigma_0 \sin(\omega t + \delta) \quad (1.4)$$

$\sigma(t)$ ,  $\sigma_0$ , and  $\delta$  indicate the stress as a function of time, the maximum stress amplitude, and the phase angle, respectively. The oscillatory stress does not completely overlap with the given sinusoidal flow and the mismatch, or phase angle  $\delta$ , is used to determine the values of the storage and loss moduli, which are commonly referred to as  $G'$  and  $G''$ . Through the values of storage and loss moduli, the fluid of interest can be analyzed, as in how elastic or solid-like it is. In a linear viscoelastic regime, the values of  $G'$  and  $G''$  are independent of the given strain and such regime is commonly referred to as a small amplitude oscillatory shear regime. For higher strain values, the values of  $G'$  and  $G''$  start to exhibit a dependence on the given strain, and these regimes are called a medium amplitude oscillatory shear regime and a large amplitude oscillatory shear regime. Each regime is known to contain different information about the fluid of interest. As the strain reaches medium or large amplitude oscillatory

flows, the stress response deviates more from the sinusoidal curve, which makes it difficult to analyze the non-linear viscoelastic properties.

In the previous capillary suspension experiments, the capillary suspensions typically showed a gel-like behavior in the small amplitude oscillatory shear (SAOS) regime, meaning that  $G'$  and  $G''$  values formed a plateau with respect to the frequency while  $G'$  values were higher than those of  $G''$ . [1, 44] In the medium amplitude oscillatory shear (MAOS) regime, the capillary suspensions showed a non integer power law scaling, whereas it is usually expected to provide an integer power law scaling in other suspensions. [47, 48] One of the possible reasons for such non-integer power law scaling is that the particles are kinetically trapped in the cluster with a possibility of particle contacts. Some researches found that a highly concentrated capillary suspension ( $\phi_{solid} > 0.45$ ) exhibits multi-tier yieldings observed when conducting oscillatory shear tests, each of which was caused by distinct types of structure break-up under oscillatory shear. [38, 39] The origin of such multi-tier yieldings is not yet clarified, but the authors discuss the possible contributions of the thin primary fluid layer at the walls that causes wall-slips as well as the percolated network of capillary suspensions breaking into smaller flocs and agglomerates.

Among many different approaches trying to understand the non-linear viscoelastic properties, an approach of Sequence of Physical Processes was recently suggested. [58, 59, 60] In the SPP approach, the transient moduli of  $G'$  and  $G''$  is used to interpret the complex behavior and by combining the SPP interpretation with structural analysis, the relationship of the structure and the rheological property can be understood. In this study, we examined oscillatory flow behavior through the Sequence of Physical Processes.

## 1.5 Thesis outline

In chapter 2, the coarse-graining method used in this study will be thoroughly explained. First, the mathematical problem involved in the coarse-graining will be discussed in detail. Then, it will be explained how to adopt the concept of the contact angle hysteresis to describe the friction that a droplet experiences when in contact with a particle, which will be taken into account when combining the forces acting on the particles and the droplets. The other forces involved include the core-repulsion and hydrodynamic friction of the droplets, which will also be described in the following section. Then, the evolution of the particle and droplet positions under a shear flow will be explained followed by the simulation condition and analysis method used in this study. Also, there are a few experimental data involved in this study and the experiment methodology is also included in this chapter.

In chapter 3, four main sections will be displayed. First, the effect of the characteristic variables on the structural and rheological properties will be described. Then, the evaluation of the mixing protocol and sample-spanning network will be carried out. Next, utilizing the information gathered so far, the simple shear flow test will be carried out and the results will be analyzed. Lastly, the developed model capillary suspension will be subjected to an oscillatory shear test and its structural and rheological properties will be analyzed.

In chapter 4, the concluding remarks will be given where the discussion on the limitation and possible extensions of this methodology will be presented. Then, the summary and conclusion of this study will be given.

# Chapter 2

## Methodology

As mentioned previously, the most challenging aspect in describing the interaction between the particles and fluids in a ternary system is to track the change in the free surface. In this study, the free surface was forced to be a spherical shape, and the cost of analyzing the change in the free surface was dramatically reduced. Thus, the solid particle and the secondary fluid droplet, which will be referred to as the particle and the droplet, respectively, will all be described as spheres, and the primary fluid will be treated as the background fluid. The fluid, unless otherwise specified, refers to the droplet in this study.

This section is composed as follows. In section 2.1, the interaction between particles is derived from the coarse-grained interaction method between the particles and droplets. In the following sections 2.2-2.3, the force balance equation on the particles and droplets will be determined by defining the core-repulsion, pinning force, and drag force. The thermal motion is not considered because for  $\sim 10 \mu\text{m}$  sized particles and droplets used in this study, the effect of the thermal motion on the capillary force is trivial. Lastly, in section 2.4, the simulation

method to describe the dynamics of the suspension under the shear flow will be discussed. Then, section 2.5 is dedicated to explaining the simulation condition and analysis method used in this study.

## 2.1 Capillary interaction

In a ternary system, there are three different surface tensions, each of which represents the surface tension between the solid and the two fluids, or between the fluids. When a droplet interacts with a particle, excess energy proportional to the area of each interface arises, and the system tends to move in the direction to minimize the excess energy. In this situation, the free surface between the fluids is determined by the contact angle with the solid and the force balance in the interfaces. [61] Nevertheless, calculating all these interfacial force balances to determine the interface requires a massive calculation cost because it involves the coupled partial differential equations, which consider the flow inside a droplet, the interfacial flow, and the interfacial tension. In this study, to reduce the calculation cost, a coarse-graining to substitute such complexity into a single variable was adopted. Instead of considering the equations to determine the flow inside a droplet or the shape of the interface, the droplet is always maintained as a sphere, and the flow inside the sphere is neglected. This is demonstrated in Fig. 2.1. In Fig 2.1, the grey spheres are the particles and the blue spheres are the droplets. When the particles and the droplet is not in contact, they exhibit radii of  $a$  and  $a_f$ , respectively, as in Fig. 2.1(a). When the particles and the droplet come close to each other, an overlap is allowed as shown in Fig. 2.1(b). Here,  $r$  refers to the center to center distance between the particle and the droplet, and  $x$  refers to the distance between the center of the particle and the cross-section where the particle and the droplet cross. When there is an overlap between the particle and the droplet, a portion of the droplet volume is occupied by the particle, and the occupied volume is defined as an overlap volume,  $V_{ov}$ . To compensate for the lost volume of the droplet by  $V_{ov}$ , the droplet radius is increased, while the spherical shape is maintained

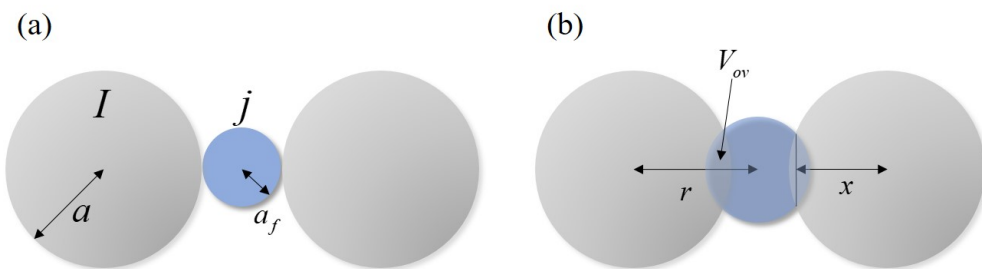


Figure 2.1 A schematic of (a) before and (b) after the contact when describing the coarse-grained potential. Grey ( $I$ ) and blue ( $j$ ) indicate the particle and the droplet, respectively.  $a$ ,  $a_f$ ,  $V_{ov}$ ,  $r$ ,  $x$  represent the particle radius, the droplet radius, the volume of the droplet overlapped by the particle, the distance between the centers of the particle and the droplet, and the distance between the particle center and the cross-section where the particle and the droplet cross. The area of the droplet (blue) is maintained to remain constant.

as mentioned. Thus, the only variable that determines the shape of the free surface is the droplet radius.

When  $V_{ov}$  is occupied by the particle as in Fig. 1(b), the volume occupied by the droplet is the difference between the original volume of the droplet and  $V_{ov}$ . Using the condition that the volume occupied by the droplet needs to be the same as the volume of the original droplet in Fig. 1(a), the new droplet radius in Fig. 1(b) can be calculated, which can be represented as following. The overlap volume,  $V_{ov}$ , when the droplet with a radius of  $a_f$  and the particle with a radius of  $a$  have the center-to-center distance of  $r$ , can be written as follows:

$$V_{ov}(r) = \begin{cases} \min(\frac{4\pi a_f^3}{3}, \frac{4\pi a^3}{3}) & 0 \leq r < |a_f - a| \\ f(x(r), a) + f(r - x(r), a_f) & |a_f - a| \leq r < a_f + a \\ 0 & a_f + a \leq r \end{cases} \quad (2.1)$$

$$f(x(r), a) = \pi \int_{x(r)}^a (a^2 - s^2) ds \quad (2.2)$$

where  $x$  indicates the distance between the particle center and the cross-section where the particle and droplet meet.  $x$  is defined as follows:

$$x(r) = \frac{r^2 + a^2 - a_f^2}{2r} \quad (2.3)$$

As mentioned above, the volume occupied by the droplet before and after the contact should be the same, which can be expressed as follows:

$$\frac{4}{3}\pi a_f^3 - V_{ov}(r) = V_0 \quad (2.4)$$

where  $V_0$  is the initial volume of the droplet before the contact. When the center-to-center distance between the particle and the droplet,  $r$ , is given, eqn.

(2.1-2.4) are coupled non-linear equations regarding  $a_f$ , and an iterative method can be applied to determine  $a_f$ . Also, it can be easily generalized for the cases of one droplet interacting with multiple particles as follows.

$$\frac{4}{3}\pi a_{f,j}^3 - \sum_{I \in j} V_{ov}(r_{Ij}) = V_0 \quad (2.5)$$

Here,  $a_{f,j}$  and  $r_{Ij}$  represent the radius of droplet  $j$  and the center-to-center distance between particle  $I$  and droplet  $j$ , respectively.  $I \in j$  indicates that the particle  $I$  and the droplet  $j$  are in contact. Unless otherwise specified, the subscripts for particles and droplets will be in the upper-case and the lower-case, respectively.

When the configuration and volume of all the particles and droplets are given, all the droplet radii can be determined by the aforementioned process. Moving forward, to determine the interaction between the particle and the droplet, the interfacial area of each interface can be determined by the following process.

For droplet  $j$  that is in contact with particle  $I$ , ( $r_{Ij} < a_{f,j} + a$  or  $j \in I$  in short) or for particle  $I$  that is in contact with fluid  $j$ , ( $I \in j$ )  $A_{S1}, A_{S2}, A_{dum}, A_{12}$ , which represent the interfacial areas of particle-primary fluid, particle-droplet, dummy, primary fluid-droplet, respectively, can be calculated. Here,  $A_{dum}$  is a dummy area which is the area of the droplet that is overlapped by the particle, and does not actually exist.

$$\begin{aligned}
A_{S1,I} &= 4\pi a^2 - \sum_{j \in I} A_{S2,j} \\
A_{S2,Ij} &= 2\pi a^2 \left( 1 - \frac{r_{Ij}^2 + a^2 - a_{f,j}^2}{2ar_{Ij}} \right) \\
A_{12,j} &= 4\pi a_{f,j}^2 - \sum_{I \in j} A_{dum,Ij} \\
A_{dum,Ij} &= 2\pi a_{f,j}^2 \left( 1 - \frac{r_{Ij}^2 + a_{f,j}^2 - a^2}{2a_{f,j}r_{Ij}} \right)
\end{aligned} \tag{2.6}$$

Thus, the total surface excess energy arising from the system for all particles  $I$  and droplets  $j$  can be written as follows.

$$\begin{aligned}
E_{\text{total}} &= \sum_{(I,j)} E_{Ij} = \\
&\sum_j \left( \begin{aligned} &\Gamma_{S2} \sum_{I \in j} A_{S2,Ij}(r_{Ij}) \\ &+ \Gamma_{12} \left( 4\pi a_{f,j}(r_{Ij})^2 - \sum_{I \in j} A_{dum,Ij}(r_{Ij}) \right) \end{aligned} \right) \\
&+ \Gamma_{S1} \sum_I \left( 4\pi a^2 - \sum_{j \in I} A_{S2,Ij}(r_{Ij}) \right)
\end{aligned} \tag{2.7}$$

$\Gamma_{S2}$ ,  $\Gamma_{12}$ , and  $\Gamma_{S1}$  are the surface tension of the solid-primary fluid, primary fluid-droplet, and particle-primary fluid interface, respectively. To roughly examine how the total energy,  $E_{\text{total}}$ , changes with respect to the center-to-center distance between the particle and the droplet, the surface tension at each interface was assumed to be equal, just for this analysis. ( $\Gamma_{12} = \Gamma_{S1} = \Gamma_{S2}$ ) Then,  $E_{\text{total}}$  is simplified as follows.

$$E_{\text{total}} = \Gamma A_{\text{total}} \tag{2.8}$$

Here,  $\Gamma$  is the surface tension at all interfaces and  $A_{\text{total}}$  is the summation of all the interfacial areas. When a droplet forms an interface with particles,  $A_{\text{total}}$  changes according to how far and how many the particles are located with respect to the droplet. In Fig. 2.2, when the droplet is in contact with 1, 2, or 3 particles, the relative changes of the surface area,  $\Delta A_{\text{total}}(r) = A_{\text{total}}(r) - A_{\text{total}}(r \rightarrow \infty)$ , is plotted as a function of center-to-center distance,  $r$ , between the droplet and the particles. When multiple particles interact with a droplet, all the center-to-center distances were assumed to be equal.

$\Delta A_{\text{total}}$  is plotted when the droplet to particle size ratio is 1 in Fig. 2.2(a) and the size ratio is 0.4 in Fig. 2.2(b). The size ratio of the droplet with radius  $a_f$  and the particle with radius  $a$  is referred to as  $\kappa$ , that is,  $\kappa = a_f/a$ . In both cases,  $\Delta A_{\text{total}}$  begins to change when the center-to-center distance becomes smaller than the contact distance, and a minimum is observed. The distance at the minimum of  $\Delta A_{\text{total}}$  appears to vary depending on the number of particles in contact with the droplet, and as the more particles are interacting, the further the distance of the minimum energy becomes. Through this analysis, the tendency of the potential curve when a droplet is in contact with one or more particles can be understood. It is worth noting that the potential derived from this method shows an attractive force when the droplet comes to contact with other particles, followed by the potential well where the capillary bond is the most stable. Then, as the center-to-center distance becomes smaller, the potential escapes from the potential well and develops rapidly, reaching a repulsive force eventually, as can be seen in Fig. 2.2(b).

Prior to deriving the evolution equations for particles and droplets from the total energy, all the equations were non-dimensionalized by introducing the following characteristic variables for length(coordinate), energy, time, and shear rate.

$$\begin{aligned}
 \mathbf{r} &= a\mathbf{r}^* \\
 E &= \frac{\Gamma_{12}a^2}{C}E^* \\
 t &= C\frac{6\pi\mu a}{\Gamma_{12}}t^* \\
 \dot{\gamma} &= \frac{1}{C}\frac{\Gamma_{12}}{6\pi\mu a}\dot{\gamma}^*
 \end{aligned} \tag{2.9}$$

$a$  and  $\mu$  are the particle radius and the viscosity of the primary fluid (back-

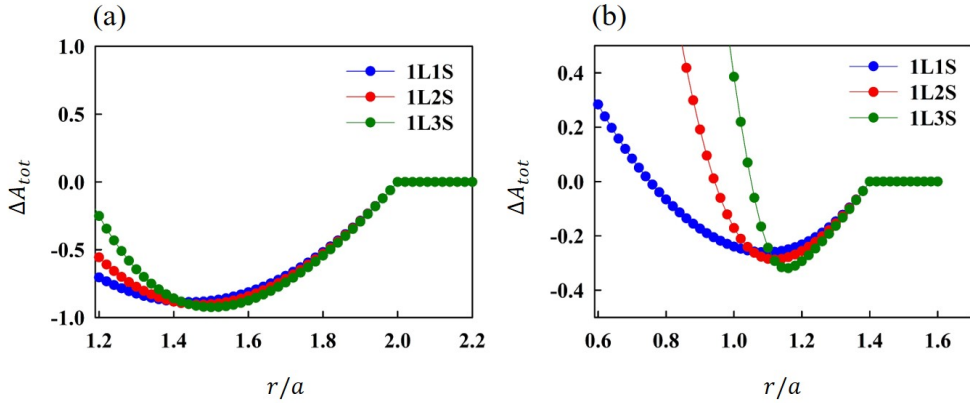


Figure 2.2 At the contact angle,  $\theta_c = 90$ , the total surface area change with respect to the center-to-center distance is plotted for the cases where the droplet to particle size ratio is (a)1 and (b)0.4. Blue(1L1S), red(1L2S), and green(1L3S) circles represent the droplet interacting with 1, 2, and 3 particles, respectively.  $r/a$  is the dimensionless distance, where  $r$  is the distance between the centers of droplet and particle, and  $a$  is the radius of the particle.

ground fluid), respectively. The characteristic variable for energy is related to the surface excess energy on the area equal to  $a^2$  and the characteristic variable for time is based on the time it takes for a particle with radius  $a$  to move a distance  $a$  by the Stokes drag. A constant,  $C$ , which is equal to  $10^3$ , is introduced to compensate for the variable range where a meaningful change appears in the simulation. The characteristic variable for energy is more than  $10^5$  times larger than the thermal energy,  $k_B T$ , and thus the Brownian motion is not accounted for in this study. The superscript \* indicates the non-dimensional variable and it will be omitted from here on, thus all the variables are non-dimensional.

The force  $F_{Ij}$  exerted on particle  $I$  by droplet  $j$ , after differentiating the energy in eqn. (2.7) with respect to the center-to-center distance  $r_{Ij}$ , can be written as follows:

$$\mathbf{F}_{Ij}^{\text{cap}} = -C \nabla_{Ij} r_{Ij} \left( \begin{array}{l} \cos \theta_c \pi \left( \frac{r_{Ij}^2 + a_{f,j}^2 - 1}{r_{Ij}^2} - 2a_{f,j} \sum_{K \in j} \left( \frac{1}{r_{Kj}} \right) \frac{\partial a_{f,j}}{\partial r_{Ij}} \right) \\ + \pi \frac{\partial a_{f,j}}{\partial r_{Ij}} \left( 8a_{f,j} - 4N_b a_{f,j} + \sum_{K \in j} \left( \frac{r_{Kj}^2 + 3a_{f,j}^2 - 1}{r_{Kj}} \right) \right) \\ + \pi a_{f,j} \frac{r_{Ij}^2 + 1 - a_{f,j}^2}{r_{Ij}^2} \end{array} \right) \quad (2.10)$$

where  $N_b$  indicates the number of particles that are in contact with droplet  $j$ . Also, the newly introduced variable,  $\theta_c$ , is defined by Young's equation. ( $\Gamma_{12} \cos \theta_c = \Gamma_{S1} - \Gamma_{S2}$ ) The first term in eqn. (2.10) represents the gradient of the surface excess energy with respect to the relative preferences between the three phases, primary, secondary fluid, and the solid particle, which are governed by the contact angle  $\theta_c$ . It can change the sign depending on the contact angle, as well, it can be trivial when the affinities of the solid particle to both fluids are identical. The second and third terms of eqn. (2.10) correspond to the total areal change of the liquid-liquid surface. (Note that the total energy

in eqn. (2.9) is normalized in terms of the interfacial tension between the fluids.) Thus, the force induced by the capillary interaction is not trivial even if the contact angle is exactly 90-degree. In a previous study, using the equation  $F^{\text{cap}} = 2\pi r\Gamma\cos\theta$  and the values of  $r = 10^{-6}\text{m}$ ,  $\Gamma = 50 \times 10^{-3}\text{N/m}$  and  $\cos\theta \sim 1$ , the capillary force exerted is approximately 300 nN. Using the force equation derived above and using the same parameters, we get the capillary force of 90 nN, which seem to be in the same order of magnitude.

Note that when multiple particles are contacting and overlapping on a droplet, the energy change by a small change in  $r_{Ij}$  is different from when only one particle is contacting the droplet, due to the terms related to  $N_b$  and the summation over the particles contacting with the fluid  $j$ ,  $\sum_{K \in j}$ . It is already shown in Fig. 2.2, with regard to the total energy. As eqn. (2.10) is the force between the particle and the droplet, the total force exerted on each particle/-droplet should be calculated by taking a summation of eqn. (2.10) as follows.

$$\mathbf{F}_I^{\text{cap}} = \sum_{j \in I} \mathbf{F}_{Ij}^{\text{cap}} \quad (2.11)$$

$$\mathbf{F}_j^{\text{cap}} = - \sum_{I \in j} \mathbf{F}_{Ij}^{\text{cap}} \quad (2.12)$$

By the force defined above, the particle and the droplet move in the direction that minimizes the total energy shown in eqn. (2.7).

## 2.2 Droplet friction on the particle surface

When a droplet comes into contact with a particle, a force is applied between the particle and the droplet in the direction that minimizes the surface excess energy by the force defined in eqn. (2.10). Nevertheless, this force does not affect the tangential movement of the droplet. In actual settings, a liquid droplet cannot slip freely on a rough surface due to the contact angle hysteresis, which is the pinning force resistant to tangential movement. [62] To bring about the effect of the pinning force in the simulation, the advancing and receding contact angle according to the solid surface condition needs to be defined and the change in liquid free surface needs to be tracked. In this study, however, the droplet shape is fixed as a sphere, and thus the direct realization of the contact angle hysteresis is impossible. Instead, a surface bond is introduced to prevent the freely slipping droplet on the particle surface.

To achieve this, when a particle and a droplet come into contact, the bonding point on the solid surface is recorded and when the droplet escapes the bonding point, a recovering force is applied in the tangential direction on the particle surface. This force can be written as follows:

$$\mathbf{F}_{Ij}^{\text{bond}} = K(\mathbf{a}_{Ij}^o - \mathbf{a}_{Ij}) \quad (2.13)$$

where  $\mathbf{a}_{Ij}$  is the relative location of the droplet  $j$  contacting the particle  $I$ , and  $\mathbf{a}_{Ij}^o$  is the  $\mathbf{a}_{Ij}$  when the two initially contact.  $\mathbf{F}_{Ij}^{\text{bond}}$  is proportional to the temporal coordinate difference of the particle  $I$  and the droplet  $j$  and the proportional constant is  $K$ . The value of  $K$  was set in the simulation as  $10^4$ , which is high enough to prevent the tangential slip of the droplet by providing a sufficient amount of the recovery force. Meanwhile, to prevent the numerical instability, the value of  $K$  was not further increased. Note that the value of  $K$  in

reality would depend on the contact angle, but to avoid additional complexity, we have fixed the value of  $K$  in our simulation.

$\mathbf{a}_{Ij}$  is given as follows.

$$\mathbf{a}_{Ij} = \frac{\mathbf{r}_j - \mathbf{r}_I}{r_{Ij}} \quad (2.14)$$

The dislocation of the initial bonding point,  $\mathbf{a}_{Ij}^o$ , due to tangential movement on the particle surface or the break-up of the bond was not considered. The bond will naturally break when the radial distance between the particle and the droplet,  $r_{Ij}$ , becomes larger than  $1 + a_{f,j}$  due to other forces. The force defined for the particle  $I$  and the droplet  $j$  can be summed in the same way as in eqn. (2.11,2.12). That is,  $\mathbf{F}_I^{\text{bond}} = \sum_{j \in I} \mathbf{F}_{Ij}^{\text{bond}}$  and  $\mathbf{F}_j^{\text{bond}} = - \sum_{I \in j} \mathbf{F}_{Ij}^{\text{bond}}$ .

The pinning force,  $\mathbf{F}_I^{\text{bond}}$ , acts in the tangential direction on the particle surface and causes a torque on the particle. (eqn. (2.15))

$$\mathbf{T}_{Ij} = \mathbf{a}_{Ij} \times \mathbf{F}_{Ij}^{\text{bond}} \quad (2.15)$$

When the rigid body rotation of the particle is calculated in a later part, the torque defined above will be used. On the other hand, the droplet does not act like a rigid body and the rotation of the droplet is not accounted for. The total torque acting on the particle  $I$  is defined as the summation of the torque caused by all the droplet  $j$  that are in contact with the particle  $I$ . ( $\mathbf{T}_I = \sum_{j \in I} \mathbf{T}_{Ij}$ )

## 2.3 Core-repulsion and hydrodynamic friction

To prevent the overlap of the particles due to the flow or other forces, a hard-core repulsion force was implemented. To do this, the potential-free method was used. [63, 64] When the particles  $I$  and  $J$  are in overlap, each particle is moved back to the contact point. Here, the displacement of the overlapped particles can be written as follows.

$$\Delta \mathbf{r}_I^{\text{overlap}} = \frac{1}{2} \frac{\mathbf{r}_{IJ}}{r_{IJ}} (r_{IJ} - a_I - a_J), \quad r_{IJ} < a_I + a_J \quad (2.16)$$

When the overlapped particles,  $I$  and  $J$ , are moved back as much as  $\Delta \mathbf{r}_I^{\text{overlap}}$ , the surface of each particle is in contact with that of the other. Here,  $\mathbf{r}_{IJ} = \mathbf{r}_J - \mathbf{r}_I$ ,  $r_{IJ} = |\mathbf{r}_{IJ}|$ , and  $a_I$  and  $a_J$  are the radii of the particles  $I$  and  $J$ , respectively. In the real-world, the droplet coalescence can occur when the droplets collide, or the droplet break-up can occur due to flow. However, the consideration of the droplet coalescence or break-up requires an excessive amount of free parameters to be involved, and therefore, they are neglected in this study. In addition, the droplet is present at only 2 vol% and the collision between droplets rarely happens. Yet, there are a few cases where the droplets collide with each other on the particle surface. When this happens, the overlap is prevented using the method described in eqn. (2.16). Nevertheless, whether the droplet overlap is prevented or not, the effect of the droplet overlap is negligible.

When the particles and droplets are moved by a flow, the Stokes' drag force [65] was applied while neglecting multi-body hydrodynamic interaction (HI). Under these assumptions, the hydrodynamic friction forces  $\mathbf{F}^h$  acting on the particle  $I$  and the droplet  $j$  are given as follows.

$$\mathbf{F}_I^h = \xi_p(\mathbf{v}_I^\infty - \mathbf{v}_I) \quad (2.17)$$

$$\mathbf{F}_j^h = \xi_f(\mathbf{v}_j^\infty - \mathbf{v}_j) \quad (2.18)$$

Here,  $\xi_p$  and  $\xi_f$  are the hydrodynamic friction coefficient for the particle and the droplet, respectively.  $\mathbf{v}_I^\infty$  and  $\mathbf{v}_j^\infty$  are the background fluid velocity at the center of the particle and the droplet, respectively.

Neglecting the multi-body HI is one of the biggest assumptions made in this study and it was done simply to reduce the simulation cost. Yet, it is inferred that such an assumption would not undermine the observed physical phenomena significantly since the strongest and most important force in the capillary suspension is the capillary force between the particles and droplets. The hydrodynamic friction coefficients used in Stokes' equation for the particle( $\xi_p$ ) and the droplet( $\xi_f$ ) that were non-dimensionalized by eqn. (2.9)( $\xi_p = 6\pi\mu a\xi_p^*$ ) are as follows.

$$\xi_p = 1 \quad (2.19)$$

$$\xi_f = a_f \left(1 + \frac{1}{2 + 3\tilde{\mu}}\right)^{-1} \quad (2.20)$$

Here, eqn. (2.20) describes the friction coefficient of the Stokes drag force that a fluid droplet experiences inside the other bulk fluid, and  $\tilde{\mu}$  is the relative viscosity of a droplet(secondary fluid in this study) to a bulk fluid(primary fluid in this study), and  $a_f$  is the radius of the fluid droplet. [61] According to the equation, as  $\tilde{\mu}$  becomes higher, which implies being more like solid, the hydrodynamic friction coefficient of the droplet becomes similar to eqn. (2.19).

Note that Stokes' solution is only valid when the hydrodynamic interactions among the droplets and the particles are negligible. However, in this simulation,

the distances between the particles are close enough to affect the other particles, especially when they form a gel structure. Even more, as the penetration of droplets into the solid particle is allowed, Stokes' solution may lead to the wrong movement of the particle. The correction of this problem is also related to the consideration of hydrodynamic interaction, which will be discussed later.

## 2.4 Evolution of particle and droplet positions under shear flow

In the simulation, the particles and droplets move according to the balance equations derived in the previous sections. The capillary suspension involves the particles and droplets that are a few micrometers and above, and the inertial effect can be neglected because the effect of the capillary interaction is much larger even for the particle of a few micrometers and above. In such an overdamped condition, the force balance becomes as follows.

$$\mathbf{0} = \mathbf{F}_I^{\text{cap}} + \mathbf{F}_I^{\text{bond}} + \mathbf{F}_I^h + \mathbf{F}_I^{\text{overlap}} \quad (2.21)$$

$$\mathbf{0} = \mathbf{F}_j^{\text{cap}} + \mathbf{F}_j^{\text{bond}} + \mathbf{F}_j^h + \mathbf{F}_j^{\text{overlap}} \quad (2.22)$$

Eqn.(2.21,2.22) describes the force balance for the particle  $I$  and the droplet  $j$ , respectively. By substituting eqn. (2.11-2.18) to eqn.(2.21,2.22) and arranging for  $\mathbf{v}_I$  and  $\mathbf{v}_j$ , the evolution equation for all the particle and droplet positions can be derived through the explicit Euler time integration.

$$\Delta \mathbf{r}_I = \left( \mathbf{v}_I^\infty + \frac{1}{\xi_p} \left( \mathbf{F}_I^{\text{cap}} + \mathbf{F}_I^{\text{bond}} \right) \right) \Delta t + \Delta \mathbf{r}_I^{\text{overlap}} \quad (2.23)$$

$$\Delta \mathbf{r}_j = \left( \mathbf{v}_j^\infty + \frac{1}{\xi_f} \left( \mathbf{F}_j^{\text{cap}} + \mathbf{F}_j^{\text{bond}} \right) \right) \Delta t + \Delta \mathbf{r}_j^{\text{overlap}} \quad (2.24)$$

Here,  $\Delta t$  is the simulation time interval and  $\Delta \mathbf{r}_I$  and  $\Delta \mathbf{r}_j$  are the displacement of the center position of the particle  $I$  and the droplet  $j$ , respectively.

The torque acting on the particle defined in eqn. (2.15) is in balance with the rotational friction force caused by the background fluid, and the orientation difference of the particle,  $\Delta \varphi_I$ , is given as follows.

$$\Delta\varphi_I = \left( \frac{1}{2}\nabla \times \mathbf{v}_I^\infty + \frac{3}{4}\mathbf{T}_I \right) \Delta t \quad (2.25)$$

The number 3/4 comes from the ratio of translational( $6\pi\mu a$ ) and rotational( $8\pi\mu a^3$ ) friction coefficients.

$\mathbf{v}^\infty$ , the background fluid velocity, is set as  $\mathbf{v}^\infty(\mathbf{r}) = \dot{\gamma}y\mathbf{e}_x$  to describe the simple shear flow. Also, to describe the suspension in a finite simulation box, the Lees-Edwards periodic boundary condition was employed to achieve a continuous velocity distribution under the shear flow. However, as will be discussed in later sections, when freezing occurs in the low shear rate regime, the Lees-Edwards boundary condition causes an artificial rupture in the particle network.

## 2.5 Simulation condition and analysis method

When the particle simulation is proceeded with the capillary interaction defined above, the relevant dimensionless control factors are  $\phi_p$ ,  $\phi_f$ ,  $\kappa$ , and  $\theta_c$ , which are particle volume fraction, secondary fluid volume fraction, fluid droplet to particle size ratio, and contact angle, respectively. Throughout the study,  $\phi_p$  was fixed at 25 vol% to enhance a smooth formation of the network structure while using dozens of thousands of particles and droplets. When measuring the structural and rheological property changes according to  $\phi_f$ , the range of  $\phi_f$  was 0 - 2 vol%, and when investigating the yielding behavior, the value of  $\phi_f$  was fixed at 2 vol%. The settings for  $\kappa$  and  $\theta_c$  will be discussed below.

As the free surface was enforced as spherical in this study, the pendular bridge cannot be reproduced for low  $\theta_c$  and the bond shape between the particle and the droplet will differ from the actual shape below a certain value of  $\theta_c$ . This will be discussed in detail in section 3.1.1.

The size ratio  $\kappa$  is defined as the radius ratio of the droplet to the particle. Even though the droplet radius can differ in the real world, they were assumed to have the same size distribution in this study for a simplified analysis. The changes in the sample-spanning network according to the change in  $\kappa$  will be discussed in section 3.1.2.

The size distribution of droplets was also considered because in real world, the droplet sizes are different for each droplet. By changing the size distribution, how the polydispersity affects the rheological and structural properties is examined. At a fixed  $\kappa$ , the size distribution was given as a normal distribution with the average at the value of  $\kappa$ . The lower limit was set to  $\kappa=0.1$  because when the droplets less than 0.1  $\kappa$  are iterated for the radius calculation, in a few cases, the iteration does not converge and caused a numerical instability.

In the simulation, the number of particles was fixed at 10,000 and the number of droplets, which vary according to  $\phi_f$  and  $\kappa$ , ranges from several thousands to several tens of thousands. For example, when  $\kappa = 0.4$ ,  $\phi_f = 2$  vol%, there are 12,501 droplets. Due to the neglect of thermal motion, the initial configuration after the initial distribution is given as deterministic. To accomplish reproducible simulation outcomes, the initial configuration is defined as follows.

We made initial configurations using three different conditions: shear only, random motion and shear, and random motion only. For the case of using shear exclusively, the mixing protocol is as follows. First, all the particles are randomly placed in the three-dimensional cube and the shear rate of  $10^1$  is applied till the strain of 100. Then, the shear rate of  $10^{-1}$  is applied till the strain of 10 to stabilize the disturbed structure from the high shear rate, followed by a rest without shear until the shear stress is relaxed sufficiently.

For the random motion and shear case, the initially randomized particles and droplets are subjected to a random motion of  $5^{-2}$  for dimensionless time of 1000. The value of random motion is not practical as the same level of thermal motion would require tens of thousands degrees Celcius temperature, and such value was used just to promote a random mixing condition. Then, the low shear rate of  $10^{-1}$  is applied till the strain of 10, followed by a rest without shear until the shear stress is sufficiently relaxed. The reason for applying the low shear after initial mixing with high shear is to induce the freezing behavior that will be discussed later.

For the random motion only case, the steps above are repeated, only without the application of the low shear after the initial mixing. This case was investigated to examine the residual stress level, which will also be discussed later.

The initial mixing with shear only protocol according to the applied shear

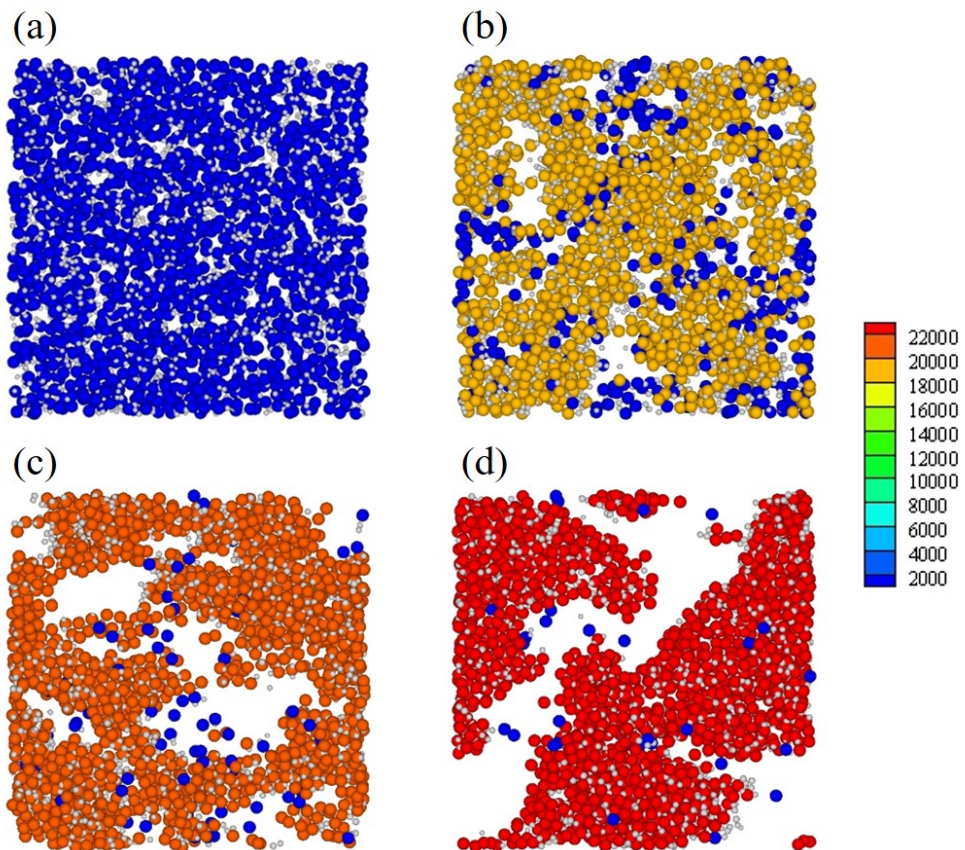


Figure 2.3 The depth-cut snapshots of the particles and droplets during the initial mixing with shear rate of  $10^1$  at strains of (a) 0, (b) 0.5, (c) 1, and (d) 10. The number of particles used is 10,000 with  $\phi_p = 0.25$ ,  $\phi_f = 0.02$ , and  $\theta = 92$ . The grey spheres indicate the monodisperse droplets with  $\kappa = 0.4$ . The particles are colored according to the number of particles and droplets in the cluster, and the maximum number of the cluster is 22,501, which is the sum of particles (10,000) and droplets(12,501).

is demonstrated in Fig. 2.3. As mentioned earlier, a total of 10 strain is applied during the initial mixing stage and the images in Fig. 2.3(a), (b), (c), and (d) depict the snapshots at strains 0, 0.5, 1, and 10, respectively. The particles and droplets are initially randomly dispersed in the simulation window as in Fig. 2.3(a) before the flow was given. After a short while, when a strain of 0.5 is applied, a network that involves more than 85% of the particles and droplets is formed. When additional 0.5 strain is applied, the cluster size got bigger but the rate of the cluster size growth is lower than before due to the reduced amount of free particles and droplets that can be added up to the cluster. At the end of 10 strain flow, more than 22,000 particles and droplets out of 22,501 available are in one cluster, forming a sample-spanning network. The network formation aspect is somewhat similar when using random motion for initial mixing, however, the final structure looks more like fractal structure with branches. Depending on the mixing protocol, this structure in Fig. 2.3(d) is exposed to low shear or not to induce the local freezing.

The structure achieved after these initialization steps are used as the initial configuration for all the simulations. As mentioned in section 2.2, because the rotation of the droplet is not considered while that of the particle is only considered, the torque may not be conserved. To prevent the imbalance, the bond points,  $\mathbf{a}_{Ij}$ , are reassigned every 1 of time.

At the end of each initial mixing, the existence of the sample-spanning network was examined. In capillary suspension, the sample-spanning network is the key to producing gel-like rheological properties, such as yield. Because of the size of the domain we can explore in the simulation, most of the particles existing in the same cluster cannot simply conclude to the existence of the sample-spanning network. In order to genuinely examine for the presence of the sample-spanning network, we need to examine if the periodic network is inter-

connected at each end of the domain. To do this, the coordinates of particles and droplets were copied and pasted to extend the structure in each direction. If the original structure is in  $(x, y, z)$  coordinate, the box length,  $bl$ , which indicates the length of each  $x, y, z$  coordinates, is added in each direction. As a result, new coordinates of  $(x, y, z)$ ,  $(x + bl, y, z)$ ,  $(x, y + bl, z)$ ,  $(x, y, z + bl)$ ,  $(x + bl, y + bl, z)$ ,  $(x + bl, y, z + bl)$ ,  $(x, y + bl, z + bl)$ , and  $(x + bl, y + bl, z + bl)$  are defined for each particle and droplet. Using the new coordinates, the distances and forces are calculated again to test if the structure is sample-spanning. If the new coordinates produce a network size that is 8 times larger than the original network, it means the network is sample-spanning.

The simple shear simulation was performed from  $10^{-1}$  to  $10^3$  of shear rates. To efficiently compute the ballistic motion of non-Brownian particles, the time-interval,  $\Delta t$ , was set to  $10^{-5}$  at low shear rates( $10^{-1}$ - $10^1$ ),  $10^{-6}$  at moderate shear rates( $10^1$ - $10^2$ ), and  $10^{-7}$  at high shear rates( $10^2$ - $10^3$ ). The simulation was performed until the imposed strain reached 10. The value of  $\Delta t$  was examined via a consistency test, where the same initial configuration was sheared with different  $\Delta t$  values, and it was determined that below  $\Delta t$  of  $10^{-5}$ , the results were within the error range.

After the suspension is formed, or while it flows under the shear flow, we analyzed the structure, the average particle stress, the local particle velocity profile, and the local particle stress profile. The structural information is mainly achieved through the bond number distribution, which measured the distribution of droplets on a particle, or of particles on a droplet. This will be discussed further in section 3.1.

The particle stress,  $\boldsymbol{\tau}^p$ , is given as the Batchelor's expression[66] for all the point pairs,  $\mathbf{r}_i$  and  $\mathbf{r}_j$  that generate the force.

$$\boldsymbol{\tau}^p = -\frac{1}{V} \sum_{(i,j)} \mathbf{r}_{ij} \mathbf{F}_{ij} \quad (2.26)$$

Here,  $V$  is the volume of the simulation domain and  $\mathbf{F}_{ij}$  is the force acting between two points,  $\mathbf{r}_i$  and  $\mathbf{r}_j$ . Using this, the shear stress, or the viscosity, under a shear flow was measured and the results will be discussed in detail in section 3.3.1.

In addition, to analyze the local strain and local stress, the simulation domain was divided into 100 slabs in shear-gradient direction and the average value of each variable was measured in each slab. The measured local particle velocity at time  $t$  for  $k$ th slab,  $\mathbf{v}_k^p(t)$ , is given as follows.

$$\mathbf{v}_k^p(t) = \frac{1}{N_{\text{slab}_k}} \sum_{i, \mathbf{r}_i(t) \in \text{slab}_k} \frac{\mathbf{r}_i(t) - \mathbf{r}_i(t - \Delta t)}{\Delta t} \quad (2.27)$$

Here,  $N_{\text{slab}_k}$  indicates the number of particles or droplets involved in the  $k$ th slab, regardless of their kind.

The local stress is measured in a similar way, but as it is defined by the displacement vector,  $\mathbf{r}_{ij}$ , instead of being defined on the positions as in the local particle velocity, it is calculated based on the contribution of each line segment belonging to different slabs. A detailed explanation can be found in the references [67, 68].

Using the velocity profile according to the time and location calculated above, the local shear rate and the local strain can be determined. The local particle shear rate can be defined by numerical differentiation of the local particle velocity, however, the direct numerical differentiation may cause large errors because of the non-trivial noise in the local particle velocity. Therefore, the Savitzky-Golay filter[69], which provides locally smooth and continuous

polynomial fitting for noisy data, was used for the local particle velocity in calculating the local shear rate. The local shear rate calculated above is integrated through Euler integration to get the local strain. The analysis of the aforementioned local properties will be investigated further in section 3.3.2.

## 2.6 Experimental

To compare the simulation results to the experimental results, a simple capillary suspension model system was experimented. In the experiment, the system was composed of 20  $\mu\text{m}$  PMMA (SSX-120, Sekisui Plastics Co., Ltd., Japan) as a particle, glycerol (Daejung Chemicals and Metals Co., Ltd., Korea) as a primary fluid, and paraffin oil (KF-96, Shin-etsu, Japan) as a secondary fluid.

Initially, 25 vol % of PMMA particles were dispersed in glycerol using a magnetic stirrer overnight. Then, the required amount of silicone oil (0 to 2 vol %) was added drop by drop while the PMMA/glycerol suspension was stirred under an overhead stirrer at 1000 rpm. The amount of sample was kept sufficient to have the stirrer completely submerged in the sample during the mixing, and the type of the stirrer used was a dissolver type. After all of the secondary fluid is added, the sample was stirred at 2000 rpm for 60 seconds.

The rheological properties were measured with AR-G2 stress-controlled rheometer (TA Instruments, U.S.A.) using a cross-hatched 40 mm parallel plate at 25 degrees Celsius. To prevent slip, a sand paper (P1000 degree) was also placed on top of the peltier as well. The measurement gap was 1000  $\mu\text{m}$  and the sample was rested for 180 seconds after the loading process. An ascending shear rate sweep was conducted with shear rates ranging from 0.01 1/s to 1000 1/s. The rate sweep test was repeated more than 3 times for each composition. The result of this experiment is presented in Fig. 1.2.

For the visualization, a fluorescent dye (Nile red, Sigma-Aldrich, U.S.A.) was added to the secondary fluid and stirred with a magnetic stirrer overnight. Then, 1.5 vol % of the dyed secondary fluid was added to the PMMA/glycerol binary suspension to form a capillary suspension network. A confocal microscopy (SP8 X, Leica Microsystems, Germany) was used with excitation wavelength of 552

nm and emission wavelength of 570 nm. The particles and the primary fluid remained undyed. The confocal result is shown in Fig. 2.4, where black circles with dark red outline indicate the PMMA particles and bright red circles indicate fluid droplets. The size ratio of the secondary fluid is comparable to the particles, as assumed in the simulation condition suggested in this study.

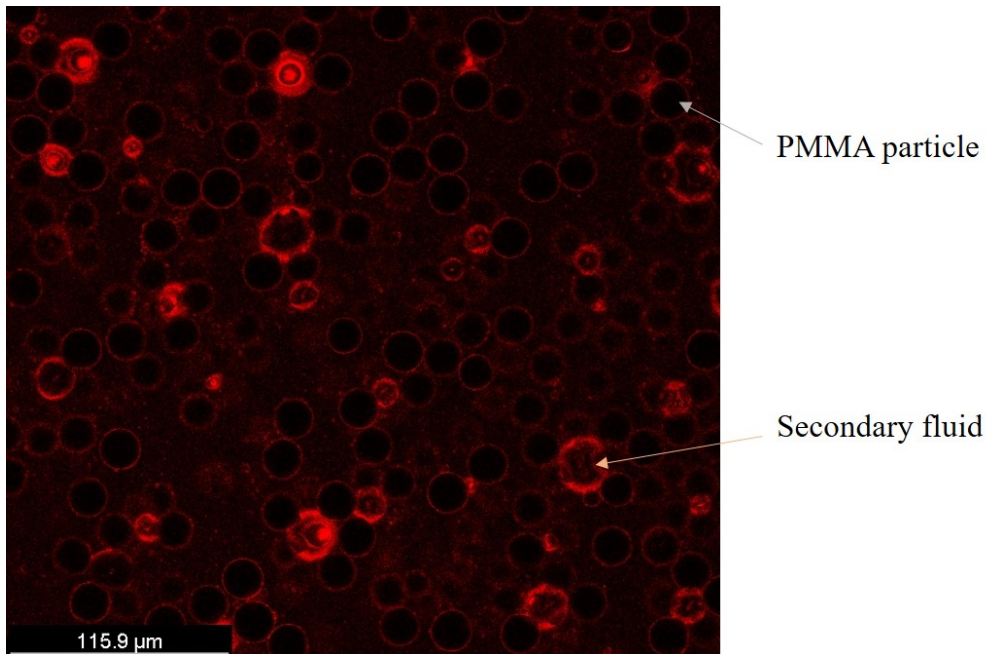


Figure 2.4 A 2D confocal microscopic image of capillary suspension with the secondary fluid marked with a fluorescent dye. The particles appear as the black circles with red outline, and the secondary fluids appear as the red circles. The system is composed of PMMA particles with  $20\ \mu\text{m}$  diameter, glycerol as primary fluid, and paraffin oil as secondary fluid, and the three-phase contact angle is approximately 90 degrees.

# Chapter 3

## Results

### 3.1 Effect of characteristic variables

In this section, the effect of simulation parameters on the behavior of the model suspension will be investigated. First, in section 3.1.1, the validation of the most important assumption in this simulation, the spherical droplet surface assumption, will be conducted and the simulation condition where the assumption is valid will be identified. Then, in section 3.1.2, the structural change and the rheological behavior according to the droplet-particle size ratio and the droplet volume fraction will be discussed. Finally, in 3.1.4, the effect of polydispersity on the droplet size will be discussed.

### 3.1.1 Effect of $\theta_c$

The contact angle,  $\theta_c$ , in eqn.(2.10) is defined by Young's equation,  $\cos \theta_c = (\Gamma_{S1} - \Gamma_{S2})/\Gamma_{12}$ . However, as the simulation in this study forces the shape of the free surface as a sphere, when a particle and a droplet reach an equilibrium after a contact, the contact angle is not guaranteed to be identical with  $\theta_c$ . As mentioned in section 2.5, the observed contact angle and  $\theta_c$  may be largely different when the  $\theta_c$  calculated from Young's equation is small. To determine the range of  $\theta_c$ , in which the observed contact angle is consistent with  $\theta_c$ , the observed contact angles are calculated at the minimum excess energy when the droplets of different size ratios interact with the particles. The excess energy is calculated from eqn.(2.7) as a function of the center-to-center distance between the particle and the droplet, and the distance, at which the excess energy exhibits its minimum, can be derived. At this distance, the observed contact angle is calculated. If the observed contact angle and  $\theta_c$  have little to no difference, it means that the spherical shape assumption is valid and vice versa. This is displayed in Fig. 3.1.

In Fig. 3.1, the range in which the error,  $\varepsilon_\theta$ , is not negligible is different for each size ratio, but the observed contact angles are accurate for  $\theta_c$  larger than 90 degrees for all the size ratios. Note that when the size ratio is 1, the error is small for some contact angles less than 90 degrees as well. However, because the spherical shape assumption is present, the droplet bridge between the particles does not form a pendular bridge and the contact angles less than 90 degrees are not suitable to be used regardless of the error value. In order to describe the pendular state capillary suspensions with concave interfacial shape, the spherical assumption needs to be modified, for example, a cylindrical assumption can be applied, or a completely different coarse-graining needs to

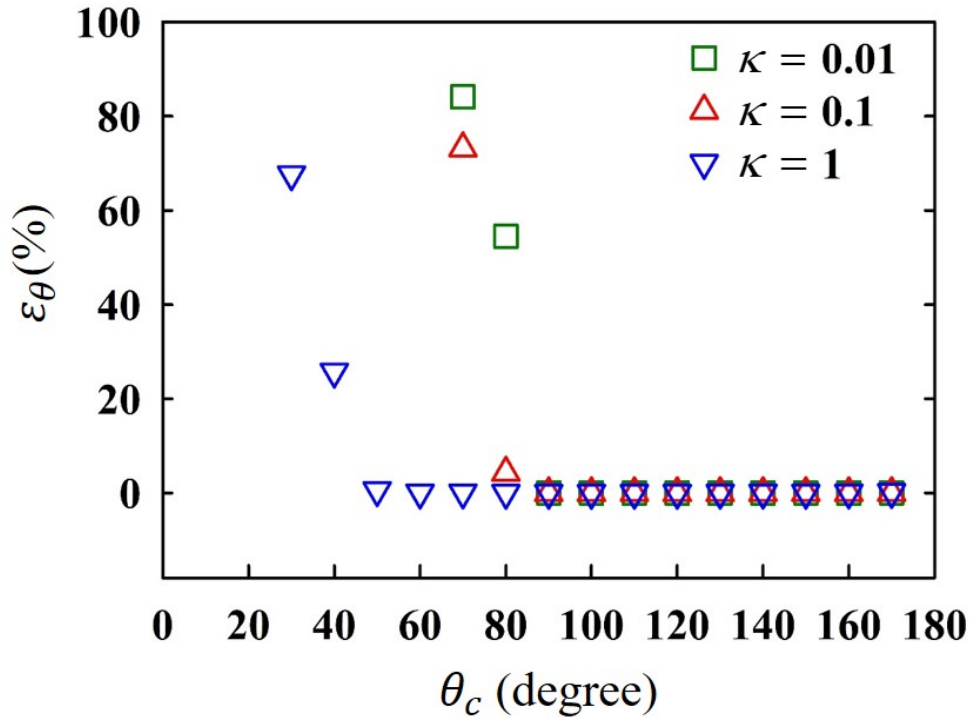


Figure 3.1 The error( $\varepsilon_\theta$ ) between the intended contact angle( $\theta_c$ ) and the observed contact angle is plotted as a function of the intended contact angle. Three size ratios were used: 0.01(green square), 0.1(red triangle), 1(blue inverted triangle). When the  $\theta_c$  is larger than 90 degrees, the error is almost zero for all the size ratios.

be adopted. The spherical assumption can describe the pendular state to some extent, as the blue upside-down triangle in Fig. 3.1 indicates, but the calculated surface area and energy will be very inaccurate due to the lack of concave interfacial shape.

In Fig. 3.2(a), it is illustrated how the values of  $\varepsilon_\theta$  deviate from 0 when the intended contact angle,  $\theta_c$  decreases. At a given  $\kappa$ , there is a minimum value of theta that can be achieved due to the hard core repulsion between the particles. At  $\kappa$  of 0.4,  $\theta_c$  of 71.2 is the minimum and the particles come into a contact, meaning that the droplet has no more room to increase its radius. If the  $\theta_c$  of lower than this value is given, the observed and intended contact angles inevitably deviate from each other. In Fig. 3.2(b), a demonstration of how the low values of  $\varepsilon_\theta$  are achieved when  $\kappa$  is large is shown. When  $\kappa$  is 0.4, the minimum  $\theta_c$  is 71.2 degrees as mentioned before, and any value below that will result in a high  $\varepsilon_\theta$ . If  $\kappa$  becomes larger, for example, 1, the minimum value of  $\theta_c$  is much lower and the value of  $\varepsilon_\theta$  is still 0. However, the demonstration shows that due to the spherical assumption of the droplets, the droplet shape remains convex and even though the  $\varepsilon_\theta$  value seems reasonable, it is clear that the droplet does not reflect what really happens, i.e. concave shape. Thus, we refrain from examining  $\theta_c$  below 90 degrees in this study, and in order to properly describe the pendular states, taking a different approach would be more reasonable.

After this paragraph, the  $\theta_c$  of 92 degrees is used to describe the capillary suspension in the capillary state. This contact angle is close to the experimentally measured value for a capillary suspension made of PMMA, glycerol(primary), and paraffin oil(secondary).

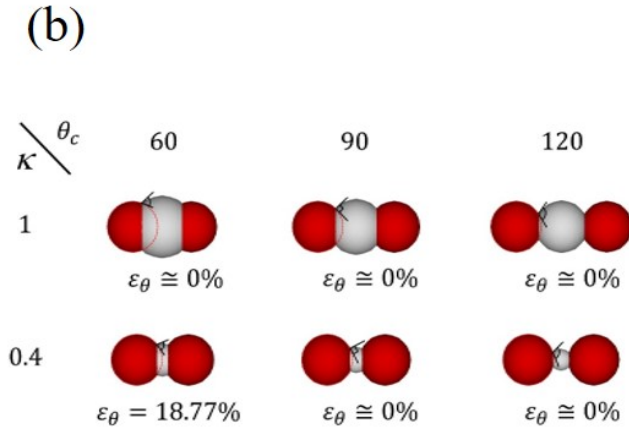
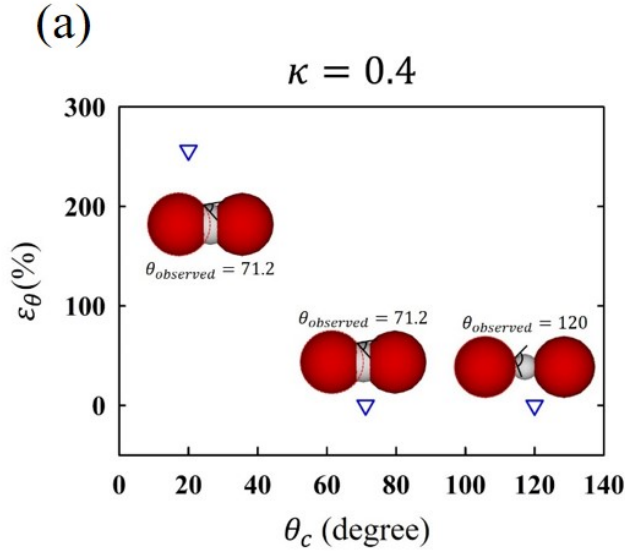


Figure 3.2 (a) A demonstration of how the observed contact angle deviates from the intended contact angle. (b) A demonstration of what happens when the contact angle goes below 90 degrees and still have low  $\varepsilon_{\theta}$ . Red spheres are the particles and the grey spheres are the droplets. The red dotted outline indicates the peripheral of the droplet screened by the droplet. The black solid lines indicate the measurement of the observed contact angle.

### 3.1.2 Effect of $\kappa$ and $\phi_f$

The rheological properties of the capillary suspension are developed by the bonding between the particles and fluids, thus the importance of the dimensionless parameters  $\phi_f$  and  $\kappa$  is clear as they determine the amount of the added droplet. In this section, we will investigate how the structure and the rheological properties evolve as these two variables change. The intuitive, or observable by experiment, fact is that if  $\phi_f$  is too low, the gel structure is not formed because there exist not enough capillary bonds to connect particles. Also, the same reasoning holds true for  $\kappa$  being too large. In experiments, a sufficient amount of mixing is critical for the formation of the capillary suspension, and having not enough amount of droplets to form the sample-spanning network would be equivalent to a situation where the secondary fluid droplets are not split enough due to an insufficient mixing. Also, through the previous investigations via microscopic approaches, the droplets are known to exhibit a size that is comparable to the particle sizes at the most in the capillary suspension. Thus, the range of  $\kappa$  compared in this study will be limited to less than 1.

The change in particle cluster size according to  $\kappa$  is shown in Fig. 3.3(a). In this simulation, the capillary force is the sole factor of the attractive interaction and therefore, as  $\kappa$  becomes smaller and the number of droplets increases, the cluster size becomes larger. As mentioned previously, when  $\kappa$  is 0.4, more than 9,900 particles out of total 10,000 particles belong to a single cluster and a sample-spanning network is achieved. When  $\kappa$  is 0.5, the number of particles in the largest cluster is approximately 9,700 but to keep the maximum cluster size to the highest value possible,  $\kappa$  equal to or less than 0.4 needs to be selected. For  $\kappa$  equals to 0.3, although more than 9,900 particles are in one cluster, Fig. 3.3(b) indicates that a droplet either links two particles only or just attaches to a

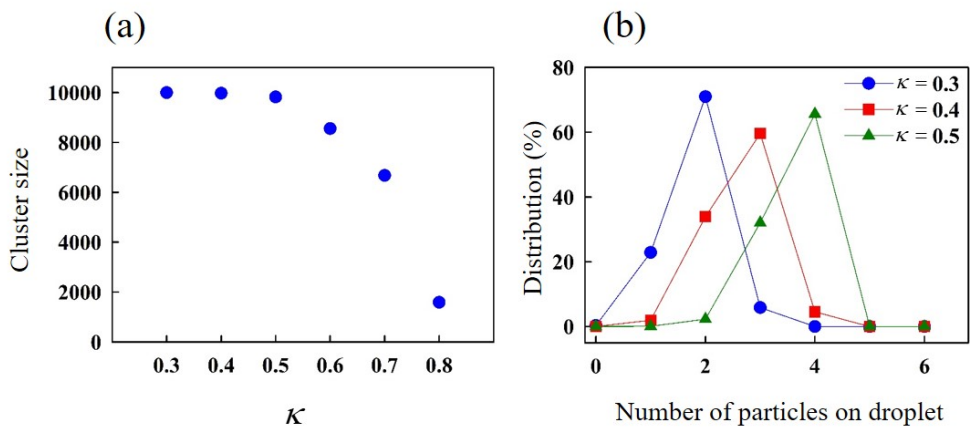


Figure 3.3 (a)Maximum cluster size change according to  $\kappa$ , and (b)the particle distribution on the droplet when  $\phi_p=25$  vol%,  $\phi_f=2$  vol%.

single particle, and hardly links three or more particles. By the observation from experiments, the capillary state is described to have multiple particles bonded together by a secondary fluid droplet. Thus, in the case of  $\kappa$  being 0.3, it barely describes the capillary state. Rather, when  $\kappa$  is 0.4, it describes the capillary state that forms a sample-spanning network very well. The number of particles on droplet can also be seen as in an agreement with the coordination number of packed spheres. For  $\kappa$  of 0.4, the available configurations are triangular and tetrahedral configurations, and the number of particles on droplet in Fig. 3.3(b) indicates that the majority of the droplets have 3 or 4 particles on them. In order to form an octahedral,  $\kappa$  needs to be higher than 0.4142. However, given that the current system is far from being a closely packed system and the octahedral configuration is therefore hardly observed.

To observe the structure difference between different values of  $\kappa$  more closely, the snapshots of different  $\kappa$  values are displayed in Fig. 3.4. When  $\kappa$  is 0.3, it can be observed that there are cases of multiple droplets existing in between two particles. Because there is no coalescence taken into account yet, such behavior leads to an unrealistic type of bonding where more than one droplet connect two particles. Ideally, especially in capillary state as assumed in this study, no more than one droplet should be involved in bonding of two or more particles, and such behavior starts to appear at higher  $\kappa$ . The snapshot also corresponds well to the bond number analysis that at this  $\kappa$ , the size of the droplets are not large enough to connect three or more particles at once. Thus, although the cluster size is the largest for  $\kappa$  being 0.3, the direct observation of the network indicates that  $\kappa$  of 0.3 does not properly describe the capillary network.

When  $\kappa$  is 0.4, there is little to none observation of droplets existing in the same particle pairs, yet, the number of particles that are not in the cluster (blue spheres) is increased than in  $\kappa = 0.3$  case. When  $\kappa$  is 0.5 or 0.6, the number of

particles that are not in the cluster is further increased, and therefore,  $\kappa$  of 0.4 is the optimal choice to attain the maximum cluster size while maintaining a realistic microstructure.

Fig. 3.5(a) describes the viscosity change according to the droplet concentration when  $\kappa$  is fixed at 0.4. The red circle and blue square indicate experiment and simulation results, respectively. To observe the effect of  $\phi_f$  better, both the experiment and simulation were designed to have similar conditions:  $\phi_p$  of 25 vol% and  $\theta_c$  of approximately 90 degrees. In the experiments, the reduced viscosity increases from 0 to 0.25 vol% of  $\phi_f$  and then varies a little after 0.25 vol% of  $\phi_f$ . In the simulation, the reduced viscosity gradually increases as  $\phi_f$  increases up to 1.5 vol%, after which it remains almost constant. At low  $\phi_f$ , the simulation results exhibit a slower increase in viscosity as  $\phi_f$  increases than the experiment results do. This difference may originate from the assumptions of this method, such as the absence of the hydrodynamic interaction, the uniform droplet size distribution, and the neglected droplet break-up and coalescence. At a fixed  $\kappa$ , although the number of droplets increases proportionally to  $\phi_f$ , it can be assumed that the reduced viscosity reaches a plateau because the excess droplets do not contribute to the increase of the viscosity once the required number of droplets form the network.

To understand this better, the bond number distribution at each condition is analyzed in Fig. 3.5(b). As  $\phi_f$  increases, the average number of droplets on a particle increases as well. When  $\phi_f$  is above 1.0 vol%, the change in reduced viscosity decreases despite the increase in  $\phi_f$ , and the excess droplets attach to the particles that already formed a network with 2 to 4 droplets, causing a rapid increase in the number of droplets on a particle. Especially, when 4 or 5 droplets are on a particle, the increase in the number of droplets on a particle is small or trivial below 1.0 vol% of  $\phi_f$ , followed by a rapid increase above 1.0

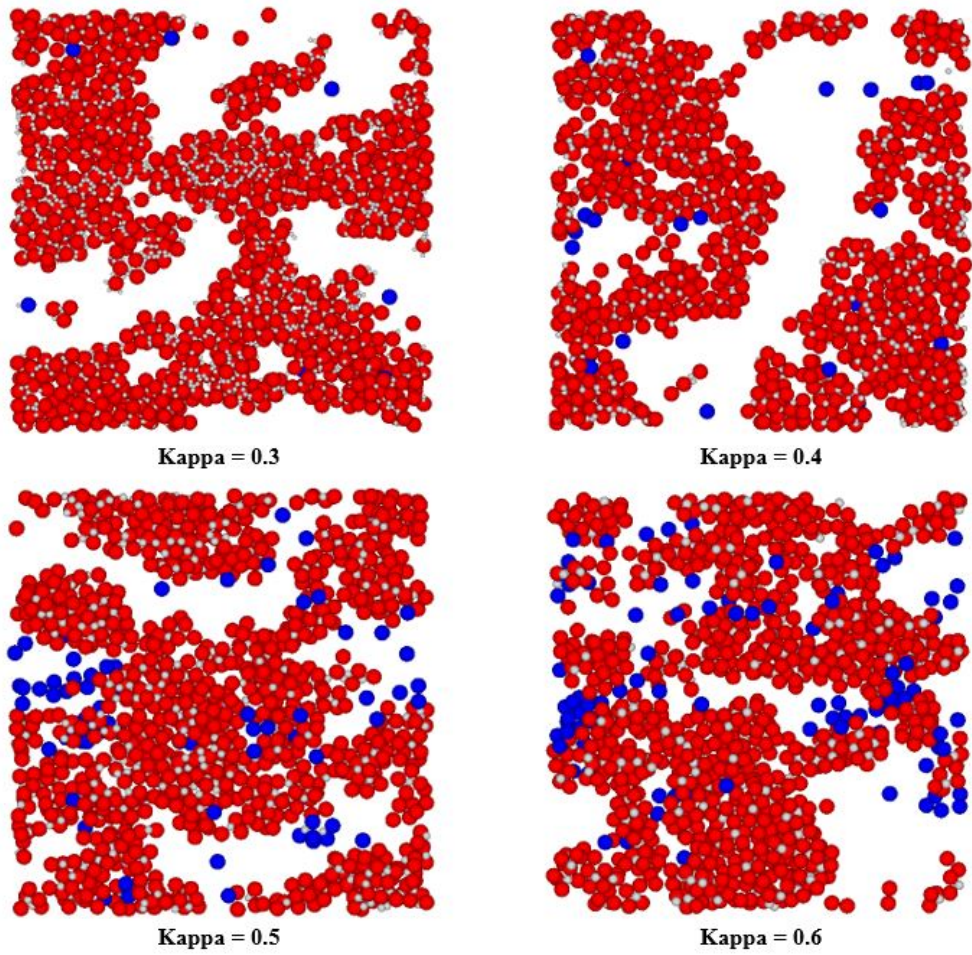


Figure 3.4 The depth-cut snapshots for different  $\kappa$  values. Red and blue spheres indicate the particles that are in and out of the cluster, respectively, and the grey spheres indicate the droplets.

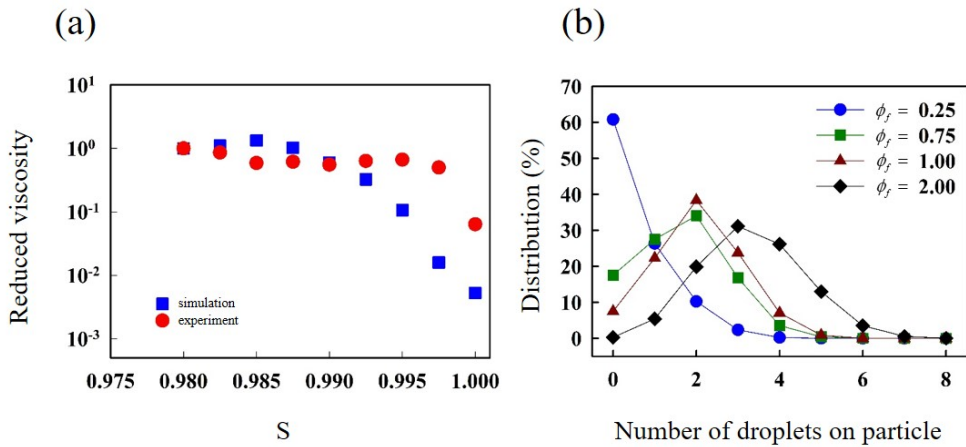


Figure 3.5 (a) The viscosity change according to  $S = 1 - \phi_f$  and (b) the droplet distribution on the particle in the range of  $\phi_f = 0.25 - 2$ . The red circles in (a) indicate experimental results measured with a capillary suspension that is made of  $20 \mu\text{m}$  PMMA, glycerol as primary fluid, and paraffin oil as secondary fluid at  $\phi_p = 25 \text{ vol}\%$ . The normalization of viscosity was based on the viscosity at  $S = 0.980$ .

vol% of  $\phi_f$ . This implies that once the sample-spanning network is formed, the particles that are already in contact with several droplets are not affected as much by the additional contacts of droplets, and therefore, the reduced viscosity does not show an additional increase.

In addition, a question that naturally arises from the difference between the experiment and the simulation in Fig. 3.5(a) is how  $\phi_f$  and  $\kappa$  are related. In the real-world, the distribution of the droplet size depends on the concentration of the secondary fluid and the degree of mixing. In this simulation, the rheological property of the suspension depends on  $\phi_f$  and  $\kappa$  simultaneously, and the situation where only one of them varies is inconsistent with what really happens. In order to take more accurate approach on how  $\phi_f$  and  $\kappa$  are related, we need to either take coalescence and break-up into account or find a physically reasonable way to relate the two, which are yet to be done. Thus, the initial formation stages of the capillary suspension as the secondary fluid is added are yet to be explored.

At a fixed value of  $\phi_f$ , the value of  $\kappa$  was varied and compared with the experimental value in Fig. 3.6. Under this circumstance, more discussion can be made on what is the reasonable relationship between the two variables, and how close will the simulation fit to the experimental data observed in the study of Koos et. al. [1] The discussion on this matter needs to be conducted as a subsequent study. Unless otherwise mentioned,  $\kappa=0.4$ ,  $\phi_f=2$  vol% will be used to achieve sufficient network formation.

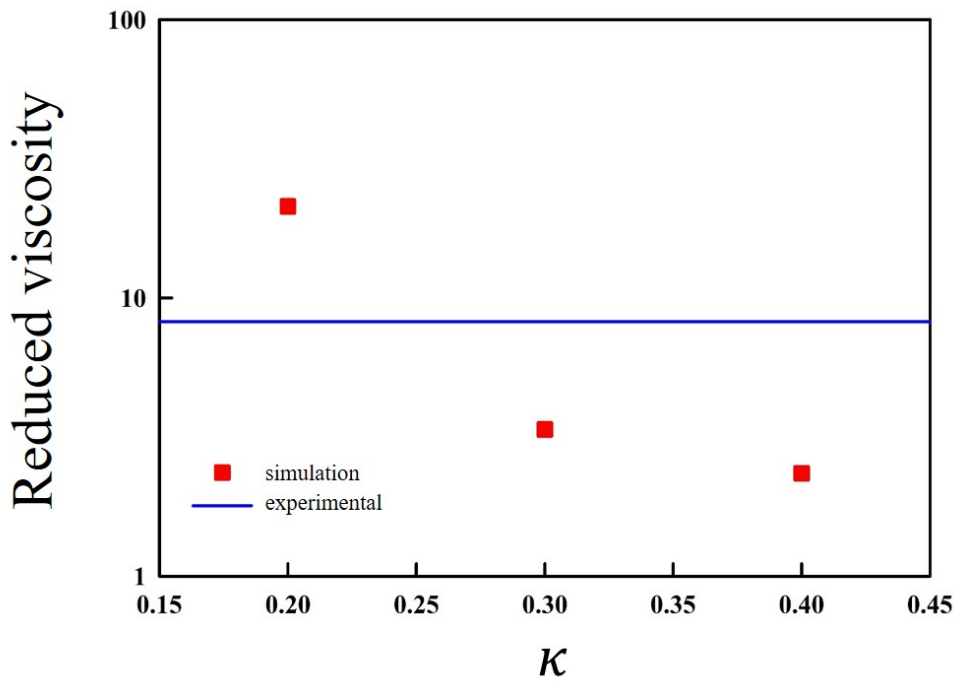


Figure 3.6 The reduced viscosity versus kappa at a fixed  $\phi_f$  of 2 vol %. Red squares indicate the simulation values with varying values of kappa and the blue solid line indicates the value attained from the experiment.

### 3.1.3 Effect of $\phi_p$

The effect of  $\phi_f$  is shown in the previous subsection and it was found that the amount of secondary fluid is important to induce a sample-spanning network given that there is a sufficient amount of particles present. Here, we will also examine how the solid volume fraction will affect the system when there is a sufficient amount of droplets present, which was fixed at 2 vol%. The number of particles used in the system was altered and therefore, the total number of particles and droplets present in the system differs, and to compare how much of particles and droplets contribute to the largest cluster size, the cluster size was divided by the total number of particles and droplets. Then, the number of particles on droplet and the number of droplets on particle were compared for each solid volume fraction.  $\kappa$  was fixed at 0.4.

In Fig. 3.7(a), the reduced cluster size is plotted for each solid volume fraction. When  $\phi_p$  is 0.25, more than 99 percent of the particles are involved in the largest cluster as demonstrated in Fig. 3.3.  $\phi_p$  of 0.2 has a slightly lower reduced cluster size of 0.94, which is still high enough to form a sample-spanning network. However, the number of particles and droplets involved in the largest cluster dramatically decreases for  $\phi_p$  of 0.15 and 0.1, reaching 0.82 and 0.65, respectively. The reason for such a dramatic cluster size drop can be found by examining Fig. 3.7(b) and (c). In Fig. 3.7(b), the number of droplets on particle is demonstrated. The number of droplets on particle peaks at 3 for  $\phi_p$  of 0.25, but the rest peaks at 4, indicating that the excess amount of droplets due to the decrease in the number of particles find the particles and try to attach to them. However, the particle surface available is limited and therefore, the graphs of  $\phi_p = 0.1, 0.15,$  and  $0.2$  show similar shapes. The shape changes slightly as the solid volume fraction decreases and the changes are in the direction of maximizing

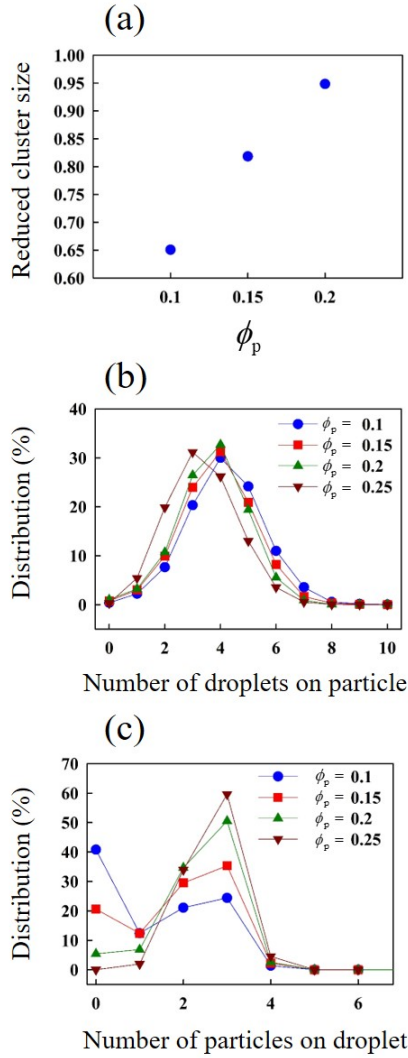


Figure 3.7 (a)the reduced cluster size, which is cluster size divided by the total number of particles and droplets present in the system. (b)the number of droplets on particle and (c)the number of particles on droplet for different solid volume fractions of 0.1, 0.15, 0.2, and 0.25, each represented by symbols of blue circle, red square, green triangle, and brown upside-down triangles, respectively.

the number of droplets on particle due to the larger number of free droplets. In Fig. 3.7(c), it is clearly shown that the number of droplets with no particle attached increases dramatically as the solid volume fraction decreases, also indicating that the presence of excess droplets that do not contribute to the network. Also, the number of droplets attached to 1 particle increases, which indicates that these droplets do not contribute to the network as well. This results in a lack of the sample-spanning network that was observed in  $\phi_p = 0.25$ , and therefore, in order to achieve a model capillary suspension with a sample-spanning network,  $\phi_p$  of 0.25 was chosen.

### 3.1.4 Effect of polydispersity in $\kappa$

In the real-world, the fluid droplets rather form different-sized droplets than uniform size droplets. The droplet distribution is controlled as described in section 2.5. The effect of polydisperse droplets is examined in this subsection.

In Fig. 3.8, the rate sweep data is shown for the systems with and without the polydisperse droplets. When the droplets are uniform, the stress curve shows a rapid increase at low shear rates below  $10^0$  followed by a less steep and linear increase at higher shear rates. The same trend is present when the droplets are polydisperse, and the shear stress at the shear rate of  $10^{-1}$  is slightly higher than that of the uniform droplet case. However, at this shear rate, the error is high and the reason for such high error is due to the local freezing, which will be explained in the later part of this study. In overall, it can be concluded that the polydisperse droplets do not bring about a significant difference in terms of the stress behavior in the rate sweep data.

Next thing that needs to be examined is how the low shear viscosity is affected by the polydispersity. Taking account of the polydispersity as defined in section 2.5, the overall number of droplets is reduced by 15 to 20 percent on average, due to the presence of smaller droplets. Thus, it can be expected to have different viscosity behaviors with respect to the secondary fluid volume fraction. In the model system used in this study, the polydispersity of the secondary fluid droplets is kept as monodisperse droplets to keep the variables and their effects on the result as low as possible. However, many different modes of polydispersity, such as bimodal and normal distribution, need to be tested to explore how the polydispersity of the droplets plays a role in the network formation. Also, it would be helpful to examine how the polydispersity looks like in experiments via fluorescent confocal imaging. Lastly, the consideration

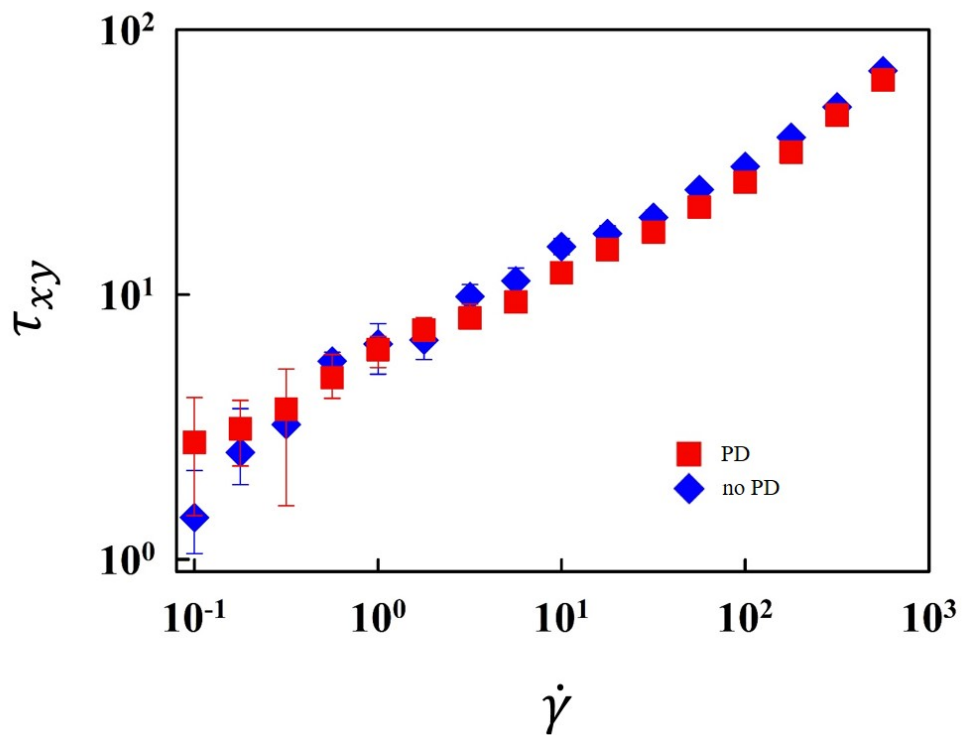


Figure 3.8 The stress versus shear rate curve of the system with  $\phi_p=25$  vol%,  $\phi_f=2$  vol%, and  $\kappa=0.4$ . Red squares and blue diamonds represent the systems with and without the polydisperse droplets, and the solid lines represent error bars.

of the polydispersity is important when there is no coalescence or break-up of droplets, and once the coalescence and break-up are implemented, the concerns regarding the polydispersity of the droplets would be significantly reduced.

In Fig. 3.9, both the polydisperse and uniform droplet cases exhibit initial increases as the volume fraction of the secondary fluid increases followed by a plateau. The plateau is expected to be present because when a sufficient amount of droplets are present, the network is saturated and the additional droplets hardly affect the viscosity after the saturation point. However, as mentioned earlier, the polydisperse droplet case has less number of droplets compared to the uniform droplet case at a given secondary fluid volume fraction and this results in lower viscosity at  $S=99$  to  $S=99.5$ . Then, the plateau exists at the same level of viscosity, meaning that at  $S=98$ , which is mainly used in this study for flow property analysis, the effect of polydispersity is negligible. Thus, in this study, in order to remove the additional parameter, the droplet polydispersity was not further considered and the uniformly sized droplets are used.

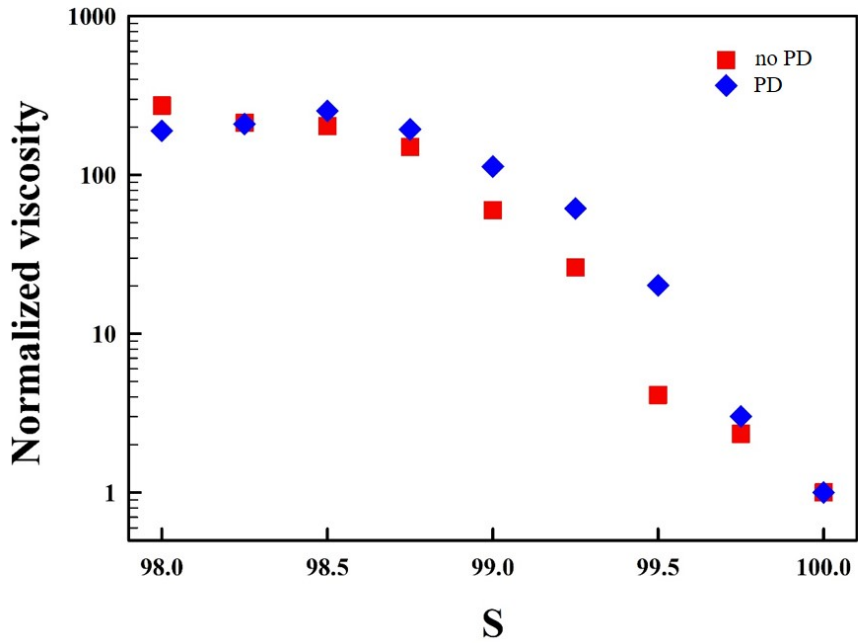


Figure 3.9 The low shear viscosity versus secondary fluid volume fraction plot of the system with  $\phi_p=25$  vol%,  $\phi_f=2$  vol%, and  $\kappa=0.4$ . Red squares and blue diamonds represent the systems with and without the polydisperse droplets, respectively.

## 3.2 Structure evaluation

### 3.2.1 Effect of mixing protocol

In this simulation, the lack of random thermal motion makes the initial mixing protocol important. As discussed in section 2.5, there were three mixing protocols that were subjected for comparison in this study. Different mixing protocols result in different levels of residual stress after the resting step, where the mixing protocol involving the shear flows produces the most residual stress and random motion mixing produces the least. Majority of the residual stress comes from the capillary forces, and it is inevitable to have some level of residual stress due to the sample-spanning network and the lack of the thermal motion that would otherwise lead the particles and droplets to find the optimal position to minimize the residual stress. When the mixing protocol mainly involves shear mixing, the microstructure formed during the mixing naturally has the effect of directional displacement, leading to layer-like structures along the direction of the flow. When the main mixing is done with random motion followed by the low shear mixing to induce the freezing, the directional effect of the shear flow is minimized, but still has higher residual stress than exclusively random motion based mixing protocol.

In a simple shear test, the different types of mixing protocol had little impact as the system is exposed to a continuous and steady shear regardless of the initial structure. However, when it comes down to the oscillatory shear tests, the residual stress becomes more important as the level of the residual stress may be as much as the maximum amplitude of the measured stress. Fig. 3.10 shows the residual stress levels of each mixing protocol after applying sufficient resting time. It is concluded that the residual stress level is minimum when there is no shear flow involved in the mixing protocol, yet, without the low

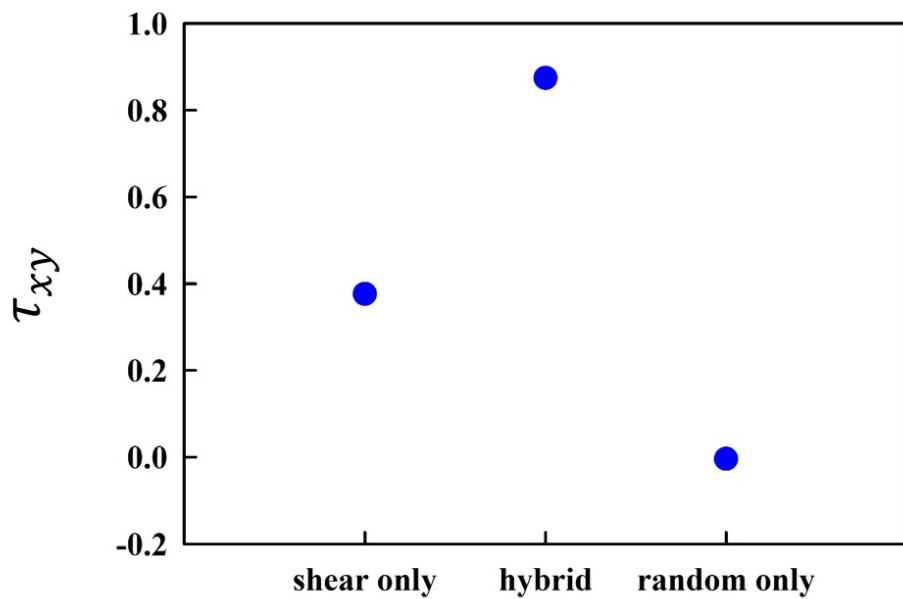


Figure 3.10 The residual stress after resting for different mixing protocols. Shear only, hybrid, and random only in x-axis indicates shear only mixing, random motion and shear hybrid mixing, and random motion only mixing, respectively.

shear flow applied before resting, it is much less likely to observe the frozen regions of the microstructure.

To investigate where such difference comes from, the two different mixing protocols, hybrid and random motion only, are compared in Fig. 3.11. The figure is the depth-cut images of two distinct mixing protocols, where the red and blue spheres indicate the particles and grey spheres indicate the droplets. The white space, or the background, is the primary fluid. The similar configuration for the shear only mixing protocol is presented in Fig. 3.4 for  $\kappa = 0.4$  case. Fig. 3.11(a) depicts the hybrid mixing protocol, where the initial mixing was done via the random motion and then a weak shear was applied to induce the local freezing. Fig. 3.11 demonstrates the configuration formed purely from the random motion. The hybrid case shows that the particles and droplets are connected in a more compact manner compared to the random motion only case, and the microstructure seems more closed. On the other hand, in the random motion only case, the network seems less dense and the microstructure exhibits a more open structure and is better distributed across the space. While both cases have the sample-spanning networks, the mixing protocols affect the microstructure and whether the network will be affected by the local freezing.

Thus, it is important to decide which mixing protocol should be used depending on what sort of microstructure one would like to investigate before carrying onto the oscillatory shear tests. Also, considering that the simulation is ballistic, 8 to 16 initial configurations were subjected to the same mixing and flow conditions and the average of the results was used for further analysis.

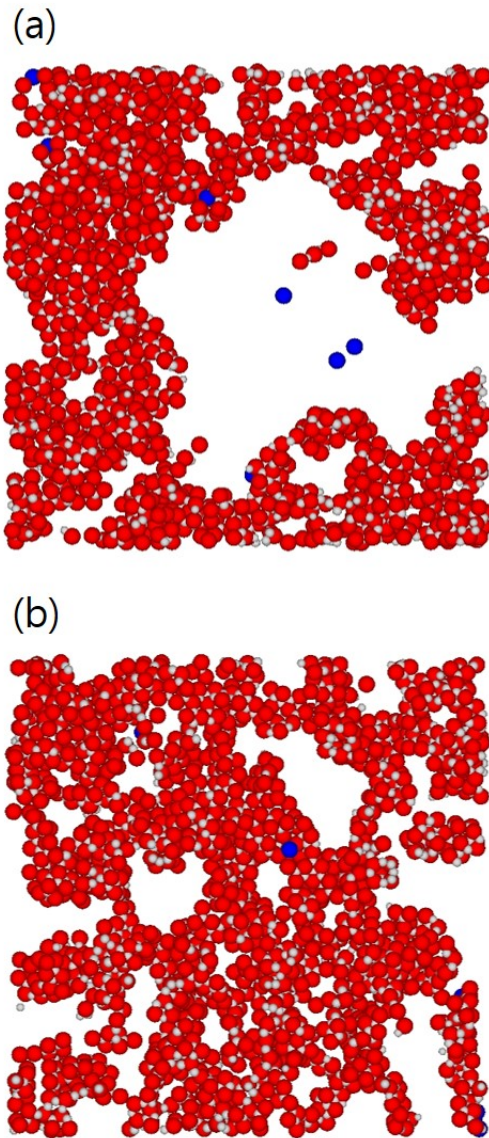


Figure 3.11 The depth-cut snapshots for different mixing protocols. Red and blue spheres indicate the particles that are in and out of the cluster, respectively, and the grey spheres indicate the droplets. (a) hybrid and (b) random motion only mixing protocols are depicted.  $\phi_p=25$  vol%,  $\phi_f=2$  vol%, and  $\kappa=0.4$

### 3.2.2 Sample-spanning network

In capillary suspension, one of the most important characteristics in structure is the sample-spanning network. Throughout the system, the particles are connected to each other by the secondary fluid, and the presence of the sample-spanning network is what gives the unique rheological properties that capillary suspensions exhibit, such as a yielding behavior. In this study, the presence of the sample-spanning network is determined in two steps. The first and simple step is to determine how many portions of the particles are involved in the main cluster. The cluster size is determined by assigning numbers to each particle and overwriting the cluster number when it comes to a contact with other clusters. When there is a sufficient amount of droplets that induce the clustering, most of the particles are found to be in the same cluster, meaning that the system is sample-spanning in the observed window. However, this step only determines whether the network is sample-spanning within the periodic boundary, and because the observation window contains a maximum of 10,000 particles, we cannot determine with certainty if the network is genuinely sample-spanning outside the observation window.

In order to determine if the sample-spanning network is present beyond the periodic boundary, we need to test if copying and pasting the coordinates side-by-side results in the sample-spanning network. Thus, 7 copies of the particle and droplet coordinates were made and pasted in x, y, and z direction. That is, when the original structure is at  $(0,0,0)$  of  $(x,y,z)$  coordinate, the box length is added to each direction and pasted. As a result, we have 8 identical copies of the coordinates at  $(0,0,0)$ ,  $(bl,0,0)$ ,  $(0,bl,0)$ ,  $(0,0,bl)$ ,  $(bl,bl,0)$ ,  $(bl,0,bl)$ ,  $(0,bl,bl)$  and  $(bl,bl,bl)$  where  $bl$  is the box length, as described in Fig. 3.12. After the coordinates are copied and put beside each other, the capillary network calcu-

lation is done to check for the connectivity. If the cluster size is 8 times larger than before, it means that the network is sample-spanning beyond the periodic boundary.

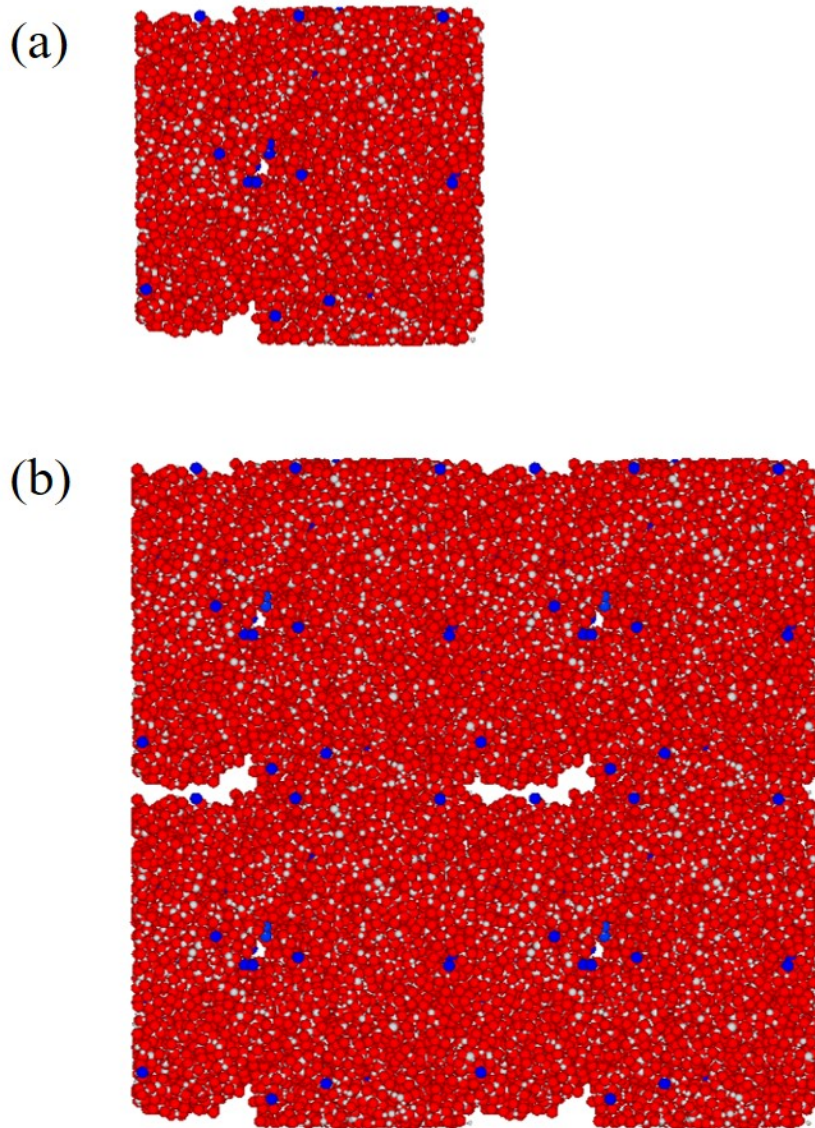


Figure 3.12 (a)The original particle cluster (b)the particle cluster that has been extended to x, y, and z direction to check for the sample-spanning network across the periodic boundary. Red and blue spheres indicate the particles that are in a cluster and out of the cluster, respectively. Grey spheres indicate the droplets.

### 3.3 Flow properties of model capillary suspension

In this section, the shear stress, structure, and flow characteristics of the sample-spanning network at  $\kappa=0.4$ ,  $\phi_f=2$  vol% under shear flow will be evaluated.

#### 3.3.1 Flow curve

To the gel achieved in Fig. 3.5(a), the shear flow with shear rates ranging from  $10^{-1}$  to  $10^3$  is applied and the stress is measured using eqn. (2.26). The measured viscosity and shear stress is plotted in Fig. 3.13(a) and Fig. 3.13(b). In Fig. 3.13(a), the cluster size according to the change in the shear rate is plotted as well.

In Fig. 3.13(a), the viscosity of the gel system shows a strong shear thinning behavior with a slope of -0.7 throughout most of the shear rate. However, the cluster size remained constant without a dramatic change, which indicates that the capillary bonds between the particles are continuously breaking and forming during the shear. Note that the constant cluster size throughout the wide range of the shear rate does not necessarily correspond to the consistency of the microstructure, and the microstructures do change according to the shear rates. Under the effect of flows, there rise locally densified chunks connected to neighboring chunks through a thin bond. Because the cluster size is determined based on whether the particles are linked with others somehow, the local coarseness of the network or the structural heterogeneity is not reflected in the cluster size. However, when the shear rate is high enough, the network structure starts to break into the smaller flocs and the cluster size decreases. In Fig. 3.13(b), the shear rate increases over the entire shear rate regime. In a previous experiment, it was also reported that there exists a non-zero slope of the shear stress at very low shear rates for a system exhibiting a yield stress. [70] The

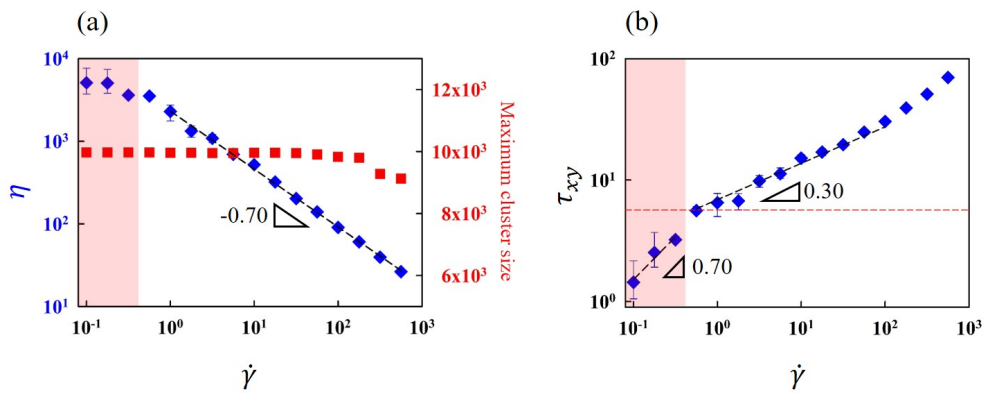


Figure 3.13 A graph of (a) viscosity ( $\eta = \tau_{xy}/\dot{\gamma}$ ) and maximum cluster size, and (b) stress versus shear rate. The blue diamond and the red square in (a) indicate the viscosity and the maximum cluster size, respectively. The dotted red line in (b) indicates the projected value of the yield stress, which will be discussed later.  $\phi_p=25$  vol%,  $\phi_f=2$  vol%,  $\kappa=0.4$ ,  $\theta_c=92$ .

study suggested that the stress may be a subject to a change at the shear rates below the yield stress due to slight disturbances inside the gel microstructure. To investigate what causes such behavior in this simulation, a local velocity analysis is conducted. The local velocity analysis that will be discussed later in section 3.3.2 indicates that the low shear rate regime, marked by the red area in Fig. 3.13, has a considerably different flow behavior from the high shear rate regime, (Fig. 3.14) and the slope change from 0.70 to 0.3 is also observed in Fig. 3.13(b). In the following section, the flow behavior in the low shear rate regime will be investigated in detail and the local freezing of the particle cluster and the yield stress (the dotted red line in Fig. 3.13(b)), in which the local freezing takes place, will be analyzed.

### 3.3.2 Yielding

To explore why the plateau at low shear rates, which is common in the yielding material, is not apparent, the local particle velocity and the local particle stress defined in section 2.5 are analyzed in both low and high shear rate regimes. In the high shear rate regime, ( $\dot{\gamma} \geq 0.56$ ) the local velocity is in good agreement with the imposed velocity profile of  $v_x(y) = \dot{\gamma}y$ . On the other hand, in the low shear rate regime, ( $\dot{\gamma} < 0.56$ ) freezing is observed in some regions. These are displayed in Fig. 3.14.

Fig. 3.14 displays the imposed velocity and the particle velocity for shear rates (a)0.1 and (b)5.6. The presented image is a snapshot of only one time period, and over the entire time span, the velocity keeps fluctuating a little. Thus, the seemingly negative slope of the right side of the particle velocity in Fig. 3.14(a) is merely due to a fluctuation. The particle velocity and the imposed velocity does not overlap in Fig. 3.14(a) while they do in Fig. 3.14(b). In this simulation, the movement of the particle is governed by the inter-particle inter-

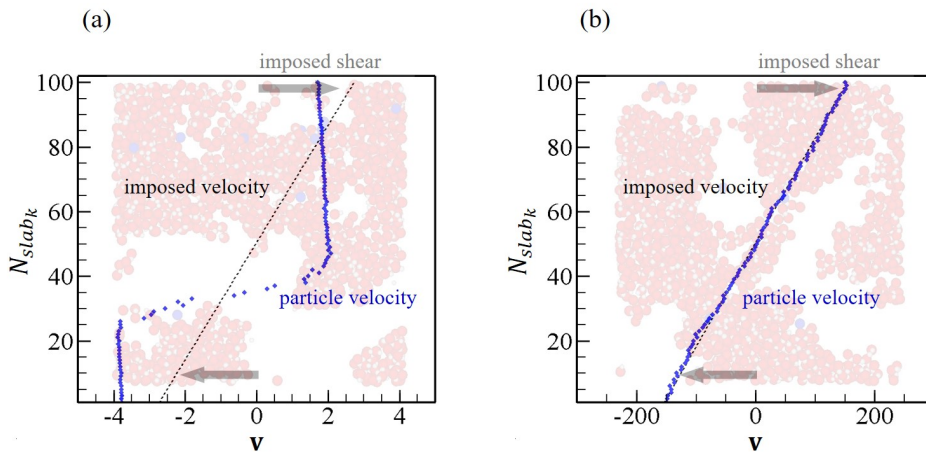


Figure 3.14 The graph that shows the particle average velocity at each bin when the  $y$  domain is divided into 100 bins. The shear rates for (a) and (b) are 0.1 and 5.6, respectively. The graphs are the snapshots at strain 10. The dotted black line, blue diamond, and grey arrow indicate the imposed velocity, the particle velocity, and the imposed shear direction, respectively. On the background overlay image, red and blue spheres indicate the particles that are in the cluster and the particles that are not in the cluster, respectively.

action and friction force caused by the background fluid velocity as defined in eqn. (2.21,2.22). At low shear rates, the suspension should not flow because the gel network is firm enough to withstand the hydrodynamic friction force. However, the Lees-Edwards boundary condition causes the gel structure to be torn by force. For example, when considering the interaction between two particles each located at the top and bottom of the simulation domain, the two experience forced relative movement due to the Lees-Edwards boundary condition even when they are jammed in the domain. It can be assumed that the cause of such a phenomenon is that the strain used in the Lees-Edwards boundary condition is based on the imposed shear rate, not on the actual movement of the particles. As a result of the forced relative movement of the top and bottom, the average shear rate throughout the entire simulation domain becomes the same as the imposed shear rate. That is, an artificial flow occurs due to the boundary condition even when there should be no flow. In spite of the forced flow, the particles freeze in place and retain their structure in most of the domain, and the shear rate range, in which local freezing occurs, is depicted as a red area in Fig. 3.13(a) and 3.13(b).

Likewise, the stress curve in Fig. 3.13(b) cannot properly represent the rheological property of the suspension at low shear rates ( $\dot{\gamma}=0.1$  to  $0.56$ ) where there exists a partial artificial flow. Also, the non-zero shear stress slope at low shear rates seems to be caused by the local freezing, which is not in an agreement with the suggested origin of the non-zero slope from the previous study.[70] In order to analyze this thoroughly, the local stresses instead of the average stress were measured and their changes were observed with respect to the local shear rate and the local strain.

As mentioned in section 2.5, the third order Savitzky-Golay filter with thirteen spatial points was applied to the local particle velocity profile,  $v_x^p(y, t)$ ,

measured by eqn. (2.27) to achieve a smooth velocity field. By differentiating the smooth velocity profile with respect to space, and by integrating it with respect to time, the local strain was obtained. Then, the position of the particles that moved less than 1% (strain  $\leq 0.1$ ) of the imposed strain of 10 could be separated and the local bins that exhibit such a trivial position change are labeled as frozen regions.

Fig. 3.15(a) shows the average of the measured local strain in the frozen regions with respect to the imposed strain at low shear rate ( $\dot{\gamma}=0.1$ ). In this condition, the local strain does not exceed 0.07 even though the imposed strain of 10 is applied. The local strain fluctuates because of the forced flow and the resulting rupture happens periodically in certain regions due to the Lees-Edwards boundary condition. Fig. 3.15(b) describes the local stress with respect to the local strain at low shear rate condition where the local freezing takes place. As the local strain fluctuates as in Fig. 3.15(a), the local stress fluctuates in a similar manner with a strong positive relation to the local strain in Fig. 3.15(b). Such a strong positive relation between the stress and the strain implies that the gel does not deform under the shear and retains its structure, which indicates the solid-like or the elastic deformation behavior. Thus, it can be inferred that the yield stress is present in the freezing regime. A similar shaped local strain graph can be achieved for higher shear rates ( $\dot{\gamma}=0.18$  and  $0.32$ ) upon isolating the frozen zones. Note that the number of frozen zones decreases as the shear rate increases. At  $\dot{\gamma}=0.32$ , the local strain begins to lose its elastic behavior and this will be described later in this section.

Fig. 3.16(a) shows the local strain throughout the entire regime where freezing does not appear at high shear rate ( $\dot{\gamma}=5.6$ ) and the local strain does not show any difference from the imposed strain. Likewise, at high shear rate condition where the freezing is not observed, the local velocity overlaps the imposed ve-

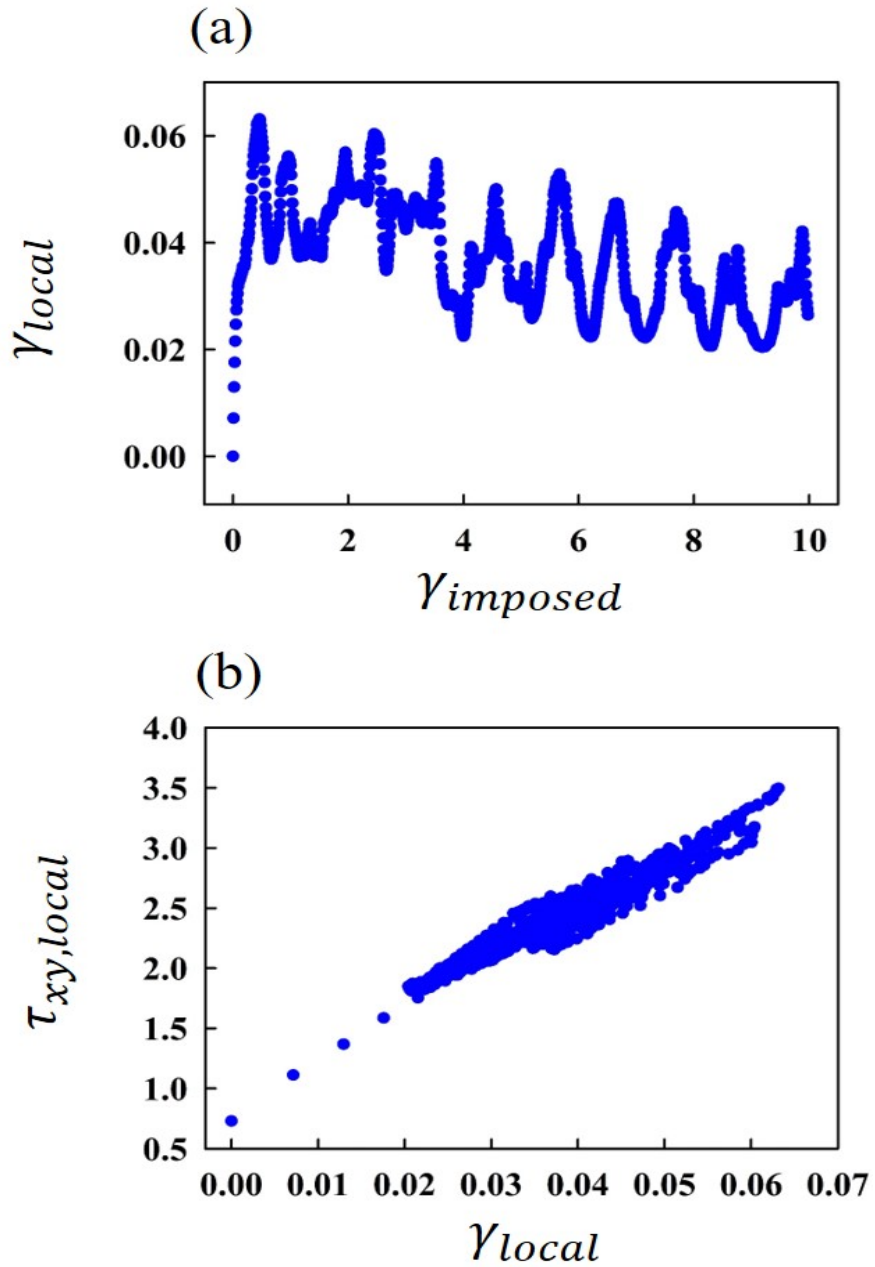


Figure 3.15 (a) The local strain versus imposed strain below 1% local strain, and (b) the local stress versus local strain when the shear rate is 0.1.

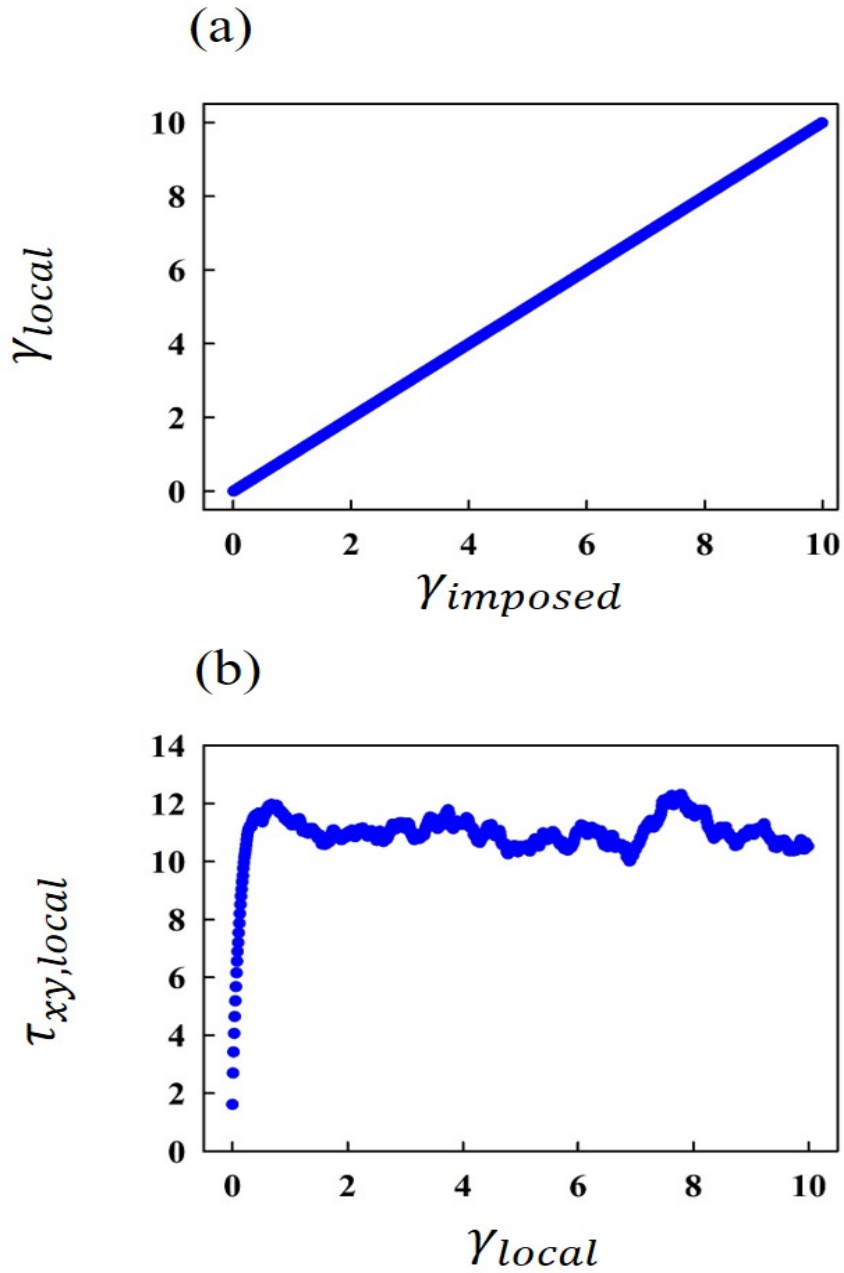


Figure 3.16 (a)The local strain versus imposed strain and (b)the local stress versus local strain when the shear rate is 5.6.

locity over the entire domain as shown in Fig. 3.14(b). Thus, the local strain in Fig. 3.16(a) is the same as the imposed velocity. When this happens, the local stress in Fig. 3.16(b) increases at the beginning followed by a plateau, just like what one can expect with a viscoelastic fluid. At low strain less than 0.1, the local stress does show a linear increase showing that at the initial stage of the shear flow, there exists an elastic behavior. At around local stress of 11, the sample-spanning network starts to yield to the shear flow, represented by the formation of the plateau, which indicates viscous behavior. Then, the elastic behavior is no longer seen and the local fluctuation of the stress due to the structure rearrangement under flow is observed. Later in this section, the slope of this linearly increasing stress will be compared to others that exhibit frozen zones.

At low shear rates, the particles in the frozen regions repeatedly go through an elastic deformation then recover by the rupture in certain parts, and the maximum value of local(elastic) stress that arises from the fluctuation is defined as the yield stress. Among the shear rates in Fig. 3.13(a), the stress in the frozen regions are plotted in Fig. 3.17. When the shear rate is 0.18, as is when the shear rate is 0.10, the local stress increases linearly with the local strain. When the shear rate is 0.32, the local stress increases linearly with the local strain until it reaches a plateau eventually, and the maximum local stress was measured as 5.4. This value is similar to the maximum local stress of 5.7 when the shear rate is 0.18, and this leads to a conclusion as follows. When the shear rate is 0.10, there is not enough stress to break the frozen structure, and when the shear rate is 0.18, the stress becomes close to the yield stress. When a larger shear rate of 0.32 is applied, the stress does reach the yield stress, which then leads to the yielding behavior between the local strain of 0.10 and 0.12. Additionally, when the shear rate is 5.6 and there is no frozen region, the stress increases

with a slope similar to the samples with the frozen regions at the startup of the shear, and increases further beyond the yield stress. It is worth noting that the starting points of each curve do not overlap even though they all have the same initial configurations because the values used are not from the entire sample, but from only the frozen regions.

According to Natalia et al., [71], the yield stress was between 3 Pa before an additional mixing and 10 Pa after an additional mixing for a capillary suspension composed of 25 vol% 20um PMMA as the particle, 2.5 vol% paraffin oil as the secondary fluid, and glycerol as the primary fluid. These values, if non-dimensionalized as was done in this study, are approximately 1 and 3, respectively. The yield stress implied in this stimulation is 5, which is the maximum value of the elastic behavior.

The yield stress measured in the simulation is not entirely accurate because of the distorted flow field by the Lees-Edwards boundary condition, the inhomogeneous distribution of particles in each  $y$  bin, and the lack of the hydrodynamic interaction, however, the significance lies in that the yield stress is still close to the ones measured experimentally.

The yield stress achieved above is plotted as a red dotted line in Fig. 3.13(b). When the stress is lower than the yield stress, in other words, in a low shear rate regime, the imposed shear rate does not properly reflect the shear rate that the particles experience due to the freezing. On the other hand, when the stress is larger than the yield stress, the imposed shear rate properly represents the shear rate that the particles experience. Thus, in the regime colored in red in Fig. 3.13(a) and (b), the local freezing as shown in Fig. 3.14(a) is present and the imposed strain and the local strain are not in accordance, which is a direct indication of the yield stress behavior.

In this study, the key assumption used to introduce the coarse-grained po-

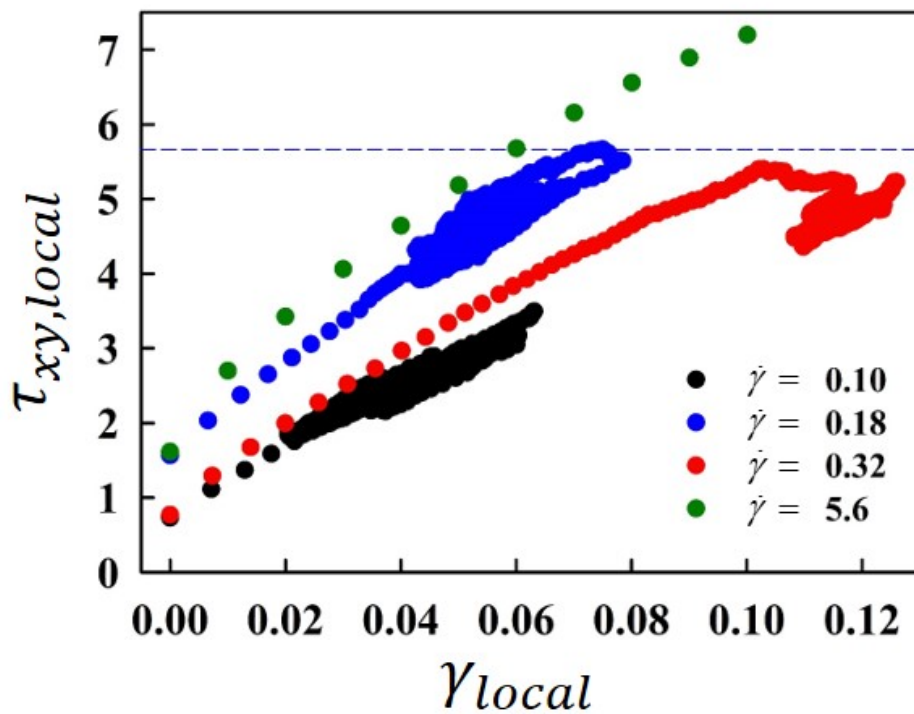


Figure 3.17 The stress versus the strain at different shear rates. Black, blue, and red indicate the shear rates of 0.1, 0.18, and 0.32, respectively, and these shear rates belong to the freezing condition. Green indicates the shear rate of 5.6 where the freezing is not observed.

tential was to fix the droplet shape as a sphere and this assumption was validated in section 3.1.1. To introduce the friction of the droplet on the particle surface, a surface bond was adopted and the torque on the particle due to the bonding point was also applied accordingly. The droplet-to-particle size ratio,  $\kappa$ , was assumed to be monodisperse to minimize the degree of freedom in the simulation. However, in the real world, the droplets will exhibit different sizes. Lastly, the Lees-Edwards boundary condition was used to attain a continuous flow field. Although the Lees-Edwards boundary condition induced artificial flows near the boundary, the localized analysis provided the data which is isolated from such an effect. From the local analysis, the yielding behavior was found to exist and the yield stress was found to be 5.7, which is in the same order as the yield stress values obtained from experiments.

### 3.3.3 Oscillatory shear flow behavior

As mentioned earlier, due to the ballistic nature of this simulation, the initial configuration of the system is important when conducting oscillatory shear tests. The residual stress levels for each mixing protocol were compared in Fig. 3.10 and it was found that the random motion only mixing protocol results in the lowest residual stress level, despite the lack of the local freezing. Thus, the initial configurations for the random motion only were used for the oscillatory tests and the hybrid mixing was used for a comparison. Also, in order to minimize the effect of the residual stresses, 8 to 16 initial configurations were obtained for each flow condition and the averaged value was used for the further analysis.

The oscillatory frequency values were kept as multiples of 10 and the value of  $\Delta t$  was varied accordingly. As mentioned earlier in the subsection 2.5, the maximum value of  $\Delta t$  allowed was  $10^{-5}$  and the  $\Delta t$  values were kept under

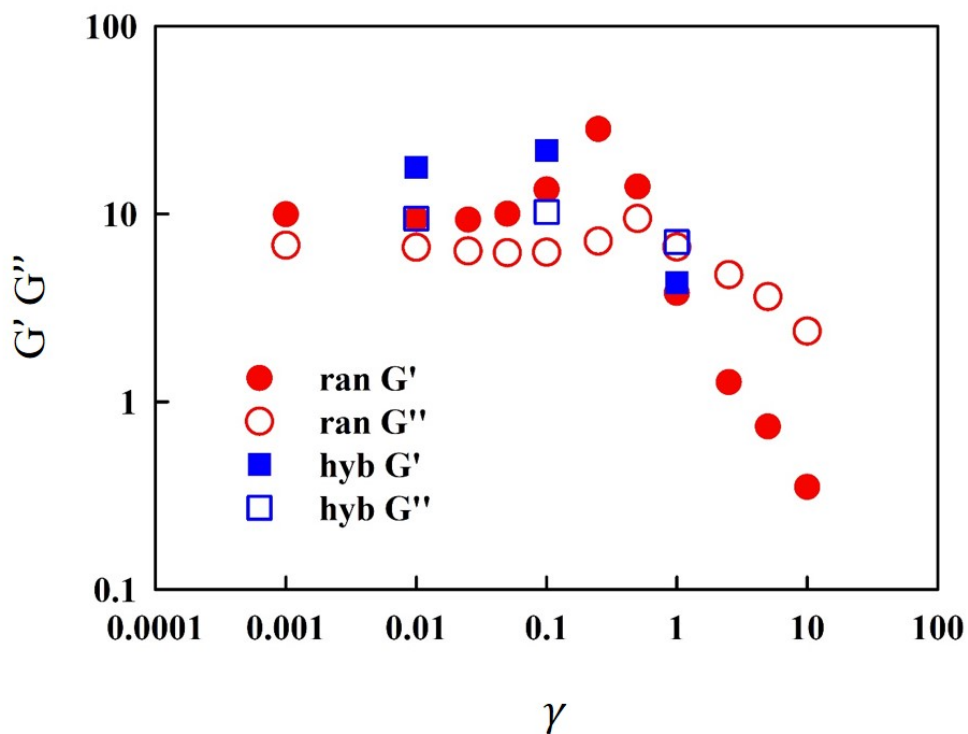


Figure 3.18 The oscillatory shear amplitude sweep graph at frequency of 10. Filled symbols indicate  $G'$  and empty symbols indicate  $G''$ . Red circles indicate the random motion only mixing protocol and blue squares indicate the hybrid mixing protocol.  $\phi_p=25$  vol%,  $\phi_f=2$  vol%,  $\kappa=0.4$ ,  $\theta_c=92$ .

that limit. The values of modulus were achieved via a linear regression. Total of 20 cycles were measured and the last three cycles were checked if they overlap well, then averaged and used for the further analysis. 1024 stress points and 50 configurations for the structure analysis were measured for each cycle.

For the random motion only case indicated by the red circles, the amplitude sweep data indicates that the values of  $G'$  is higher than those of  $G''$  at the low amplitude regime. Once the linear viscoelasticity disappears, the values of  $G'$  and  $G''$  show signs of stiffening followed by a rapid drop, eventually reaching the crossover point where the values of  $G''$  becomes higher than those of  $G'$ . The linear viscoelastic regime ranges from strain 0.001 to strain 0.05. The hybrid mixing data shows that the values of  $G'$  and  $G''$  are higher than those of the random motion only case, and the degree of stiffening is much less pronounced. The higher moduli at low strain seem to be originated from the local freezing network of the hybrid mixing case, which can be seen in Fig. 3.11.

At the strain of 0.01, the frequency sweep data were measured and are shown in Fig. 3.19. For the random motion only case, the frequency sweep data indicates that  $G'$  is higher than  $G''$  for low frequency, which is inverted somewhere between frequency 10 and 100. This result shows that at low frequency, the model capillary suspension exhibits a solid-like behavior where elasticity plays a major role. As frequency increases, the solid-like behavior becomes scarce and the model capillary suspension exhibits a liquid-like behavior eventually. The hybrid mixing case also exhibit a similar behavior with almost identical slope of both  $G'$  and  $G''$  to that of the random motion only case, but with higher values of  $G'$  and  $G''$ .

For the random motion only case, at the amplitudes beyond the linear viscoelastic regime, a strain-stiffening behavior of both  $G'$  and  $G''$  is observed. There are four known distinct types of LAOS behavior, strain thinning, strain

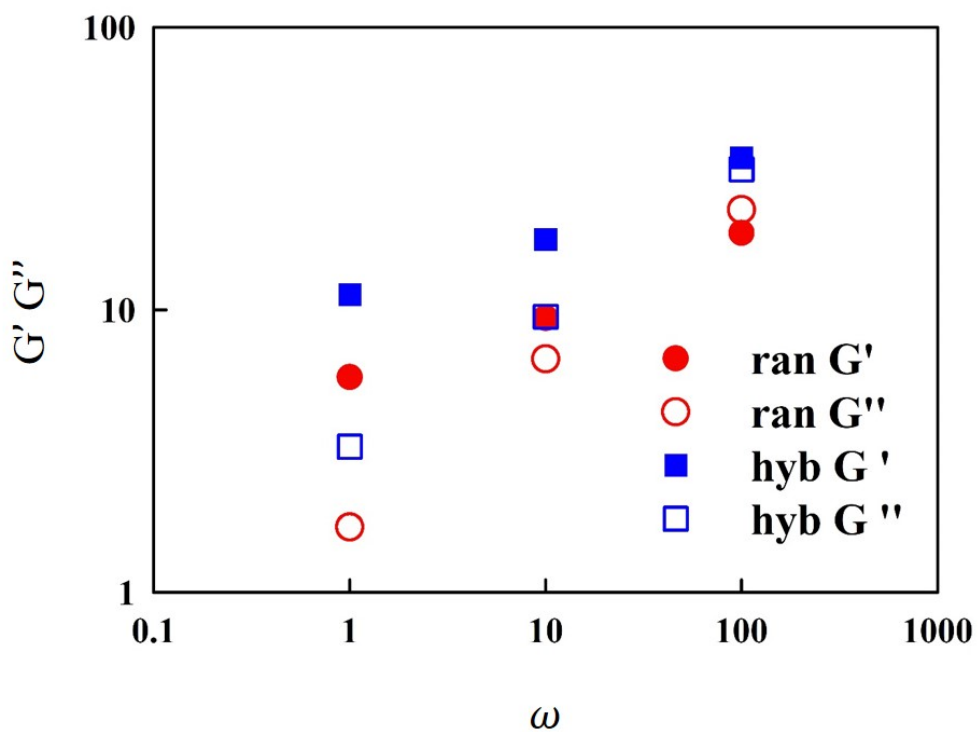


Figure 3.19 The oscillatory shear frequency sweep graph at a strain of 0.01. Filled symbols indicate  $G'$  and empty symbols indicate  $G''$ . Red circles indicate the random motion only mixing protocol and blue squares indicate the hybrid mixing protocol.  $\phi_p=25$  vol%,  $\phi_f=2$  vol%,  $\kappa=0.4$ ,  $\theta_c=92$ .

hardening, weak strain overshoot, and strong strain overshoot.[72] The behavior observed in Fig. 3.18 belongs to type IV LAOS behavior, which is the strong strain overshoot and such behavior has been observed in HASE/1M NaOH solution, colloidal aggregate gels of PS latex/water/MgCl<sub>2</sub>, or 10% silica suspension in PPG. The systems that exhibit such strain stiffening behavior are known to contain backbone segments, and the structural characteristics of the model capillary suspension need to be further investigated to explore the possible cause of such behavior.

In Fig. 3.20, the Cole-Cole plot at different strain amplitudes is demonstrated. In systems without the strain stiffening, the Cole-Cole plots are expected to shift left and downwards as the strain amplitude increases. However, in this system, the plot shifts right first due to the strain stiffening, then starts to shift left and downward.

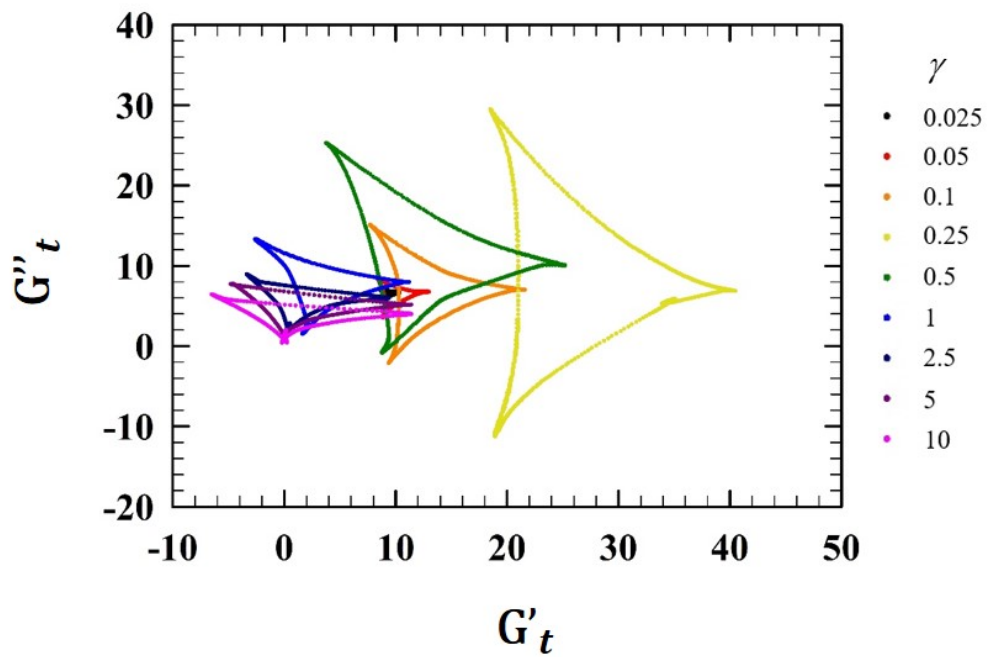


Figure 3.20 The Cole-Cole plot at different amplitudes of 0.025, 0.05, 0.1, 0.25, 0.5, 1, 2.5, 5, 10.

# Chapter 4

## Conculsion

### 4.1 Concluding remarks

To describe a capillary suspension via simulation, the biggest challenge is solving the free interface. There have been a few attempts to describe the capillary suspension through the simulations, but the scope of these studies has been limited to either small scale or observing the network formation. These limitations largely originate in the difficulties associated with solving the free interface of the secondary fluid in the capillary suspension system. The capillary force, which is the most important aspect of the sample-spanning network formation, comes from the surface energy and therefore, accurately predicting the droplet shape and size is important in describing the capillary suspension via a simulation. However, on top of the difficulties associated with the free interface, the actual phenomenon involves various other complexities, such as droplet distribution, coalescence, break-up, hydrodynamic interaction, etc, and it is very challenging to properly consider all of the aspects that may affect the system.

Thus, we chose to first develop a simulation methodology that can describe the capillary force with relatively low cost by adopting a coarse-grained approach.

The coarse-grained approach assumes that the secondary fluid exists as a superposable sphere with constant volume. Of course, the coarse-grained free interface will not perfectly agree with the actual secondary fluid free interface, yet, for some cases where the convex shape of the droplet is guaranteed, i.e. capillary state, the coarse-grained free interface will be capable of giving the parameters that closely mimic the real world. In the subsection 3.1.1, the resemblance of the coarse-grained droplets to the real world was examined, and as long as the droplet shape does not deviate much from a sphere, it can be assumed that the coarse-grained approach is reasonable.

Because we chose to simplify the free surface as spherical shape, the suggested coarse-graining is suitable only for the capillary state cases. To describe the pendular state, a different approach should be taken to simplify the free surface. For example, the pendular-shaped interface can be described as a volume-preserving cylindrical bridge with a changing height and radius, similar to our methodology. Using this assumption, one may easily derive the attractive interaction potential. However, it will be difficult to consider the transition of the shape (sphere to cylinder) before and after the bond formation. Also, there has been a study on how to simply express the concave and convex liquid bridge between two solid spheres,[52, 51] whose idea could be utilized and applied to this methodology to describe the pendular state capillary suspension.

While developing the coarse-grained approach, many assumptions were made and the limitations were followed. One such example is the assumption of no coalescence or break-up. By neglecting the coalescence and break-up, we had to carefully design the mixing protocols, consider the size distribution, and analyze the effect of the droplet-particle size ratio. The implementation of the

coalescence and break-up of the droplets is not only difficult, but also requires many other assumptions to be involved. Yet, there are some previous studies that can be adopted in this methodology to implement the break-up and the coalescence.

For the droplet break-up, some polymer melt studies can be referred to. In these studies, the authors use the capillary numbers to determine whether the droplet will break under the given shear. [73, 74] If the capillary number of the droplet does not reach the critical capillary number, the droplet will remain intact. When the droplet capillary number exceeds the critical capillary number, the droplet goes through a break-up. The critical capillary number, however, depends on what model is used to determine it and the model that is the most suitable to describe the capillary suspension system needs to be explored first. Once the critical capillary number is known, this methodology will provide a relatively easy way to determine the break-up of the droplets. The aforementioned studies on the droplet break-up also explored the coalescence of the droplets. When a certain shear rate and droplet size are determined, the maximum size of the coalesced droplet can be determined as well. This maximum size, however, is dependent on the model used to calculate it and therefore, like in the break-up case, the appropriate model for the coalescence needs to be carefully explore first as well.

Of other forces considered in this study, both the particle and the droplet experience the hard core repulsion forces. Though it is natural for the particles to experience the hard core repulsion, it is less likely for the droplets to experience one. Due to the current state of the development stage, the coalescence of the droplets, which would be more likely to happen than hard core repulsion when the droplets contact each other, is not yet considered. Nonetheless, the overlap rate upon the droplet collision is negligible due to the very low vol-

ume fraction of the droplets, and the hard core repulsion between the droplets does not affect the bulk properties significantly. Thus, the hard core repulsion of the droplets is in place just to make sure that the secondary fluid volume fraction stays constant throughout the simulation even if the actual effect of it is minimal.

The hydrodynamic friction forces are considered for both the particles and the droplets, yet, the two do not share the same hydrodynamic friction coefficient. The fluid droplets experience a different type of friction from what the solid particles experience due to the fact that the liquid-liquid interface has more complex factors involved under a drag force. Thus, the friction coefficient of the droplets based on the droplet viscosity is calculated and the droplets were exposed to the frictions accordingly. This is the least we did to consider the hydrodynamic interaction in this study. However, taking a full consideration of the hydrodynamic interaction, though computationally high-cost, would carry more accuracy and should be of consideration in future studies.

The last, but not least, important force is the friction force of the droplet on the particle surface. In this study, the droplet friction on the particle surface was simplified to a pinning force that prevents the tangential slip of the droplet by adding a recovery force in the opposite direction of the slip. The value of the constant  $K$  was set to a maximum value, above of which will cause a numerical instability, regardless of other simulation conditions. However, the value of  $K$  should in fact be a function of the contact angle. One other aspect we did not explore deeper is the conservation of the torque, and the excess torque exerted by the particle on the droplet is handled simply by resetting the torque at certain time span. There are many other approaches that could be applied to encounter this, such as rotating the entire network to the same amount of residual torque or considering the droplet rotation as well. The former would be

simpler and more practical considering the cost while the latter would require a careful investigation on how the fluid droplet would rotate upon the disturbance caused by a solid interface.

The contact angle hysteresis utilized in this study is a simple spring force-like version that only considers the rotation of the particles. In a study, the contact angle hysteresis of liquid bridges was investigated and this could be utilized to elaborate the forces involved in the contact angle hysteresis. [75] Meanwhile, another study suggested a model to describe the contact angle hysteresis. [76] Also, the torque conservation can be handled with more sophisticated methods to better represent the physical phenomenon. As of now, for simplicity, the torque is reset regularly to prevent it affecting the measured stress. Another way to go around this issue would be to calculate the sum of the entire torque generated within a cluster and apply the equivalent amount of torque in the opposite direction. Yet, these methods are mere detours to patch up the lack of the fluid droplet rotation due to the particle friction. The best resolution is to carefully examine how the fluid droplet would react to the friction caused by the particle in contact and find a cost efficient way of achieving it into the simulation.

The hydrodynamic interaction is another issue that may enrich the current state of the simulation and taking the hydrodynamic interaction into account would be eventually of interest. There are some mesoscale computational techniques that can be utilized to describe the hydrodynamic interactions. [77, 78, 79] Yet, these methods of implementing the hydrodynamic interaction to a simulation are cost-heavy and because this study aims to secure practically as many particles as possible to calculate the rheological properties, reducing the computation cost is of the most importance. Thus, it was not considered at this stage of the study, and even without the hydrodynamic interaction,

the sample-spanning network formed by the particles and the droplets exhibits unique behaviors that may bring about important messages regarding the capillary suspension.

Also, this methodology could be further developed to describe ternary systems other than the capillary suspension. For example, a Pickering emulsion typically has a spherical shaped droplets surrounded by particles. With the implementation of coalescence, break-up, and HI interaction, the simulation of some Pickering emulsions would become possible. Another example would be the late drying stage where we can assume the primary fluid as air and the secondary fluid as a fluid that keeps decreasing in size as the drying proceeds. By doing so, the drying stress could be explored through a simulation.

There are some interesting characteristics that the capillary suspension exhibit under oscillatory flows, such as the multi-tier yielding that appears in the amplitude sweep in oscillatory tests at a high solid volume fraction ( $\phi_p > 0.45$ ). This suggests that the yielding occurs in various length scales in the capillary suspension, and investigating what causes such behavior would result in a meaningful work.

## 4.2 Conclusion

In this study, a new methodology was suggested to describe the behavior of the capillary suspensions by employing the capillary force derived from a coarse-grained potential. The secondary fluid, or the droplet, was assumed to be the superposable spherical particle with a constant volume, and the free surface between the particle and the droplet was expressed in a simple manner. Under this assumption, the change in the interfacial area between the particle and the droplet was computed. Through this, the interaction between the particles

by the surface excess energy at the interface could be calculated. As a result, a coarse-grained model that was cost efficient was achieved, and a sufficient amount of particles was secured to calculate the rheological properties.

Prior to the full simulation, the parameter limitation for the coarse-grained model was explored, and the effect of contact angle,  $\theta_c$ , and the droplet to particle size ratio,  $\kappa$ , was probed in advance. For  $\theta_c$ , the model prediction was accurate for the capillary state with the contact angle of 90 degrees or higher, and  $\theta_c$  of 92 degrees was used in the simulation. The contact angle analysis indicates that the contact angles lower than 90 degrees still carry decent accuracy at high values of  $\kappa$ . However, due to the spherical shape assumption, the convex shape of the droplet will be present at all times and the methodology lacks the ability to accurately explore the concave shaped droplet bridges, and the application of the coarse-graining onto pendular states should be approached with more care. For  $\kappa$ , the analysis on the maximum cluster size and the particle bond number on the droplet implied that the capillary suspension was best described when  $\kappa$  was 0.4. When the value of  $\kappa$  is low, although the cluster size becomes larger due to the high number of droplets available to connect the particles, the droplets are either too small to connect more than two particles at once or present with multiple other droplets in between a single particle pair. Higher values of  $\kappa$  than 0.4 result in smaller cluster size and therefore, to maintain the maximum cluster size and sample-spanning network,  $\kappa$  higher than 0.4 was excluded. All of the four characteristic variables in this study,  $\phi_p$ ,  $\phi_f$ ,  $\kappa$ , and  $\theta_c$ , play important roles in determining the properties of the model system developed by this methodology. However, since the key aspect of the capillary suspension is the capillary force exerted by the secondary fluids,  $\phi_f$  and  $\kappa$  are of the most importance of these four. The sample-spanning network, which is the key characteristic of the capillary suspension, is affected the most

by  $\phi_f$  and  $\kappa$  and a careful tuning process of these two parameters is necessary.

Meanwhile, the effect of the polydispersity in the droplet size was explored. Two modes, uniform and polydisperse, of the droplets were tested at  $\kappa = 0.4$ , with the polydispersity applied to have a normal distribution with a minimum of 0.1 to prevent the possible numerical instability. This resulted in a reduced number of droplets compared to the uniform case. The flow curve of the two shows little difference with an exception at the very low shear rate and the different at this shear rate is assumed to attribute to the high error. The low shear viscosity with respect to the secondary fluid volume fraction, on the other hand, showed considerably different behaviors at the secondary fluid volume fraction of 0.5 to 1 vol %. Due to the lower number of the droplets on average due to polydispersity, the number of the droplets available to form the network is less and this leads to the slower formation of the capillary network. However, the two formed plateau at similar viscosity and this indicates that once there are enough droplets to form the sample-spanning network, the polydispersity has little effect on the rheological property, and this is also shown in the flow curve. Thus, the polydispersity is neglected in the following experiments to maintain the minimum number of free parameter.

Using these parameters, the initial structure was established using a multi-step initialization. The different modes of the initial mixing are important in this study due to the ballistic nature of this study, meaning that the study lacks the random motion that will keep stabilizing and rearranging the network. Thus, once the initial mixing is done, the network bears the residual stress that is inherit due to the network formed by the mixing and the residual stress cannot dissipate. Three modes of the initial mixing were tested by combining shear and random motion. The mixing is generally composed of three steps, initial mixing, low shear mixing, then resting. The low shear mixing is applied to

induce a freezing in the network. A strong shear or random motion by itself cannot produce a local freezing and mainly aims to induce the most collision between the particles and the droplets. Then, applying a low shear mixing causes local rearrangements of the network, which results in a local freezing. Then, the stress is allowed to dissipate by applying a resting step. Results show that when a shear is the only means for mixing, the residual stress level was medium with a combination being the highest and a random motion only being the lowest. The non-zero residual stress indicates that the network have a directional tendency, and the low(almost 0) residual stress indicates that the network has no directional tendency. In this study, the interest lies in observing the local freezing and yielding behavior, and therefore, we adopted the shear only mixing to use in a simple shear experiment. However, depending on the need, the mixing protocol should be tailored with care since the simulation is ballistic.

The analysis on the structure and the rheological properties were conducted under various flow conditions, along with the analysis on the yielding behavior. The viscosity curve exhibited a strong shear thinning behavior with a slope of -0.7 while the maximum cluster size remained above 9,000 out of total 10,000 particles. Although the cluster size did not exhibit a dramatic change, this cannot directly infer that the capillary network is not affected by the flow. The cluster size is mainly measured by examining if there is any kind of connection, and the cluster size staying constant only means that the rate of formation is high enough to maintain the cluster. A deeper investigation on how the cluster is affected in smaller scales, such as local flocs, should be investigated in future studies as well. To evaluate the yielding behavior, the local strain and stress of locally frozen regions of low shear rate regimes (shear rate of 0.10, 0.18, 0.32) were investigated to reveal the elastic behavior, which was then analyzed

relating to the yielding behavior. Also, through this process, we were able to point out a transition from the elastic behavior to the viscous behavior, and the stress at that transition was inferred as the yield stress. The dimensionless yield stress reported in the literature was between 1 and 3, [71] and was similar to the value acquired in the simulation, 5.7.

The aforementioned analysis confirms that the coarse-grained potential used to describe the capillary suspension is capable of reflecting the key characteristic of the capillary suspension, the yielding behavior observed in previous experiments.[1] This opened up an opportunity to make progress on the investigations that were otherwise hard to achieve due to limitations in experiments, such as how the local networks rearrange when exposed to the stress lower than the yield stress.

Because the droplet coalescence or break-up was not accounted for, the initial configuration was built under several assumptions, such as monodisperse droplet size distribution or fixed  $\kappa$  and a hard-core repulsion between the droplets, which can be improved in future studies. Considering the droplet coalescence and break-up will have a great impact on this methodology due to many aspects that can be affected by it. The relationship between  $\kappa$  and  $\phi_f$ , which is the key to the initial formation of capillary suspension at low secondary fluid volume fraction, could either be defined separately or just taken into account by a part of the droplet coalescence and break-up calculation. This will enrich the understanding of the capillary suspension formation and give more insights on how the initial mixing protocol would affect the rheological properties. Also, the consideration of the coalescence and break-up may help investigate the structural changes of the capillary network, for example, the shattering of the droplet under the strong deformation and the restructuring at rest.

Lastly, oscillatory shear tests were conducted using this methodology. The

amplitude sweep data indicated that there was a strain-stiffening, which can be classified as the type IV LAOS behavior, and the SPP analysis was performed. The SPP data can be further interpreted by analyzing the microstructure during the oscillatory flow. For the structure analysis, the number of droplets on particle, the number of particles on droplet, the cluster size, and the average droplet radius can be measured and used. The bond number and cluster size analysis provides the information on how the sample-spanning network is affected by the oscillatory flow. The average droplet radius has a linear correspondence to both the strength of the force exerted by the droplet and the distance between the particles.

Although the methodology suggested in this study is based on a coarse-graining and has many aspects that could be improved, it managed to describe the capillary suspension successfully, which has not been done until now. Also, the local freezing that leads to the yielding behavior has not yet been investigated through a particle simulation until now. Thus, the significance of this study lies in its ability to describe a ternary system via a coarse-grained approach and to demonstrate an yielding behavior via a particle simulation, which is also an important aspect in describing the capillary suspension. There are some aspects of the capillary suspension that is hard to be observed through experiments due to the physical limitations. For example, the reconstruction of the capillary suspension after a high shear rate was applied could not be observed yet due to the short time scale it occurs at. To observe and understand such aspects of the capillary suspension, a simulation tool can be very useful. Together with the suggested future improvements, the methodology bears a great potential to enrich the understanding of the capillary suspension.

# Appendix A

## Formulation

The relation between the particle and the droplet radii,  $a$  and  $R$ , can be defined using  $x$  and  $d$ .

$$\begin{aligned}R^2 - (d - x)^2 &= a^2 - x^2 \\ -a < x &= \frac{d^2 + a^2 - R^2}{2d} < a \\ d - x &= \frac{d^2 + R^2 - a^2}{2d}\end{aligned}$$

Then, the volume occupied by the particle and therefore excluded from the droplet,  $V_{ex}$  can be defined.

$$\begin{aligned}V_{ex} &= \int_x^a \pi(a^2 - t^2)dt + \int_{d-x}^R \pi(R^2 - t^2)dt \\ &= \pi[a^2t - \frac{1}{3}t^3]_x^a + \pi[R^2t - \frac{1}{3}t^3]_{d-x}^R \\ &= \pi \left( \frac{2}{3}a^3 + \frac{2}{3}R^3 - a^2x + \frac{1}{3}x^3 - R^2(d-x) + \frac{1}{3}(d-x)^3 \right) \\ V_{ex} &= \frac{\pi}{3} (2a^3 + 2R^3 - 3(a^2x + R^2(d-x)) + x^3 + (d-x)^3)\end{aligned}$$

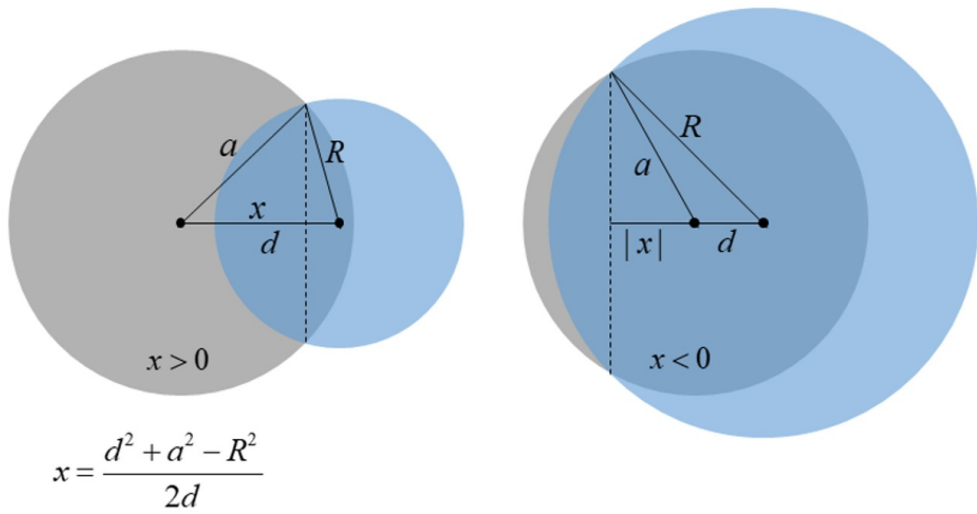


Figure A.1 A demonstration of the variables used in the formulation process. Grey spheres are the particles and blue spheres are the droplets.  $a$ ,  $R$ ,  $d$ ,  $x$  represent the particle radius, the droplet radius, the distance between the centers of the particle and the droplet, and the distance between the particle center and the cross-section where the particle and the droplet cross.

By modifying the variables, simplified version of  $V_{ex}$  can be obtained.

$$a^2x = \frac{a^2d^2 + a^4 - a^2R^2}{2d}$$

$$R^2(d-x) = \frac{d^2R^2 + R^4 - R^2a^2}{2d}$$

$$x^3 + (d-x)^3 = d(d^2 - 3dx + 3x^2)$$

$$V_{ex} = \frac{\pi}{3} (2a^3 + 2R^3 - 3(a^2x + R^2(d-x)) + x^3 + (d-x)^3)$$

$$R^2(d-x) = \frac{d^2R^2 + R^4 - R^2a^2}{2d}$$

$$a^2x = \frac{a^2d^2 + a^4 - a^2R^2}{2d}$$

$$x^3 + (d-x)^3 = d^3 - 3d^2x + 3dx^2 = -\frac{d^3 + 3da^2 - 3dR^2}{2} + 3dx^2$$

$$x = \frac{d^2 + a^2 - R^2}{2d}$$

$$V_{ex} = \frac{\pi}{6} \left( 4a^3 + 4R^3 - 3 \left( a^2d + dR^2 + \frac{a^4 - 2a^2R^2 + R^4}{d} \right) - d^3 - 3da^2 + 3dR^2 + 6dx^2 \right)$$

$$6dx^2 = \frac{3(d^4 + a^4 + R^4)}{2d} + 3 \frac{a^2d^2 - d^2R^2 - a^2R^2}{d}$$

Substituting the above equations into  $V_{ex}$ , we get the following.

$$\begin{aligned} V_{ex} &= \frac{\pi}{6} \left( 4a^3 + 4R^3 - 3 \left( a^2d + dR^2 + \frac{a^4 - 2a^2R^2 + R^4}{d} \right) - d^3 \right) \\ &\quad + 3dR^2 + \frac{3(d^4 + a^4 + R^4)}{2d} + 3 \frac{a^2d^2 - d^2R^2 - a^2R^2}{d} \end{aligned}$$

$$= \frac{\pi}{12} \left( 8a^3 + 8R^3 - 6a^2d - 6dR^2 - \frac{6a^4 - 12a^2R^2 + 6R^4}{d} - 2d^3 \right) \\ + 6dR^2 + \frac{3(d^4 + a^4 + R^4)}{d} + \frac{-6d^2R^2 - 6a^2R^2}{d}$$

$$= \frac{\pi}{12} \left( 8a^3 + 8R^3 - 6a^2d - 6dR^2 - 2d^3 + 6dR^2 + \frac{3d^4 - 6d^2R^2 - 3a^4 - 3R^4 + 6a^2R^2}{d} \right)$$

$$= \frac{\pi}{12} \left( 8a^3 + 8R^3 - 6a^2d - 6dR^2 - 2d^3 + 6dR^2 + 3d^3 - 6dR^2 - 3 \frac{a^4 - 2a^2R^2 + R^4}{d} \right)$$

$$= \frac{\pi}{12} \left( 8a^3 + 8R^3 - 6d(a^2 + R^2) + d^3 - 3 \frac{(a^2 - R^2)^2}{d} \right)$$

Then,  $V_{ex}$  can be simply expressed as follows.

$$V_{ex}(d) = \frac{\pi}{12} \left( d^3 + 8(a^3 + R^3) - 6d(a^2 + R^2) - 3 \frac{(a^2 - R^2)^2}{d} \right)$$

Due to the volume conservation,  $V_0$  needs to be constant, meaning that the current volume minus the excluded volume should equal to  $V_0$ .

$$\frac{4}{3}\pi R^3 - \sum_i V_{ex}(d_i) = V_0$$

Substituting  $V_{ex}$ , we get the following.

$$\begin{aligned} \frac{4}{3}\pi R^3 - \frac{\pi}{12} \sum_i \left( d_i^3 + 8(a^3 + R^3) - 6d_i(a^2 + R^2) - 3 \frac{(a^2 - R^2)^2}{d_i} \right) &= V_0 \\ 4\pi R^2 \frac{\partial R}{\partial d_i} - \frac{\pi}{12} \left( 3d_i^2 - 6(a^2 + R^2) + 3 \frac{(a^2 - R^2)^2}{d_i^2} \right) \\ - \frac{\pi}{12} \sum_j \left( 24R^2 - 12d_j R - 12 \frac{R(R^2 - a^2)}{d_j} \right) \frac{\partial R}{\partial d_i} &= 0 \\ R \left( 4R - 2N_b R + \sum_j \left( d_j + \frac{R^2 - a^2}{d_j} \right) \right) \frac{\partial R}{\partial d_i} &= \frac{1}{4} \left( d_i^2 - 2(a^2 + R^2) + \frac{(a^2 - R^2)^2}{d_i^2} \right) \end{aligned}$$

Next, each type of surface area needs to be considered. First, the total surface area can be expressed as follows.

$$2\pi r^2 \int_0^\theta \sin t dt = 2\pi r^2 (1 - \cos \theta)$$

particle-droplet area is as follows.

$$\begin{aligned} \cos \theta &= \frac{x}{a} = \frac{d^2 + a^2 - R^2}{2ad} \\ A_{S2,i} &= 2\pi a^2 \left( 1 - \frac{d_i^2 + a^2 - R_i^2}{2ad_i} \right) < 4\pi a^2 \end{aligned}$$

particle-primary fluid area is as follows.

$$A_{S1} = 4\pi a^2 - \sum_i A_{S2,i}$$

droplet-dummy area is as follows.

$$A_{dum,j} = 2\pi R^2 \left( 1 - \frac{d_j^2 + R^2 - a^2}{2Rd_j} \right)$$

primary fluid-droplet area is as follows.

$$A_{12} = 4\pi R^2 - \sum_j A_{dum,j}$$

total area of each interface is as follows.

$$\begin{aligned} \sum_j \left( \sum_{I \in j} A_{S2,I}(d_{(I,j)}) \right) &= \sum_{(i,j)} A_{S2,I}(d_{(I,j)}) \\ \sum_I \left( 4\pi a^2 - \sum_{j \in I} A_{S2,I}(d_{(I,j)}) \right) &= 4\pi a^2 N_p - \sum_{(i,j)} A_{S2,I}(d_{(I,j)}) \\ \sum_j \left( 4\pi R^2(d_{(I,j)}) - \sum_{I \in j} A_{dum,I}(d_{(I,j)}) \right) &= 4\pi \sum_j R^2(d_{(I,j)}) - \sum_{(i,j)} A_{dum,I}(d_{(I,j)}) \end{aligned}$$

where

$$\begin{aligned} A_{S2,i} &= 2\pi a^2 \left( 1 - \frac{d_i^2 + a^2 - R_i^2}{2ad_i} \right) \\ A_{dum,j} &= 2\pi R^2 \left( 1 - \frac{d_j^2 + R^2 - a^2}{2Rd_j} \right) \end{aligned}$$

By substituting the variables, the first equation can be simplified and differentiated as follows.

$$\begin{aligned} \sum_j \left( \sum_{I \in j} A_{S2,I}(d_{(I,j)}) \right) &= \sum_j \left( \sum_{I \in j} 2\pi a^2 \left( 1 - \frac{d_{Ij}^2 + a^2 - R_j^2}{2ad_{Ij}} \right) \right) = \pi a \sum_j \left( \sum_{I \in j} \left( a - d_{Ij} - \frac{a^2}{d_{Ij}} + \frac{R_j^2}{d_{Ij}} \right) \right) \\ \pi a \frac{\partial}{\partial d_{Ij}} \sum_j \left( \sum_{I \in j} \left( a - d_{Ij} - \frac{a^2}{d_{Ij}} + \frac{R_j^2}{d_{Ij}} \right) \right) &= \pi a \left( -1 + \frac{a^2}{d_{Ij}^2} - \frac{R_j^2}{d_{Ij}^2} + 2R_j \sum_{K \in j} \left( \frac{1}{d_{Kj}} \right) \frac{\partial R_j}{\partial d_{Ij}} \right) \\ &= -\pi a \left( \frac{d_{Ij}^2 + R_j^2 - a^2}{d_{Ij}^2} - 2R_j \sum_{K \in j} \left( \frac{1}{d_{Kj}} \right) \frac{\partial R_j}{\partial d_{Ij}} \right) \end{aligned}$$

With a similar approach, the second equation can be simplified and differentiated as follows.

$$\begin{aligned} \frac{\partial}{\partial d_{Ij}} \sum_I \left( 4\pi a^2 - \sum_{j \in I} A_{S2,I}(d_{(I,j)}) \right) &= \frac{\partial}{\partial d_{Ij}} \left( 4\pi a^2 N_p - \sum_{(i,j)} A_{S2,I}(d_{(I,j)}) \right) \\ &= -\frac{\partial}{\partial d_{Ij}} A_{S2,I}(d_{(I,j)}) = \pi a \left( \frac{d_{Ij}^2 + R_j^2 - a^2}{d_{Ij}^2} - 2R_j \sum_{K \in j} \left( \frac{1}{d_{Kj}} \right) \frac{\partial R_j}{\partial d_{Ij}} \right) \end{aligned}$$

Lastly, the third equation can be simplified and differentiated as follows.

$$\begin{aligned} &\frac{\partial}{\partial d_{Ij}} \sum_k \left( 4\pi R_k^2(d_{(I,k)}) - \sum_{K \in k} A_{dum,K}(d_{(K,k)}) \right) \\ &= 8\pi R_j \frac{\partial R_j}{\partial d_{Ij}} - \pi \frac{\partial}{\partial d_{Ij}} \left( \sum_{K \in j} R_j^2 \left( 2 - \frac{d_{Kj}^2 + R_j^2 - a^2}{R_j d_{Kj}} \right) \right) \\ &= 8\pi R_j \frac{\partial R_j}{\partial d_{Ij}} - 2\pi R_j \frac{\partial R_j}{\partial d_{Ij}} \sum_{K \in j} \left( 2 - \frac{d_{Kj}^2 + R_j^2 - a^2}{R_j d_{Kj}} \right) + \pi R_j^2 \frac{\partial}{\partial d_{Ij}} \sum_{K \in j} \frac{d_{Kj}^2 + R_j^2 - a^2}{R_j d_{Kj}} \\ &= 8\pi R_j \frac{\partial R_j}{\partial d_{Ij}} - 2\pi R_j \frac{\partial R_j}{\partial d_{Ij}} \sum_{K \in j} \left( 2 - \frac{d_{Kj}^2 + R_j^2 - a^2}{R_j d_{Kj}} \right) + \pi R_j^2 \left( \frac{\partial R_j}{\partial d_{Ij}} \sum_{K \in j} \left( \frac{R_j^2 + a^2 - d_{Kj}^2}{R_j^2 d_{Kj}} \right) + \frac{d_{Ij}^2 + a^2 - R_j^2}{R_j d_{Ij}^2} \right) \\ &= 8\pi R_j \frac{\partial R_j}{\partial d_{Ij}} - 2\pi \frac{\partial R_j}{\partial d_{Ij}} \sum_{K \in j} \left( 2R_j - \frac{d_{Kj}^2 + R_j^2 - a^2}{d_{Kj}} \right) + \pi \frac{\partial R_j}{\partial d_{Ij}} \sum_{K \in j} \left( \frac{R_j^2 + a^2 - d_{Kj}^2}{d_{Kj}} \right) + \pi R_j \frac{d_{Ij}^2 + a^2 - R_j^2}{d_{Ij}^2} \\ &= \pi \frac{\partial R_j}{\partial d_{Ij}} \left( 8R_j - 4N_b R_j + \sum_{K \in j} \left( \frac{d_{Kj}^2 + 3R_j^2 - a^2}{d_{Kj}} \right) \right) + \pi R_j \frac{d_{Ij}^2 + a^2 - R_j^2}{d_{Ij}^2} \end{aligned}$$

Using the surface energy definition, the force exerted on particle-droplet pair can be expressed as follows.

$$\begin{aligned} E(d_{(I,j)}) &= \sum_j \left( \Gamma_{S2} \sum_{I \in j} A_{S2,I}(d_{(I,j)}) + \Gamma_{12} \left( 4\pi R^2(d_{(I,j)}) - \sum_{I \in j} A_{dum,I}(d_{(I,j)}) \right) \right) \\ &+ \Gamma_{S1} \sum_I \left( 4\pi a^2 - \sum_{j \in I} A_{S2,I}(d_{(I,j)}) \right) \\ \mathbf{F}_I &= -\nabla_I d_{Ij} \frac{\partial E}{\partial d_{Ij}} \\ \mathbf{F}_j &= -\mathbf{F}_I \end{aligned}$$

Substituting the differentiated equations above, the following is done to define the capillary force acting on the particle I by the droplets that are in contact with the particle I.

$$\frac{\partial}{\partial d_{Ij}} \sum_j \left( \sum_{I \in j} A_{S2,I}(d_{(I,j)}) \right) = -\pi a \left( \frac{d_{Ij}^2 + R_j^2 - a^2}{d_{Ij}^2} - 2R_j \sum_{K \in j} \left( \frac{1}{d_{Kj}} \right) \frac{\partial R_j}{\partial d_{Ij}} \right)$$

$$\begin{aligned} & \frac{\partial}{\partial d_{Ij}} \sum_k \left( 4\pi R_k^2(d_{(I,k)}) - \sum_{K \in k} A_{dum,K}(d_{(K,k)}) \right) \\ &= \pi \frac{\partial R_j}{\partial d_{Ij}} \left( 8R_j - 4N_b R_j + \sum_{K \in j} \left( \frac{d_{Kj}^2 + 3R_j^2 - a^2}{d_{Kj}} \right) \right) + \pi R_j \frac{d_{Ij}^2 + a^2 - R_j^2}{d_{Ij}^2} \end{aligned}$$

$$\frac{\partial}{\partial d_{Ij}} \sum_I \left( 4\pi a^2 - \sum_{j \in I} A_{S2,I}(d_{(I,j)}) \right) = \pi a \left( \frac{d_{Ij}^2 + R_j^2 - a^2}{d_{Ij}^2} - 2R_j \sum_{K \in j} \left( \frac{1}{d_{Kj}} \right) \frac{\partial R_j}{\partial d_{Ij}} \right)$$

$$\begin{aligned} \mathbf{F}_I &= -\nabla_I d_{Ij} \frac{\partial E}{\partial d_{Ij}} \\ &= -\nabla_I d_{Ij} \left( \begin{aligned} & (\Gamma_{S1} - \Gamma_{S2}) \pi a \left( \frac{d_{Ij}^2 + R_j^2 - a^2}{d_{Ij}^2} - 2R_j \sum_{K \in j} \left( \frac{1}{d_{Kj}} \right) \frac{\partial R_j}{\partial d_{Ij}} \right) \\ & + \Gamma_{12} \left( \pi \frac{\partial R_j}{\partial d_{Ij}} \left( 8R_j - 4N_b R_j + \sum_{K \in j} \left( \frac{d_{Kj}^2 + 3R_j^2 - a^2}{d_{Kj}} \right) \right) + \pi R_j \frac{d_{Ij}^2 + a^2 - R_j^2}{d_{Ij}^2} \right) \end{aligned} \right) \\ & \frac{\partial R_j}{\partial d_{Ij}} = \frac{d_{Ij}^2 - 2(a^2 + R_j^2) + \frac{(a^2 - R_j^2)^2}{d_{Ij}^2}}{4R_j \left( 4R_j - 2N_b R_j + \sum_{K \in j} \left( d_{Kj} + \frac{R_j^2 - a^2}{d_{Kj}} \right) \right)} \end{aligned}$$

$$V_{ex}(d) = \frac{\pi}{12} \left( d^3 + 8(a^3 + R^3) - 6d(a^2 + R^2) - 3 \frac{(a^2 - R^2)^2}{d} \right)$$

$$\frac{4}{3} \pi R_j^3 - \sum_{K \in j} V_{ex}(d_{Kj}) = V_0$$

## 초록

모세관 현탁액은 하나의 고체와 두개의 섞이지 않는 유체들을 포함하는 3상계 시스템이다. 두 유체 중 소량으로 첨가되는 유체를 2차 유체라고 하며 2차 유체가 1차 유체에 분산되어 있는 입자들 사이에 위치하며 샘플-스패닝 구조를 형성하게 되고, 이는 유변 물성의 큰 변화로 이어지게 된다. 현재까지의 모세관 현탁액에 대한 시뮬레이션 연구는 국소 응집체나 형태에 대한 작은 규모의 분석에만 국한되어 있다. 본 논문에서는 2차 유체와 입자 간의 상호 작용을 근사하는 입자 시뮬레이션으로 모세관 현탁액을 묘사하는 방식이 제안되었고, 이를 통해 흐름 하에서의 모세관 현탁액의 구조와 유변 물성을 조사하였다. 실제 자유 계면을 푸는 과정에 포함되는 다수의 편미분 방정식들과 계산을 위해 필요한 많은 양의 계산 자원으로 인해 근사적 접근법은 모세관 현탁액을 입자 시뮬레이션으로 구현하는 데 있어서 필수적이다. 두 유체의 자유 계면은 구형으로 가정되었으며 고체 표면에서 부분적으로 겹쳐질 수 있고 부피가 일정하다는 가정을 적용시켰다. 입자를 이어주는 2차 유체로부터 기인하는 모세관력은 입자와 2차 유체 간 거리가 변하며 생기는 표면 에너지의 차이를 고려함으로써 묘사되었다. 2차 유체가 입자와 만났을 때 2차 유체의 부피 유지를 위해 반경이 커지게 되며 2차 유체가 입자와 떨어질 때도 마찬가지로 묘사된다. 표면적의 변화는 표면 에너지의 변화로 이어지게 되며 입자 간 작용하는 힘은 이 표면 에너지를 최소화 하는 방향으로 작용된다. 이 방법론을 통해 다양한 조건에서 모세관 현탁액의 형성이 실험되었으며 샘플-스패닝 구조가 얻어졌다. 이 때 모세관 현탁액의 구조와 모세관력을 결정짓는 특성 변수들로는 입자의 부피분율( $\phi_p$ ), 2차 유체의 부피분율( $\phi_f$ ), 3상 접촉각( $\theta_c$ ), 2차 유체와 고체 간의 크기비( $\kappa$ )가 있다. 각각의 특성 변수가 모세관 현탁액의 형성과 구조에 미치는 영향들은 응집체 크기 분석, 본드 넘버 분석, 유변 물성을 통해 조사되었고, 다양한 조건의 믹싱 프로토콜의 영향 또한 조사되었다. 특성 변수들의 최적값을 가

지고 25 vol%의 입자 부피분율, 2 vol%의 2차 유체 부피분율, 92도의 3상 접촉각, 0.4의 2차 유체와 고체 간의 크기 비를 가지는 모델 모세관 현탁액을 형성하였고, 이 모델 모세관 현탁액의 구조 및 흐름 특성이 조사되었다. 보다 더 정확한 유변 물성 측정을 위해 10,000개의 입자와 부피 분율과 크기비에 상응하는 개수의 2차 유체가 들어갔다. 2차 유체 부피 분율 변화에 따른 저전단 점도의 경향성은 실험에서 저전단 점도가 2차 유체 부피 분율에 대해 가지는 의존성과 비슷한 결과를 보여주었다. 레이트 스위프 분석을 통해 모세관 현탁액이 강한 전단 박화를 보여줌을 알 수 있었으며, 낮은 전단 속도의 영역에서는 국소 동결로 인해 전단 응력의 급격한 경사 변화가 일어나는 것을 관찰할 수 있었다. 무차원 전단 속도가 0.5보다 낮을 때 시뮬레이션의 흐름 특성들은 국소 동결의 징후를 보였고 리즈-에드워즈 경계 조건으로 인해 나타나는 국소 동결은 재어진 점도나 응력에 반영되지 않았다. 따라서, 동결된 부분의 국소 물성들은 전체적인 물성들과 분리되어 따로 조사되었다. 국소 물성들은 시뮬레이션 영역을 y 방향으로 잘게 나눈 후 각각의 구획에서 측정된 입자의 속도와 응력을 통해 측정되었다. 국소 동결이 일어나는 부분에서 국소 응력은 국소 변형과 비례하게 증가하는 양상을 보였으며 이는 탄성의 발현으로 볼 수 있다. 이는 물질이 주어진 변형에 저항하여 구조를 유지하려는 것을 나타내고 주어진 변형과 관찰되는 변형 간의 차이는 항복 응력의 영향으로 해석될 수 있다. 다른 전단 속도에서도 국소 동결이 발생하는 전단 속도에 한하여 국소 물성 분석이 이루어졌으며, 탄성이 사라지는 응력의 값이 측정되었다. 이 항복 응력은 무차원 형태로 5.7의 값을 가지는 것으로 계산되었고, 이는 이전 연구에서 보고된 값들과 유사함을 알 수 있었다. 진동 흐름 하에서 진폭 스위프 실험이 이루어졌으며 0.1의 변형에서 변형 농화가 관찰되었다. 진폭 스위프 결과는 시퀀스 오브 피지컬 프로세스 방식을 통해 분석되었다. 본 연구는 근사적 접근법을 포함한 방법론을 제시함으로써 모세관 현탁액을 시뮬레이션으로 묘사하고자 하였으며 모세관 현탁액의 주요 특성들을 성공적으로 재현해내었다.

**주요어:** 모세관 현탁액, 입자 시뮬레이션, 항복 응력, 국부 동결

**학번:** 2015-30219

# Bibliography

- [1] E. Koos and N. Willenbacher, “Capillary forces in suspension rheology,” *Science*, vol. 331, no. 6019, pp. 897–900, 2011.
- [2] S. S. Velankar, “A non-equilibrium state diagram for liquid/fluid/particle mixtures,” *Soft Matter*, vol. 11, no. 43, pp. 8393–403, 2015.
- [3] S. J. Heidlebaugh, T. Domenech, S. V. Iasella, and S. S. Velankar, “Aggregation and separation in ternary particle/oil/water systems with fully wettable particles,” *Langmuir*, vol. 30, no. 1, pp. 63–74, 2014.
- [4] E. Koos, J. Johannsmeier, L. Schwebler, and N. Willenbacher, “Tuning suspension rheology using capillary forces,” *Soft Matter*, vol. 8, no. 24, 2012.
- [5] F. Bossler, L. Weyrauch, R. Schmidt, and E. Koos, “Influence of mixing conditions on the rheological properties and structure of capillary suspensions,” *Colloids Surf A Physicochem Eng Asp*, vol. 518, pp. 85–97, 2017.
- [6] B. Bitsch, J. Dittmann, M. Schmitt, P. Scharfer, W. Schabel, and N. Willenbacher, “A novel slurry concept for the fabrication of lithium-ion battery electrodes with beneficial properties,” *Journal of Power Sources*, vol. 265, pp. 81–90, 2014.

- [7] B. Bitsch, B. Braunschweig, and N. Willenbacher, “Interaction between polymeric additives and secondary fluids in capillary suspensions,” *Langmuir*, vol. 32, no. 6, pp. 1440–9, 2016.
- [8] J. Park, N. Willenbacher, and K. H. Ahn, “How the interaction between styrene-butadiene-rubber (sbr) binder and a secondary fluid affects the rheology, microstructure and adhesive properties of capillary-suspension-type graphite slurries used for li-ion battery anodes,” *Colloids and Surfaces A: Physicochemical and Engineering Aspects*, vol. 579, 2019.
- [9] J. Park and K. H. Ahn, “Controlling drying stress and mechanical properties of battery electrodes using a capillary force-induced suspension system,” *Industrial & Engineering Chemistry Research*, vol. 60, no. 13, pp. 4873–4882, 2021.
- [10] M. Schneider, N. Willenbacher, E. Koos, and C. Yuce, “Process for producing highly conductive, printable pastes from capillary suspensions,” U.S. Patent 20190148030A1, May 2019.
- [11] M. Schneider, E. Koos, and N. Willenbacher, “Highly conductive, printable pastes from capillary suspensions,” *Sci Rep*, vol. 6, p. 31367, 2016.
- [12] S. Roh, D. P. Parekh, B. Bharti, S. D. Stoyanov, and O. D. Velev, “3d printing by multiphase silicone/water capillary inks,” *Adv Mater*, vol. 29, no. 30, 2017.
- [13] H. Ding, S. Barg, and B. Derby, “Direct 3d printing of graphene using capillary suspensions,” *Nanoscale*, vol. 12, no. 21, pp. 11440–11447, 2020.
- [14] M. Weiß, P. Sälzler, N. Willenbacher, and E. Koos, “3d-printed lightweight ceramics using capillary suspensions with incorporated nanoparticles,”

- Journal of the European Ceramic Society*, vol. 40, no. 8, pp. 3140–3147, 2020.
- [15] S. Wollgarten, C. Yuce, E. Koos, and N. Willenbacher, “Tailoring flow behavior and texture of water based cocoa suspensions,” *Food Hydrocoll*, vol. 52, pp. 167–174, 2015.
- [16] S. Hoffmann, E. Koos, and N. Willenbacher, “Using capillary bridges to tune stability and flow behavior of food suspensions,” *Food Hydrocolloids*, vol. 40, pp. 44–52, 2014.
- [17] W. Mustafa, G. Pataro, G. Ferrari, and F. Donsì, “Novel approaches to oil structuring via the addition of high-pressure homogenized agri-food residues and water forming capillary bridges,” *Journal of Food Engineering*, vol. 236, pp. 9–18, 2018.
- [18] J. Dittmann, E. Koos, N. Willenbacher, and A. Krell, “Ceramic capillary suspensions: Novel processing route for macroporous ceramic materials,” *Journal of the American Ceramic Society*, vol. 96, no. 2, pp. 391–397, 2013.
- [19] D. Menne, L. Lemos da Silva, M. Rotan, J. Glaum, M. Hinterstein, and N. Willenbacher, “Giant functional properties in porous electroceramics through additive manufacturing of capillary suspensions,” *ACS Appl Mater Interfaces*, 2022.
- [20] M. Weiß, J. Maurath, N. Willenbacher, and E. Koos, “Shrinkage and dimensional accuracy of porous ceramics derived from capillary suspensions,” *Journal of the European Ceramic Society*, vol. 39, no. 5, pp. 1887–1892, 2019.

- [21] J. Maurath, J. Dittmann, N. Schultz, and N. Willenbacher, “Fabrication of highly porous glass filters using capillary suspension processing,” *Separation and Purification Technology*, vol. 149, pp. 470–478, 2015.
- [22] K. Hartung, C. Benner, N. Willenbacher, and E. Koos, “Lightweight porous glass composite materials based on capillary suspensions,” *Materials (Basel)*, vol. 12, no. 4, 2019.
- [23] J. Dittmann, J. Maurath, B. Bitsch, and N. Willenbacher, “Highly porous materials with unique mechanical properties from smart capillary suspensions,” *Adv Mater*, vol. 28, no. 8, pp. 1689–96, 2016.
- [24] K. Hauf, K. Riazi, N. Willenbacher, and E. Koos, “Radical polymerization of capillary bridges between micron-sized particles in liquid bulk phase as a low temperature route to produce porous solid materials,” *Colloid Polym Sci*, vol. 295, no. 10, pp. 1773–1785, 2017.
- [25] K. Hauf and E. Koos, “Structure of capillary suspensions and their versatile applications in the creation of smart materials,” *MRS Commun*, vol. 8, no. 2, pp. 332–342, 2018.
- [26] M. Schneider, J. Maurath, S. B. Fischer, M. Weiss, N. Willenbacher, and E. Koos, “Suppressing crack formation in particulate systems by utilizing capillary forces,” *ACS Appl Mater Interfaces*, vol. 9, no. 12, pp. 11095–11105, 2017.
- [27] S. B. Fischer and E. Koos, “Using an added liquid to suppress drying defects in hard particle coatings,” *J Colloid Interface Sci*, vol. 582, no. Pt B, pp. 1231–1242, 2021.

- [28] S. B. Fischer and E. Koos, “Influence of drying conditions on the stress and weight development of capillary suspensions,” *Journal of the American Ceramic Society*, vol. 104, no. 3, pp. 1255–1270, 2020.
- [29] T. Domenech and S. Velankar, “Capillary-driven percolating networks in ternary blends of immiscible polymers and silica particles,” *Rheologica Acta*, vol. 53, no. 8, pp. 593–605, 2014.
- [30] J. M. Lee, J. S. Hong, and K. H. Ahn, “Particle percolation in a poly(lactic acid)/calcium carbonate nanocomposite with a small amount of a secondary phase and its influence on the mechanical properties,” *Polymer Composites*, vol. 40, no. 10, pp. 4023–4032, 2019.
- [31] J. H. Ahn, J. S. Hong, and K. H. Ahn, “Toughening effect of clay particles on poly(lactic acid)/natural rubber blend,” *Nihon Reoroji Gakkaishi*, vol. 48, no. 2, pp. 101–107, 2020.
- [32] J. H. Kim, J. S. Hong, and K. H. Ahn, “Secondary polymer-induced particle aggregation and its rheological, electrical, and mechanical effects on plabased ternary composites,” *Journal of Rheology*, vol. 66, no. 2, pp. 275–291, 2022.
- [33] J. H. Kim, J. S. Hong, and K. H. Ahn, “Design of electrical conductive poly(lactic acid)/carbon black composites by induced particle aggregation,” *Journal of Applied Polymer Science*, vol. 137, no. 42, 2020.
- [34] J. H. Ahn, J. S. Hong, and K. H. Ahn, “Synergistic toughening effect of hybrid clay particles on poly(lactic acid)/natural rubber blend,” *Polymer Composites*, vol. 42, no. 2, pp. 1021–1033, 2020.

- [35] J. H. Kim, J. S. Hong, A. Ishigami, T. Kurose, H. Ito, and K. H. Ahn, “Effect of melt-compounding protocol on self-aggregation and percolation in a ternary composite,” *Polymers (Basel)*, vol. 12, no. 12, 2020.
- [36] T. Domenech and S. S. Velankar, “On the rheology of pendular gels and morphological developments in paste-like ternary systems based on capillary attraction,” *Soft Matter*, vol. 11, no. 8, pp. 1500–16, 2015.
- [37] K. D. Danov, M. T. Georgiev, P. A. Kralchevsky, G. M. Radulova, T. D. Gurkov, S. D. Stoyanov, and E. G. Pelan, “Hardening of particle/oil/water suspensions due to capillary bridges: Experimental yield stress and theoretical interpretation,” *Adv Colloid Interface Sci*, vol. 251, pp. 80–96, 2018.
- [38] A. Ahuja and C. Gamonpilas, “Dual yielding in capillary suspensions,” *Rheologica Acta*, vol. 56, no. 10, pp. 801–810, 2017.
- [39] A. Ahuja, T. Peifer, C. C. Yang, O. Ahmad, and C. Gamonpilas, “Wall slip and multi-tier yielding in capillary suspensions,” *Rheologica Acta*, vol. 57, no. 10, pp. 645–653, 2018.
- [40] E. Koos, W. Kannyade, and N. Willenbacher, “Restructuring and aging in a capillary suspension,” *Rheol Acta*, vol. 53, no. 12, pp. 947–957, 2014.
- [41] F. Bossler and E. Koos, “Structure of particle networks in capillary suspensions with wetting and nonwetting fluids,” *Langmuir*, vol. 32, no. 6, pp. 1489–501, 2016.
- [42] F. Bossler, J. Maurath, K. Dyhr, N. Willenbacher, and E. Koos, “Fractal approaches to characterize the structure of capillary suspensions using rheology and confocal microscopy,” *J Rheol (N Y N Y)*, vol. 62, no. 1, pp. 183–196, 2018.

- [43] S. Bindgen, F. Bossler, J. Allard, and E. Koos, “Connecting particle clustering and rheology in attractive particle networks,” *Soft Matter*, vol. 16, no. 36, pp. 8380–8393, 2020.
- [44] E. Koos and N. Willenbacher, “Particle configurations and gelation in capillary suspensions,” *Soft Matter*, vol. 8, no. 14, 2012.
- [45] E. Koos, “Capillary suspensions: Particle networks formed through the capillary force,” *Curr Opin Colloid Interface Sci*, vol. 19, no. 6, pp. 575–584, 2014.
- [46] A. Fortini, “Clustering and gelation of hard spheres induced by the pickering effect,” *Phys Rev E Stat Nonlin Soft Matter Phys*, vol. 85, no. 4 Pt 1, p. 040401, 2012.
- [47] I. Natalia, R. H. Ewoldt, and E. Koos, “Questioning a fundamental assumption of rheology: Observation of noninteger power expansions,” *Journal of Rheology*, vol. 64, no. 3, pp. 625–635, 2020.
- [48] I. Natalia, R. H. Ewoldt, and E. Koos, “Particle contact dynamics as the origin for noninteger power expansion rheology in attractive suspension networks,” *Journal of Rheology*, vol. 66, no. 1, pp. 17–30, 2022.
- [49] A. Barbot and T. Araki, “Colloidal suspensions in one-phase mixed solvents under shear flow,” *Soft Matter*, vol. 13, no. 35, pp. 5911–5921, 2017.
- [50] H.-J. Butt, W. J. P. Barnes, A. del Campo, M. Kappl, and F. Schönfeld, “Capillary forces between soft, elastic spheres,” *Soft Matter*, vol. 6, no. 23, 2010.

- [51] D. Megias-Alguacil and L. J. Gauckler, “Analysis of the capillary forces between two small solid spheres binded by a convex liquid bridge,” *Powder Technology*, vol. 198, no. 2, pp. 211–218, 2010.
- [52] D. Megias-Alguacil and L. J. Gauckler, “Capillary forces between two solid spheres linked by a concave liquid bridge: Regions of existence and forces mapping,” *AIChE Journal*, vol. 55, no. 5, pp. 1103–1109, 2009.
- [53] B. Rajaram and A. Mohraz, “Microstructural response of dilute colloidal gels to nonlinear shear deformation,” *Soft Matter*, vol. 6, no. 10, 2010.
- [54] N. Koumakis and G. Petekidis, “Two step yielding in attractive colloids: transition from gels to attractive glasses,” *Soft Matter*, vol. 7, no. 6, 2011.
- [55] K. Masschaele, J. Fransaer, and J. Vermant, “Flow-induced structure in colloidal gels: direct visualization of model 2d suspensions,” *Soft Matter*, vol. 7, no. 17, 2011.
- [56] J. Vermant and M. J. Solomon, “Flow-induced structure in colloidal suspensions,” *Journal of Physics: Condensed Matter*, vol. 17, no. 4, pp. R187–R216, 2005.
- [57] J. D. Park and K. H. Ahn, “Structural evolution of colloidal gels at intermediate volume fraction under start-up of shear flow,” *Soft Matter*, vol. 9, no. 48, 2013.
- [58] S. A. Rogers, “In search of physical meaning: defining transient parameters for nonlinear viscoelasticity,” *Rheologica Acta*, vol. 56, no. 5, pp. 501–525, 2017.

- [59] J. D. Park and S. A. Rogers, “The transient behavior of soft glassy materials far from equilibrium,” *Journal of Rheology*, vol. 62, no. 4, pp. 869–888, 2018.
- [60] J. D. Park and S. A. Rogers, “Rheological manifestation of microstructural change of colloidal gel under oscillatory shear flow,” *Physics of Fluids*, vol. 32, no. 6, 2020.
- [61] D. A. Edwards, H. Brenner, and D. T. Wasan, *Interfacial transport processes and rheology*. Butterworth-Heinemann series in chemical engineering, Boston: Butterworth-Heinemann, 1991.
- [62] J. F. Joanny and P. G. Degennes, “A model for contact-angle hysteresis,” *Journal of Chemical Physics*, vol. 81, no. 1, pp. 552–562, 1984.
- [63] D. M. Heyes and J. R. Melrose, “Brownian dynamics simulations of model hard-sphere suspensions,” *Journal of Non-Newtonian Fluid Mechanics*, vol. 46, no. 1, pp. 1–28, 1993.
- [64] D. R. Foss and J. F. Brady, “Brownian dynamics simulation of hard-sphere colloidal dispersions,” *Journal of Rheology*, vol. 44, no. 3, pp. 629–651, 2000.
- [65] R. B. Bird, W. E. Stewart, and E. N. Lightfoot, *Transport phenomena*. New York: J. Wiley, 2nd, wiley international ed., 2002.
- [66] G. K. Batchelor, “Stress system in a suspension of force-free particles,” *Journal of Fluid Mechanics*, vol. 41, pp. 545–+, 1970.
- [67] A. K. Thakre, W. K. den Otter, J. T. Padding, and W. J. Briels, “Spinal decomposition of asymmetric binary fluids in a micro-couette geom-

- etry simulated with molecular dynamics,” *Journal of Chemical Physics*, vol. 129, no. 7, 2008.
- [68] M. Schindler, “A numerical test of stress correlations in fluctuating hydrodynamics,” *Chemical Physics*, vol. 375, no. 2-3, pp. 327–336, 2010.
- [69] A. Savitzky and M. J. E. Golay, “Smoothing + differentiation of data by simplified least squares procedures,” *Analytical Chemistry*, vol. 36, no. 8, pp. 1627–&, 1964.
- [70] S. Huprikar, S. Usgaonkar, A. K. Lele, and A. V. Orpe, “Microstructure and yielding of capillary force induced gel,” *Rheologica Acta*, vol. 59, no. 5, pp. 291–306, 2020.
- [71] I. Natalia, N. Zeiler, M. Weiss, and E. Koos, “Negative normal stress differences  $n_1$ - $n_2$  in a low concentration capillary suspension,” *Soft Matter*, vol. 14, no. 17, pp. 3254–3264, 2018.
- [72] K. Hyun, S. H. Kim, K. H. Ahn, and S. J. Lee, “Large amplitude oscillatory shear as a way to classify the complex fluids,” *Journal of Non-Newtonian Fluid Mechanics*, vol. 107, no. 1-3, pp. 51–65, 2002.
- [73] I. Tucker, Charles L. and P. Moldenaers, “Microstructural evolution in polymer blends,” *Annual Review of Fluid Mechanics*, vol. 34, p. 177, 2002.
- [74] M. Minale, P. Moldenaers, and J. Mewis, “Effect of shear history on the morphology of immiscible polymer blends,” *Macromolecules*, vol. 30, no. 18, pp. 5470–5475, 1997. doi: 10.1021/ma9617330.
- [75] Z. Shi, Y. Zhang, M. Liu, D. A. H. Hanaor, and Y. Gan, “Dynamic contact angle hysteresis in liquid bridges,” *Colloids and Surfaces A: Physicochemical and Engineering Aspects*, vol. 555, pp. 365–371, 2018.

- [76] A. DeSimone, N. Grunewald, and F. Otto, “A new model for contact angle hysteresis,” *Networks & Heterogeneous Media*, vol. 2, no. 2, pp. 211–225, 2007.
- [77] A. Malevanets and R. Kapral, “Mesoscopic model for solvent dynamics,” *The Journal of Chemical Physics*, vol. 110, no. 17, pp. 8605–8613, 1999.
- [78] P. J. Hoogerbrugge and J. M. V. A. Koelman, “Simulating microscopic hydrodynamic phenomena with dissipative particle dynamics,” *Europhysics Letters (EPL)*, vol. 19, pp. 155–160, jun 1992.
- [79] R. A. Gingold and J. J. Monaghan, “Smoothed particle hydrodynamics: theory and application to non-spherical stars,” *Monthly Notices of the Royal Astronomical Society*, vol. 181, pp. 375–389, 12 1977.